



# Graphene Nanodevices

Victor Calado

# Graphene nanodevices



# Graphene nanodevices

## Proefschrift

ter verkrijging van de graad van doctor  
aan de Technische Universiteit Delft,  
op gezag van de Rector Magnificus Prof. ir. K.C.A.M Luyben,  
voorzitter van het College voor Promoties,  
in het openbaar te verdedigen op vrijdag 13 september 2013 om 12:30 uur

door

**Victor Emanuel CALADO**

Natuurkundig ingenieur  
geboren te Rotterdam.



Dit proefschrift is goedgekeurd door de promotor:

Prof. dr. ir. L.M.K. Vandersypen

Samenstelling van de promotiecommissie:

Rector Magnificus	Voorzitter
Prof. dr. ir. L.M.K. Vandersypen	Technische Universiteit Delft, promotor
Prof. dr. C. Dekker	Technische Universiteit Delft
Prof. dr. ir. H.S.J. van der Zant	Technische Universiteit Delft
Prof. dr. F. Guinea	Instituto de Ciencia de Materiales de Madrid
Prof. dr. C. Schönnenberger	Universität Basel
dr. L. DiCarlo	Technische Universiteit Delft
Prof. dr. ir. L.P. Kouwenhoven	Technische Universiteit Delft, reservelid



ISBN: 978-90-8593-163-8

Casimir PhD Series, Delft-Leiden 2013-22

Copyright © 2013 by Victor Calado

All rights reserved. No part of the material protected by this copyright notice may be reproduced or utilized in any form of by any means, electronic or mechanical, including photocopying, recording, or by any information storage and retrieval system, without the prior permission of the author.

Printed by Gildeprint Drukkerijen - [www.gildeprint.nl](http://www.gildeprint.nl)

---

Man reist ja nicht, um anzukommen, sondern um zu reisen.

*Goethe: Begegnungen und Gespräche: 1786-1792*



---

# Contents

<b>1</b>	<b>Introduction</b>	<b>1</b>
<b>2</b>	<b>Theory</b>	<b>7</b>
2.1	Electronic Bandstructure . . . . .	7
2.1.1	Atomic structure . . . . .	7
2.1.2	Tight-binding model . . . . .	8
2.1.3	Dirac Equation . . . . .	9
2.1.4	Conservation of pseudo-spin . . . . .	10
2.2	Veselago lens . . . . .	11
2.3	Conductivity of Graphene . . . . .	12
2.4	Quantum Hall effect . . . . .	14
2.5	Superconductivity in Graphene . . . . .	15
2.5.1	Josephson Effect . . . . .	15
2.5.2	Andreev Reflection . . . . .	16
<b>3</b>	<b>Experimental Methods</b>	<b>19</b>
3.1	Introduction . . . . .	19
3.2	Graphene by exfoliation . . . . .	19
3.2.1	Visibility of Graphene . . . . .	20
3.3	Characterization Methods . . . . .	21
3.3.1	Atomic force microscopy . . . . .	21
3.3.2	Raman microscopy . . . . .	21
3.4	Electron-beam lithography . . . . .	22
3.4.1	Contacting graphene . . . . .	23
3.4.2	Etching graphene and bottom split gates . . . . .	24
3.5	Transfer . . . . .	24
3.5.1	Substrate effect . . . . .	24
3.5.2	Dry transfer methods . . . . .	25
3.6	Cleaning Graphene . . . . .	26
3.6.1	Chemical cleaning . . . . .	26
3.6.2	Oven annealing . . . . .	26
3.6.3	Mechanical cleaning . . . . .	27
3.7	Bubbles and wrinkles in graphene . . . . .	27
3.7.1	Wrinkles and bubbles in graphene on hBN . . . . .	28
3.8	Measurement Setup . . . . .	29

<b>4</b>	<b>Wedging Transfer of Nanostructures</b>	<b>33</b>
4.1	Introduction . . . . .	33
4.1.1	Motivation . . . . .	33
4.1.2	Wedging principle . . . . .	34
4.2	Glass slide example . . . . .	34
4.3	Transfer & alignment . . . . .	35
4.4	Graphene transfer . . . . .	35
4.5	Versatility . . . . .	37
4.6	Conclusion . . . . .	37
4.7	Methods . . . . .	37
4.7.1	Preparation for wedging transfer . . . . .	37
4.7.2	Preparation of graphene samples . . . . .	39
4.7.3	Nanofabrication of the gold WEDGING patterns and microelec- trodes . . . . .	39
<b>5</b>	<b>Formation and control of wrinkles in graphene by the wedging trans- fer method</b>	<b>41</b>
5.1	Introduction . . . . .	41
5.2	Wrinkle formation . . . . .	42
5.3	Transport measurements . . . . .	44
5.4	Wrinkle orientation and density . . . . .	44
5.5	Conclusion . . . . .	46
5.6	Supplementary . . . . .	46
<b>6</b>	<b>DNA Translocation through Graphene Nanopores</b>	<b>49</b>
6.1	Introduction . . . . .	49
6.2	Graphene nanopore . . . . .	51
6.3	Measurement setup . . . . .	51
6.4	DNA translocations . . . . .	52
6.5	Conclusion . . . . .	54
6.6	Methods . . . . .	55
6.6.1	Graphene sample fabrication . . . . .	55
6.6.2	Fabrication of Nanopores in Graphene . . . . .	55
6.6.3	Nanopore Experiments . . . . .	55
<b>7</b>	<b>Zero-bias conductance peak and Josephson effect in graphene-NbTiN junctions</b>	<b>57</b>
7.1	Introduction . . . . .	57
7.2	Sample fabrication . . . . .	58
7.3	Measurements . . . . .	59
7.3.1	SGN junction: type A . . . . .	59
7.3.2	SGS junction: type B . . . . .	62
7.4	Conclusion . . . . .	63

<b>8</b>	<b>Mechanical cleaning of graphene</b>	<b>65</b>
8.1	Introduction . . . . .	65
8.2	Heat cleaning ineffective . . . . .	66
8.3	Mechanical cleaning with contact mode AFM . . . . .	67
8.3.1	Double gated device . . . . .	68
8.3.2	Discussion . . . . .	68
8.4	Conclusions . . . . .	69
<b>9</b>	<b>Ballistic transport in CVD graphene</b>	<b>71</b>
9.1	Introduction . . . . .	71
9.2	CVD growth . . . . .	72
9.3	Device . . . . .	73
9.4	Transverse Magnetic focussing . . . . .	74
9.5	Inhomogeneous . . . . .	76
9.6	Conclusion . . . . .	77
9.7	Supplementary Information . . . . .	77
9.7.1	TEM . . . . .	77
9.7.2	Fabrication of tungsten bottom gates . . . . .	77
9.7.3	Preparation of hBN substrates . . . . .	78
9.8	Dry Transfer of CVD graphene . . . . .	78
9.8.1	Carrier Density . . . . .	80
9.8.2	Field effect mobility . . . . .	80
9.8.3	Fits with self-consistent Boltzmann model . . . . .	81
9.8.4	TMF in other parts of the device . . . . .	81
9.9	Extraction of $L$ . . . . .	82
<b>10</b>	<b>Outlook</b>	<b>85</b>
10.1	Current status . . . . .	85
10.2	Near-future experiments . . . . .	86
10.2.1	Veselago lens in a $p - n$ junction by CVD graphene . . . . .	87
10.2.2	Double-gated twisted CVD bilayer . . . . .	88
10.2.3	Superconductivity . . . . .	90
10.2.4	Technology . . . . .	91
	<b>Bibliography</b>	<b>108</b>
	<b>Summary</b>	<b>109</b>
	<b>Curriculum Vitae</b>	<b>114</b>
	<b>List of Publications</b>	<b>116</b>
	<b>Acknowledgements</b>	<b>117</b>



---

# CHAPTER 1

---

## Introduction

**Graphene** Graphene is a two dimensional (2D) atomic sheet of carbon. It exists in bulk graphite, which is a stack of graphene layers that are weakly coupled to each other. In 2004 Geim and Novoselov used sticky tape on graphite and transferred a single layer graphene sheet onto a silicon substrate [1]. For the first time graphene was isolated from bulk graphite and, soon after, measurements in high magnetic field revealed that electrons behave as massless Dirac fermions [2, 3]. This has made a huge impact and prompted many research groups to start working on graphene, including our group in Delft. Since then graphene has become a research field in itself. In Fig. 1.1 we have plotted the number of publications per year about graphene on a logarithmic(!) scale. In 2010 Geim and Novoselov were awarded for the Nobel prize in physics *”for groundbreaking experiments regarding the two-dimensional material graphene”* [4, 5].

**Graphene’s superlatives** Graphene has an impressive list of superior properties. Here we list most of them. Graphene is one-atom-layer thin and because of that it is very transparent (97.7% [6]) and flexible [7]. Graphene is a very good electrical conductor, it has a sheet resistance of  $< 100 \Omega/\square$ . Thus graphene combines these often conflicting properties; it is a transparent flexible conductor. Graphene has a Young’s modulus of 1 TPa, which is 100 times more than steel [8]. It has a very high intrinsic mobility, exceeding  $10^6 \text{ cm}^2/\text{Vs}$  [9]. It can sustain very high current densities of six orders larger than copper [10]. Its thermal conductivity,  $\sim 5000 \text{ W/mK}$ , is higher than that of diamond [11–13]. Furthermore, graphene has a negative thermal expansion coefficient at room temperature [14, 15]. It is very impermeable to gases, even to helium [16]. Unlike most semiconductors, graphene is a semiconductor without a bandgap. Because the energy dispersion is linear at low energies, charge carriers are effectively massless. At low energies the kinetic energy is described by the Dirac equation for massless fermions. This makes electrons behave as relativistic chiral particles such as neutrinos. From this diverse set of properties graphene has drawn the attraction of researchers from many different disciplines, such as physicists, chemists, material scientists with theoretical and experimental background.



**2-Dimensional** Graphene belongs to the family of  $sp^2$  carbon allotropes and among 0D fullerenes [17], 1D carbon nanotubes [18] and 3D graphite it completes the list with the 2D variant [19]. Usually thin films become unstable when the thickness is reduced to atomic dimensions [20]. Experimentally it is well-known that atomically thin films will nucleate in clusters or small islands [21]. This is not the case for graphene. Graphene is a true 2D material with an atomic thickness of  $3.4 \text{ \AA}$  [22]. However, graphene always needs a support (i.e. a substrate). For that reason there are always (strong) interactions with its underlying substrate [23], which often degrades the electronic quality of graphene. The choice of substrate becomes thus very relevant.

**Substrate** Graphene has a very good visual contrast on standard 285 nm  $\text{SiO}_2/\text{Si}$  substrates [24]. Moreover  $\text{SiO}_2/\text{Si}$  substrates are widely available, but its disadvantage is that charged impurities are present in the oxide, which leads to electronic scattering and degrade the electronic quality [25]. In addition, since graphene is atomically thin, it is very sensitive to surfaces with a roughness larger than its atomic thickness of  $3.4 \text{ \AA}$ , which is the case for  $\text{SiO}_2$  [26]. When graphene conforms to a rough substrate it causes atomic-scale disorder, which leads to short-range scattering [27–29]. Removing the substrate and making graphene suspended is a solution to suppress scattering, which has led to ultra high mobilities in suspended devices [30, 31]. Another solution is to replace the substrate with one that is atomically flat and inert, such as hexagonal boron nitride (hBN) flakes. This has been achieved by transferring graphene flakes onto hBN flakes. As a result the graphene on hBN showed a carrier mobility an order of magnitude higher than graphene on  $\text{SiO}_2$  [32, 33]. Solid substrates are a lot less fragile than suspended structures and allow more flexibility in device fabrication [34–36]. In addition thin hBN flakes can be used as clean and flat topgate dielectric [37] and as a dielectric separating two graphene layers, for instance for Coulomb drag experiments [38]. Recently, interactions between hBN and graphene resulting in a Moiré pattern have been observed by the appearance of a Hofstadter’s butterfly [39–41].

**Other 2D crystals** As graphene exists as a stable 2D crystal, a lot of research is moving to other 2D materials such as  $\text{MoS}_2$  [42–44],  $\text{WSe}_2$  [45],  $\text{NbSe}_2$  [46] and combinations of those to make heterostructures [47]. With those heterostructures a tunneling-transistor with a thin hBN barrier has been realized [48], where the on/off ratio is enhanced to  $10^6$  by replacing the hBN interlayer with  $\text{WS}_2$  [49].

**Graphene technology** Recently the focus in graphene research is turning towards technology and applications. Large companies, such as Samsung and Nokia, have started researching graphene. In this context it is illustrative to note that the number of patents is increasing exponentially since 2005, Fig. 1.1. In early 2013 the European Commission selected graphene as an EU future and emerging technology flagship with a one billion grant over 10 years. This FET flagship is a consortium of many European research groups and industries that have the joint goal *to take graphene and related layered materials from academic laboratories to society, revolutionize multiple industries and create economic growth and new jobs in Europe*. In less than 10 years, graphene has evolved from a simple proof-of-principle from sticky tape to a potentially disruptive technology that may have a significant impact on society and economy in

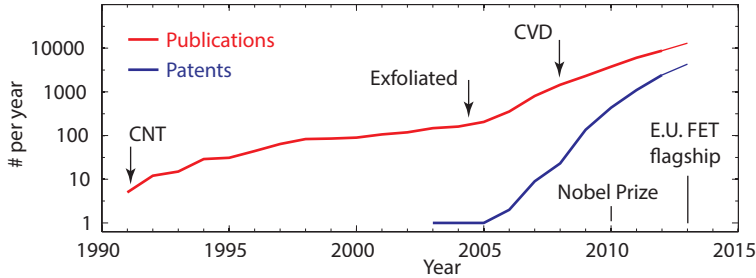


**Figure 1.1:** Number of publication and patents per year that mention 'graphene' on a logarithmic scale. The number of publications for 2013 is estimated to be close to 12000. Source: European Patent Office and Thomson Reuters Web of Science

the next decades of the 21st century.

**Applications** As graphene has such a rich variety of superior properties, there is an even larger list of potential applications that are now foreseen [50]. Here we briefly list some of them in categories.

- **Photonics and Optoelectronics** [51]  
Graphene can be used as a transparent and flexible electrode in touch screens [7] or organic LED's [52]. Graphene can be applied in photo-voltaic cells [53], that can even be flexible [54] and potentially exceed the efficiency of current photo-voltaic cells [55, 56]. Photodetectors made out of graphene could work over much broader wavelength range (up to THz), as there is no bandgap [57, 58].
- **Electronics**  
Graphene has a very high intrinsic mobility that is very attractive for RF transistors [59, 60]. Graphene is not yet suitable for logic (dc) transistors, despite the effort to open a bandgap in nanoribbons [61, 62], double gated bilayers [63] and functionalized graphene [64]. Graphene may be more useful for interconnects in integrated circuits, where it can profit from its excellent thermal and electrical conductivity.
- **Coatings and composites**  
Graphene could be used for coatings or paints that are electrically and thermally conductive, impermeable to gas and inert [65]. Given its high tensile strength it may be used for low-weight mechanical reinforcement [66].
- **Sensing applications**  
Bio-sensing application may require ultra-thin graphene sheets for DNA sequencing [67, 68] and Chapter 6. Graphene is very sensitive to gases, so it could be used as a gas detector [69]. Graphene can also be functionalized, providing selective sensitivity to specific chemicals or biomolecules.
- **Energy storage**  
Graphene supercapacitors have shown a high capacitance [70] and (dis-)charging rates [71] matching today's state-of-art lithium batteries [72].

**Production methods** In order to realise any of the above applications, graphene must be mass produced. Clearly the sticky tape method is not suitable for mass production and a lot of effort is made in developing scalable production methods. Here we mention three methods:

- **Chemical vapour deposition**  
Chemical vapour deposition (CVD) is a promising method for making large sheets of single layer graphene [73]. With this method graphene is grown on metallic surfaces using for instance methane and hydrogen gas as precursors.
- **SiC**  
Graphene can be grown on SiC by sublimating Si at elevated temperatures [74]. With this method high-quality graphene can be produced [59].
- **Liquid-Phase exfoliation**  
Graphene can be exfoliated from graphite with ultrasound in a solvent [75]. The result is a dispersed solution of small graphene flakes. This can be particularly useful for conducting composites, films and paints.

All these methods have their specific advantages and disadvantages, in other words a general superior production method does not exist yet.

**Thesis** This thesis reports very diverse experimental research on graphene with the goal to explore new physics or create novel applications by using the special properties of graphene.

We have developed a water-based transfer technique that allows graphene or nanostructures to be transferred from  $\text{SiO}_2$  substrates onto other substrates, Chapter 4. With this method we are able to fabricate graphene nanopores with high throughput. We have found that wrinkles in graphene sheets are present after transfer, but do not degrade the electronic quality more than the  $\text{SiO}_2$  substrate does, Chapter 5. It has opened the possibility to transfer graphene on other substrates such as hBN. However for graphene/hBN devices we have adapted dry transfer methods, which shows less contamination than the water-based transfer method.

Graphene is a promising candidate for DNA sequencing at the single molecule level. Using graphene nanopores offers the potential of resolving individual base pairs, because the distance between two base pairs is in the order of the thickness of graphene. We have fabricated a graphene nanopore device, through which single DNA molecules were translocated. These translocation events were detected by a reduction in the ionic current through the pore, Chapter 6. The device serves as a prototype single DNA molecule sensor, which is the first step in the direction of a single DNA sequencing device.

Motivated by the prospect of observing Andreev reflection in combination with the Quantum Hall effect (QHE), we have contacted graphene with NbTiN. Because NbTiN is a superconductor with a high critical field of above 11 T and graphene shows QHE at relatively low fields, it should show QHE while the contacts are in the superconducting state. The junctions were too disordered to observe QHE, but we have found that Andreev reflection in a disordered Graphene/NbTiN junction is accompanied by reflectionless tunnelling, Chapter 7.

---

Graphene is prone to residue contamination and many cleaning methods are available, but not always effective. We have developed a mechanical cleaning method for cleaning graphene, Chapter 8. This new technique can serve as an alternative to the existing methods.

The Veselago lensing [76] and Klein tunneling [77] are exemplary for the peculiar nature of electrons in graphene. So far these phenomena are not easily accessible because it requires ballistic transport on a micrometer scale. In that context we have used CVD produced graphene to make the first CVD produced device that shows ballistic transport on micron scales, Chapter 9. This makes it possible to produce ballistic devices with CVD graphene with high throughput for observing these phenomena and exploring other physics.

Basic theory of graphene physics in this thesis is treated in Chapter 2 and the experimental methods that have been used in this thesis are discussed in Chapter 3.



---

# CHAPTER 2

---

## Theory

The topics in this thesis are rather diverse, therefore we limit to the general theory of graphene. We derive the band structure of graphene and the Dirac Hamiltonian. We show that electron-hole symmetry can lead to Veselago lensing, for which we have made ballistic devices in Chapter 9. The conductivity of graphene for 2D conductors is treated in Sec. 2.3, we apply this basic theory in all our conductivity measurements. In Sec. 2.4 the integer quantum Hall effect for graphene is explained. In the last section we discuss superconductivity in graphene, which is particularly relevant for Chapter 7.

### 2.1 Electronic Bandstructure

#### 2.1.1 Atomic structure

Graphene is a 2-dimensional sheet of carbon atoms in a honeycomb lattice, shown in Fig. 2.1a. The inter-atomic distance is  $a_0 = 1.42 \text{ \AA}$ . The primitive unit cell consists of two basis atoms, labelled A and B [78]. The primitive translation vectors make up a triangular lattice and are given by

$$\vec{a}_1 = \frac{a_0}{2} (3, \sqrt{3}), \quad \vec{a}_2 = \frac{a_0}{2} (3, -\sqrt{3}). \quad (2.1)$$

The A atoms make up a sublattice that is independent<sup>1</sup> from sublattice B. This yields an extra degree of freedom and is usually referred to as the pseudo-spin.

The reciprocal lattice is shown in Fig. 2.1b with the first Brillouin Zone (BZ). The reciprocal lattice vectors are given by

$$\vec{b}_1 = \frac{2\pi}{3a_0} (1, \sqrt{3}), \quad \vec{b}_2 = \frac{2\pi}{3a_0} (1, -\sqrt{3}). \quad (2.2)$$

The K points<sup>2</sup> are located at the six corners of the BZ. Only two points are unique, because from these two distinct points (K and K') all other K points can be reached

---

<sup>1</sup>Sublattice B is made up from B atoms. They are distinct because there is no linear combination of  $\vec{a}_1$  and  $\vec{a}_2$  to make the transition from an A atom to a B atom.

<sup>2</sup>In the context of graphene K points are also called Dirac points.

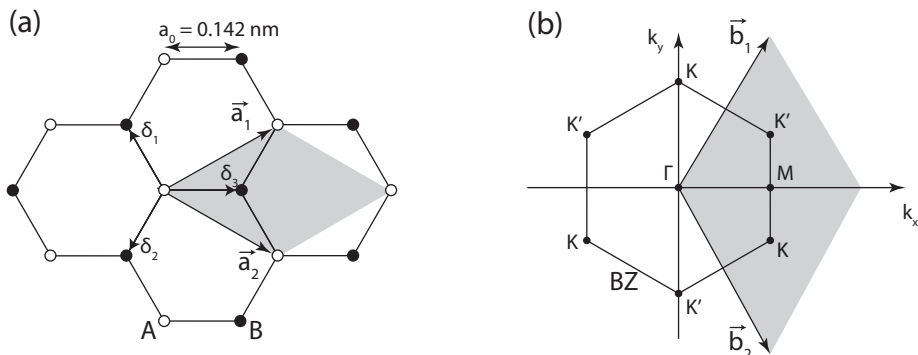


**Figure 2.1:** (a) The atomic lattice of graphene in real space  $(x, y)$  with the sublattices A and B, black and white indicated. The lattice vectors are  $\vec{a}_1$  and  $\vec{a}_2$  making up the primitive unit cell. The carbon atoms are separated by  $\delta_{1,2,3}$  to their nearest neighbours with the inter atomic distance of  $a_0 = 1.42 \text{ \AA}$ . (b) The corresponding lattice in reciprocal space  $(k_x, k_y)$ , with reciprocal lattice vectors  $\vec{b}_1$  and  $\vec{b}_2$ . The first Brillouin zone is drawn with the six K points

with a linear combination of the reciprocal lattice vectors  $\vec{b}_1$  and  $\vec{b}_2$ . K and K' are located at  $\vec{k} = (0, \pm 4\pi/3a_0)$ . In the next section we will show that these K points are at zero energy and therefore play a crucial role in the physics of graphene.

### 2.1.2 Tight-binding model

Each carbon atom has four valence electrons, out of which three form in-plane  $\sigma$ -bonds with three neighbouring atoms by  $sp^2$  hybridization. These are localized and far below the Fermi energy and thus do not contribute to electronic transport. The fourth electron is delocalized and occupies an out-of-plane  $p_z$  orbital, which forms  $\pi$ -bonds with neighbouring atoms. Using the tight-binding model with only nearest-neighbour interaction<sup>3</sup> we can derive the electronic bandstructure of graphene. The tight-binding Hamiltonian has already been solved long ago by Wallace [79] and is given by

$$H = -t \sum_{i,j=1,2,3} (a_{R_i}^\dagger b_{R_i+\delta_j} + h.c.), \quad (2.3)$$

where  $a_{R_i}$  ( $a_{R_i}^\dagger$ ) annihilates (creates) an electron on a lattice site  $R_i$ .  $\delta_j$  are the vectors that connect an A to a B atom. Electrons can hop between nearest-neighbour A and B atoms with hopping energy  $t \approx 2.8 \text{ eV}$ .

Using Bloch wavefunctions on each of the two sublattices we can solve the tight-binding Hamiltonian [80]. The solutions for the bonding and anti-bonding states are given by

$$E(\vec{k}) = \pm t \sqrt{1 + 4 \cos(\sqrt{3}ak_x/2) \cos(ak_y/2) + 4 \cos^2(ak_y/2)}, \quad (2.4)$$

<sup>3</sup>For the sake of discussion we neglect next-nearest-neighbour interaction.

where  $a = \sqrt{3}a_0$  is the lattice constant and  $\pm$  is the solution for the valence and conduction band. In Fig. 2.2a the solutions are plotted in a 3D plot. The bonding and anti-bonding states touch each other at the six K points (Dirac points) at the Fermi level. This means that there is no bandgap at zero energy.

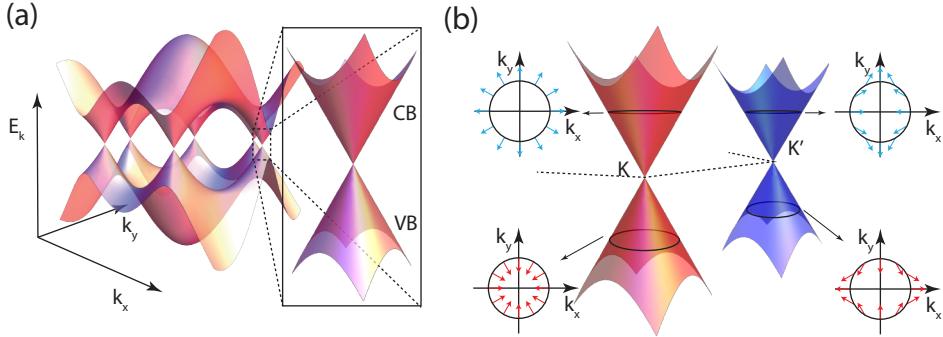


**Figure 2.2:** (a) The energy dispersion in 3D with the bonding and anti-bonding subbands as a result of the tight-binding calculation. The inset shows a close-up near one of the K-points. Here the two cones touch each other (energy gap is zero) and the dispersion is linear, implying massless Dirac fermions. (b) The two distinct valleys (K and K') with the pseudo-spin direction drawn in the insets for each subband.

For low energies at the Dirac point the energy dispersion becomes linear and the charge carrier mass becomes effectively infinite<sup>4</sup>. Therefore the Schrödinger equation no longer holds and the Dirac equation must be used instead.

### 2.1.3 Dirac Equation

A direct result of the linear dispersion close to K and K' at low energy is that the Hamiltonian can be described by the 2D Dirac equation for massless fermions (Weyl equation) which is

$$\hat{H}\Psi = v_F \hat{\sigma} \cdot \hat{p}\Psi, \quad (2.5)$$

where  $v_F = 3a_0t/2/\hbar \approx 10^6$  m s<sup>-1</sup> is the Fermi velocity, which is the analogue of the speed of light.  $\hat{\sigma} \equiv (\pm\hat{\sigma}_x, \hat{\sigma}_y)$  is the 2D vector of the Pauli spin matrices with  $\pm$  for K and K',  $\hat{p}$  the momentum operator<sup>5</sup>.  $\Psi = (\psi_A, \psi_B)$  is the wave function, where  $\psi_A$  and  $\psi_B$  are the complex wave amplitudes on sublattice A and B, respectively.

If we diagonalize the Hamiltonian  $\hat{H}\Psi = \epsilon(\vec{k})\Psi$  we find the plane wave solutions with corresponding eigenenergies  $\epsilon(\vec{k}) = \pm\hbar v_F |\vec{k}|$ . Around K and K' the wave function has the form:

$$\psi_{\pm}^K(\vec{k}) = \frac{1}{\sqrt{2}} \begin{pmatrix} e^{-i\theta(\vec{k})/2} \\ \pm e^{i\theta(\vec{k})/2} \end{pmatrix}, \quad \psi_{\pm}^{K'}(\vec{k}) = \frac{1}{\sqrt{2}} \begin{pmatrix} e^{i\theta(\vec{k})/2} \\ \mp e^{-i\theta(\vec{k})/2} \end{pmatrix}. \quad (2.6)$$

<sup>4</sup>Its effective mass is defined by  $m_{eff} \equiv (\partial^2 E / \partial k^2)^{-1}$ . As a consequence in linear dispersion the effective mass becomes infinite.

<sup>5</sup>The momentum  $\vec{p} = \hbar\vec{k}$  and the wavevector  $\vec{k}$  are from now on defined from K or K' and no longer from  $\Gamma$ , the centre of the Brillouin zone.



The  $\pm$  sign represents electrons in the conduction band and holes in the valence band.  $\theta(k) = \arctan(k_x/k_y)$  is the angle in momentum space. The pseudo-spin is connected to its momentum, so particles are helical or chiral<sup>6</sup>. The helicity is defined by the projection of the momentum direction to its pseudo-spin direction illustrated in Fig. 2.2b. Here the Dirac cones at K and K' are drawn with the pseudo-spin directions for electrons in the conduction band (blue) and holes in valence band (red). For electrons at K the pseudo-spin is aligned with the wavevector, whereas for holes it is anti-aligned. The helicity at K' is opposite to K.

An important consequence of the helicity is that when the phase is rotated by  $2\pi$  (i.e. a particle makes a loop) an additional phase of  $\pi$  is added. This is called Berry's phase [81] and its manifestation has been observed by the anomalous quantum Hall effect [2, 3] and by weak anti-localization [82, 83].

## 2.1.4 Conservation of pseudo-spin

An important implication of the helicity (pseudo-spin tied to the wavevector) is the suppression of backscattering. This can be seen by calculating the probability between spinor wavefunctions residing in the same valley and band but propagating with different angles  $\theta_1$  and  $\theta_2$ :

$$P_{\theta_1 \rightarrow \theta_2} = |\langle \psi_+^K(\theta_1) | \psi_+^K(\theta_2) \rangle|^2 = 1/2(1 + \cos(\theta_1 - \theta_2)). \quad (2.7)$$

For backscattering<sup>7</sup>, i.e. ,  $\theta_1 - \theta_2 = \pi$ , it follows that  $P_{\theta_1 \rightarrow \theta_2} = 0$ . This phenomenon is often called conservation of pseudo-spin. It can be intuitively seen in Fig. 2.2b, where arrows indicate the pseudo-spin direction tied to its wavevector. If an electron tries to backscatter  $k \rightarrow -k$  it needs to reverse its pseudo-spin direction as well. This is not possible since a smooth<sup>8</sup> impurity potential acts on diagonal terms and not on the off-diagonal terms (sublattice space)<sup>9</sup>.

A mechanism that breaks the conservation of pseudo-spin is inter-valley scattering. Through this process an electron is able to make a transition from valley K to K'. Inter-valley scattering occurs at defects on the scale of the lattice constant  $a$  that provide a large momentum transfer of  $|\vec{K} - \vec{K}'| \approx 1/a$ . This couples the two sublattices and thus mixes the pseudo-spin. In pristine graphene it is mainly present at the rough edges.

In the next section we show that transitions between bands in the same valley yield interesting phenomena, realisable in realistic devices using external gates.

---

<sup>6</sup>For massless fermions helicity is equivalent to chirality.

<sup>7</sup>In fact for "true" backscattering one needs to include an impurity potential. Here we demonstrate what is called the chirality factor. In Ref. [84] the same calculation is done with an impurity potential using first order Born approximation.

<sup>8</sup>The potential is assumed smooth compared to the atomic lattice  $\sim a$ , but is allowed to be sharp compared to the Fermi wavelength  $\sim 1/k_F$ .

<sup>9</sup> $\hat{H}\psi = v_F \hat{\sigma} \cdot \hat{\mathbf{p}}\psi + V_{imp}\psi = v_F \begin{pmatrix} V_{imp} & \hat{p}_x - i\hat{p}_y \\ \hat{p}_x + i\hat{p}_y & V_{imp} \end{pmatrix} \psi.$

## 2.2 Veselago lens

A  $p - n$  junction is made by external gates that induce a sharp potential step, shown in Fig. 2.3b. The transmission through such a  $p - n$  junction is analogous with light rays crossing media with a negative index of refraction. This is drawn in Fig. 2.3a for the case where the carrier densities are exactly opposite  $n_n = -n_p$ . This is called a Veselago lens [76, 85, 86]. To derive the index of refraction, we use the conservation of momentum projection along  $y$  and calculate the propagation direction of the charge carriers, which is given by the group velocity of a plane wave by

$$\vec{V} = \frac{1}{\hbar} \frac{d\epsilon}{dk} = \alpha v_F \frac{\vec{k}}{|\vec{k}|}, \quad (2.8)$$

where  $\alpha = \pm 1$  is the band index. It implies that when  $\alpha = -1$  an electron that resides in the valence band and propagates opposite to its wavevector  $\vec{k}$ . The band filling is controlled by the chemical potential and in real devices this is done by applying a voltage to external gates. Consider an incoming electron moving in the conduction band towards the  $p - n$  junction, as is shown in Fig. 2.3a. It has a group velocity

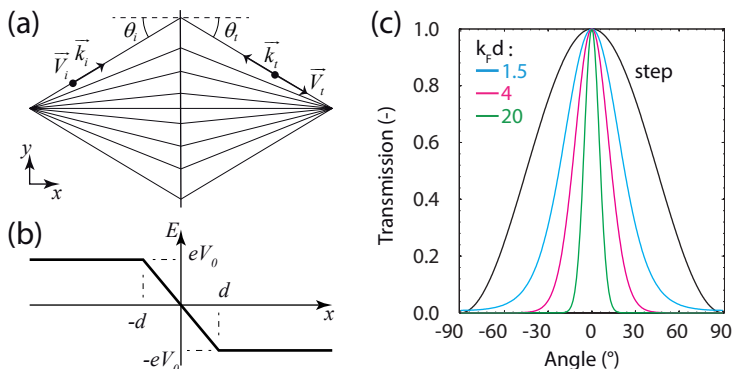


**Figure 2.3:** (a) Electrons leave a point source at the left to right. At the interface of a  $p - n$  junction they are negatively refracted and collimated. This is known as the Veselago lens. (b) The energy as function of the position. The  $p - n$  junction has a junction width  $2d$  and is biased with an energy of  $\pm eV_0$ . (c) The transmission probability as function of incident angle as a result from calculations done in Ref. [84]. The angle transmission width is determined by  $k_F d$ , it implies the smaller the charge carrier density  $n$  the larger incident angles are refracted.

$\vec{V}_i = v_F(\cos \theta_i, \sin \theta_i)$ . Its corresponding wavevector is then  $\vec{k}_i = k_i(\cos \theta_i, \sin \theta_i)$ . At a sharp<sup>10</sup> interface of a  $p - n$  junction, it is partially reflected and transmitted. The transmitted part has a group velocity  $\vec{V}_t = v_F(\cos \theta_t, \sin \theta_t)$ . Because this electron resides now in the valence band ( $\alpha = -1$ ), its wavevector is opposite to the group velocity  $\vec{k}_t = k_t(-\cos \theta_t, -\sin \theta_t)$ . From the conservation of momentum projection

<sup>10</sup>Sharp in this context is  $a < d < 1/k_F$ .

along  $y$  the  $k_y$  component should be preserved:  $k_{y,i} = k_{y,t}$ . It follows that

$$\frac{\sin \theta_i}{\sin \theta_t} = -\frac{k_t}{k_i}. \quad (2.9)$$

This expression is analogous to Snell's law of refraction, with opposite index of refraction, where light rays are refracted between media with negative refractive index, shown in Fig. 2.3a.

So far we have considered a sharp  $p-n$  junction, where the junction width  $a < d < 1/k_F$  in Fig. 2.3b. Because in realistic devices it is not possible to achieve such a sharp junctions we consider a smooth potential variation, where the junction width  $d > 1/k_F$ . The transmission probability as function of incoming angle is then given by Ref. [87]

$$T(\theta) \approx e^{-\pi k_F d \sin^2 \theta}. \quad (2.10)$$

This is plotted in Fig. 2.3c for  $k_F d = 1.5, 4, 20$ . The black line is the transmission probability for a perfectly sharp step. For low  $k_F d$  the collimation effect is the strongest, it has a larger critical angle. From the transmission probabilities we can predict the two terminal conductance for a smooth  $G_{np}^{\text{smooth}}$ , sharp  $G_{np}^{\text{sharp}}$  and no junction  $G$  by the Landauer formula [84, 87]

$$G_{np}^{\text{smooth}} = \frac{1}{2} \sqrt{\frac{1}{k_F d}} G, \quad G_{np}^{\text{sharp}} = \frac{2}{3} G, \quad G = \frac{4e^2}{\pi h} k_F W, \quad (2.11)$$

where  $W$  is the width of the junction. Here we note that the conductance for a smooth junction depends on the junction width  $d$  and increased for sharper junctions.

When the junction is extended to a  $p-n-p$  junction, Klein tunneling can take place [77, 84].

## 2.3 Conductivity of Graphene

We start by considering two transport regimes that can dominate:

- In the diffusive limit ( $l_{mfp} < L$ ) electrons will scatter multiple times across the device size  $L$ . The average path between two collisions is the mean free path  $l_{mfp}$ .
- In the ballistic limit ( $l_{mfp} > L$ ) electrons move without scattering and their momentum and energy are conserved. Here the mean free path ( $l_{mfp}$ ) is larger than the device size ( $L$ ).

In experiments we deal mostly with diffusive conductivity. We therefore treat the Drude model, that describes transport in the diffusive limit. In an equilibrium situation electrons gain momentum from externally applied fields at a rate equal to the rate of lost of momentum due to scattering and this equilibrium is when

$$\frac{m\vec{v}_d}{\tau} = -e \left( \vec{E} + \vec{v}_d \times \vec{B} \right), \quad (2.12)$$

where  $\vec{v}_d$  is the drift velocity,  $\vec{E}$  an electric field and  $\vec{B}$  a magnetic field.  $1/\tau$  is the momentum relaxation rate and in graphene it is equal to  $1/\tau = v_F/l_{mfp}$ . Following Ref. [88], we derive the following resistivity tensor

$$\begin{pmatrix} E_x \\ E_y \end{pmatrix} = \frac{1}{en\mu} \begin{pmatrix} 1 & -\mu B \\ \mu B & 1 \end{pmatrix} \begin{pmatrix} J_x \\ J_y \end{pmatrix} = \begin{pmatrix} \rho_{xx} & \rho_{xy} \\ \rho_{yx} & \rho_{yy} \end{pmatrix} \begin{pmatrix} J_x \\ J_y \end{pmatrix}, \quad (2.13)$$

where  $\mu$  is the charge carrier mobility and is defined by  $\mu \equiv e/\tau m$ ,  $n$  is the charge carrier density which is in graphene<sup>11</sup> equal to  $n = k_F^2/\pi$  and can be controlled with external gates. In Fig. 2.4 a Hall bar geometry is shown of a device. In such a geometry  $\rho_{xx}$  and  $\rho_{xy}$  are given by

$$\rho_{xx} = \frac{(V_2 - V_1)W}{I} = \frac{V_x W}{I L}, \quad \rho_{xy} = \frac{(V_3 - V_1)}{I} = \frac{V_H}{I}, \quad (2.14)$$

where  $I$  is the applied current,  $V_2 - V_1 = V_x$  is the longitudinal voltage along the current direction and  $V_3 - V_1 = V_H$  is the transverse or Hall voltage.  $W$  and  $L$  are the width and the length of the Hall bar.

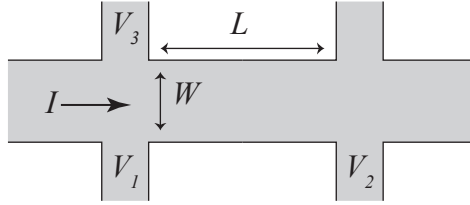


**Figure 2.4:** A Hall bar geometry, with width  $W$  and length  $L$ . A current of  $I$  flows with voltage probes  $V_1$ ,  $V_2$  and  $V_3$ .

From the resistivity tensor we can extract the carrier density  $n$  with a corresponding charge carrier mobility<sup>12</sup>  $\mu$  by

$$n = \frac{I}{e \frac{dV_H}{dB}}, \quad \mu = \frac{I}{neV_x} \frac{L}{W}, \quad (2.15)$$

where  $e$  is the electron charge. We can characterize the electronic quality of graphene by extracting the mobility  $\mu$  from measuring  $V_x$  and  $V_H$  as function of  $B$ .

In graphene the charge carrier density can be changed by capacitively coupled external gates. The carrier density as function of a gate voltage  $V_g$  can be calculated by the parallel plate capacitor approximation, which is

$$n = \frac{\epsilon_r \epsilon_0}{ed} V_g, \quad (2.16)$$

where  $d$  is the distance from the gate and  $\epsilon_r \epsilon_0$  the dielectric constant of the dielectric in between. At zero magnetic field the longitudinal conductivity is equal to  $\sigma_{xx} = 1/\rho_{xx}$ .

<sup>11</sup>The charge carrier density in 2D is given by  $n_{2D} = g \frac{\pi k_F^2}{4\pi^2}$ . In graphene  $g = 4$ , because of the spin and valley degeneracy.

<sup>12</sup>It is often called the Hall mobility because of the extraction via the Hall effect.

With the conductivity as function of the carrier density one can estimate the charge carrier mobility<sup>13</sup> by

$$\mu = \frac{1}{e} \frac{d\sigma_{xx}}{dn}, \quad (2.17)$$

where  $d\sigma_{xx}/dn$  is the slope that can be extracted from the backgate dependence of the conductance.

## 2.4 Quantum Hall effect

When graphene is subjected to a strong magnetic field, its linear density of states (DOS) will change into a set of discrete peaks located at energies at the Landau levels (LL). We derive the LL energies using a semiclassical approach.

A magnetic field bends flowing charges by the Lorentz force and, when sufficiently strong, electrons (and holes) will follow a circular path, called cyclotron orbit. In the presence of a magnetic field the canonical momentum  $\vec{p}$  is modified and becomes  $\vec{P} = \vec{p} + e\vec{A}$ , with  $\vec{A}$  the vector potential,  $\vec{B} = \vec{\nabla} \times \vec{A}$ . The cyclotron radius is then  $r_c = |\vec{P}|/eB$ . Upon completing a full orbit an electron wavefunction will gain a phase  $\phi$  and it can constructively interfere with itself when  $\phi = 2\pi N$ . The accumulated phase  $\phi$  around a stable cyclotron orbit is calculated by

$$\phi = \frac{1}{\hbar} \oint d\vec{r} \cdot \vec{p} = \frac{\pi P^2}{\hbar e B} = 2\pi N, \quad (2.18)$$

where  $N$  is an integer number<sup>14</sup>. From the energy dispersion  $E = \pm v_F |\vec{P}|$  we obtain the LL energies, which are

$$E = \pm v_F \sqrt{2\hbar e B N}. \quad (2.19)$$

In Fig. 2.5a the DOS is sketched as function of energy, in grey the DOS at zero field and in black the LL at strong magnetic field. We note the  $\sqrt{N}$  dependence on the energy, which is different from usual 2DEG systems<sup>15</sup>, where  $N$  is linear in energy. Each LL can host a limited number of electrons/holes per unit area, which is the LL degeneracy  $N_{el}/A = gB/\Phi_0$ , where  $g = 4$ , two from the spin and two from the valley degeneracy. When the Fermi level is in between two LLs, the conductance will be quantized and conductance plateaus will appear in the transverse direction and the longitudinal resistance will vanish

$$\rho_{xx} = 0, \quad \sigma_{xy} = 4 \left( N + \frac{1}{2} \right) \frac{e^2}{h}. \quad (2.20)$$

In Fig. 2.5b,  $\sigma_{xy}$  is plotted as function of filling factor. Discrete plateaus are visible at  $\pm 2, \pm 6, \pm 10, \dots e^2/h$ . Due to the Berry's phase, a LL appears at zero energy, which

---

<sup>13</sup>This is also called the field-effect mobility.

<sup>14</sup>Here we use the semiclassical Bohr-Sommerfeld quantization for a cyclotron orbit. A phase addition of  $2\pi$  is included here. It is due to caustics (Maslov contribution of  $\pi$ ) and Berry's phase ( $\pi$ ). See Ref. [89] for more about this approach.

<sup>15</sup>2DEG stands for 2 dimensional electron gas, such as in GaAs/AlGaAs hetero-structures.

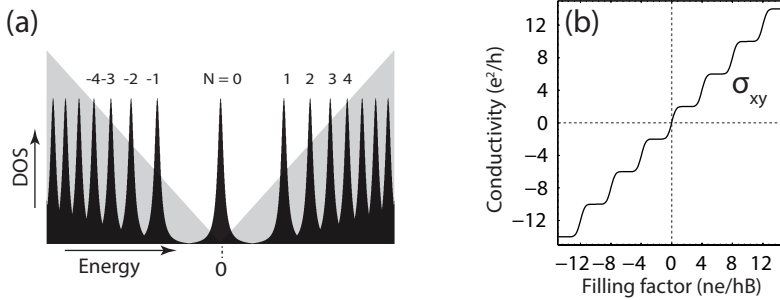


**Figure 2.5:** (a) In grey the linear DOS at zero field. In black the DOS at high magnetic field, The peaks indicated by  $N = 0, \pm 1, \pm 2, \pm 3, \pm 4$  are Landau levels and are strongly degenerate. (b) The hall conductivity  $\sigma_{xy}$  as function of the filling factor. Quantized plateaus appear when the filling factor is tuned in between two Landau levels and conductivity corresponds precisely to the number of transport channels.

is filled with both holes and electrons. This is in strong contrast with conventional 2DEG's, where no LL is present at zero energy. As a consequence in graphene there is no conductance plateau at zero energy. This is characteristic for graphene, where transport is governed by massless Dirac fermions that are helical, which lead to the anomalous quantum Hall effect [2, 3, 90].

## 2.5 Superconductivity in Graphene

### 2.5.1 Josephson Effect

Superconductivity is well described by the Bardeen-Cooper-Schrieffer (BCS) theory [91, 92], where electrons form a Bose-Einstein condensate of Cooper pairs. A Cooper pair is a pair of two electrons with opposite momentum and thus a boson. The condensate is described by a macroscopic wavefunction

$$\Psi = |\Psi|e^{i\phi}. \quad (2.21)$$

Here,  $\phi$  is the phase of the wavefunction and  $|\Psi|$  its amplitude. When two superconductors are separated by a thin insulating barrier a spontaneous DC current (supercurrent  $I_s$ ) can flow through it. This effect was predicted by B. D. Josephson in 1962 [93]. The insulating barrier can become superconducting by the proximity effect. The barrier does not have to be necessarily insulating: semiconducting [94, 95] or even metallic barriers can be superconducting by the proximity effect, as well as graphene [96].

The supercurrent is determined by the phase difference of the two superconductors  $\varphi_1 - \varphi_2 = \Delta\phi$  and given by

$$I_s = I_c \sin(\Delta\phi). \quad (2.22)$$

In Fig. 2.6a, a schematic is shown of two superconductors with macroscopic wavefunctions  $|\Psi_1|e^{i\varphi_1}$  and  $|\Psi_2|e^{i\varphi_2}$  that are contacted to a graphene strip of size  $L \times W$ . The phase difference can be tuned by a small perpendicular magnetic flux, which would

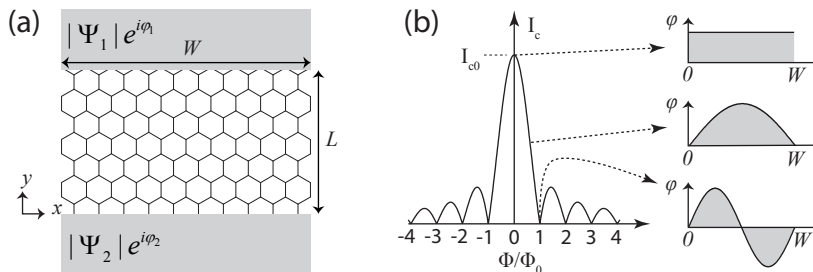


**Figure 2.6:** (a) Graphene is contacted by two superconductors with wavefunctions  $|\Psi_1|e^{i\varphi_1}$  and  $|\Psi_2|e^{i\varphi_2}$ . Graphene can become superconducting by the proximity effect, which is the manifestation of the Josephson effect. (b) A Fraunhofer pattern. The critical supercurrent as a function of flux through the graphene area. In the insets the position dependent phase, which has to be integrated to obtain the critical supercurrent, which explains the oscillatory behaviour. Figure is inspired by Ref. [97].

change the supercurrent. The flux through the graphene strip is  $\Phi = BLW$  and the corresponding phase addition across the width  $W$  as function of position  $x$  is then

$$\varphi(x) = 2\pi \frac{BLx}{\Phi_0}. \quad (2.23)$$

Here the phase  $\varphi(x)$  is now position dependent. To obtain the total supercurrent through the junction, the supercurrent density<sup>16</sup> has to be integrated over the width  $W$ , following the derivation in Ref. [97], this yields

$$I_c = I_{c0} |\text{sinc}(\pi\Phi/\Phi_0)|, \quad (2.24)$$

where  $\Phi_0 = h/2e$  is the flux quantum. This is plotted in Fig. 2.6b. This periodic pattern is known as a Fraunhofer interference pattern. When the total flux equals an integer number of flux quanta,  $\Phi = N\Phi_0$ , the sum of phases across the junction is exactly zero and the supercurrent disappears. This cancellation is indicated in the lower panel where the total area, that equals the critical supercurrent, is zero.

## 2.5.2 Andreev Reflection

When graphene (a normal conductor) is connected to a superconductor, electronic transport through the graphene/superconductor interface is governed by Andreev reflection [98]. This process is schematically shown in Fig. 2.7a.

Consider an electron moving with momentum  $\vec{k}_e$  and group velocity  $\vec{v}$  towards the superconductor with an energy  $\delta\varepsilon$  away from the Fermi energy  $E_F \gg \delta\varepsilon$ . Given here that the energy is smaller than the superconducting gap ( $\delta\varepsilon < \Delta$ ), there are no states in the superconductor to accommodate the electron by itself in the superconductor<sup>17</sup>. Instead a second electron with energy  $-\delta\varepsilon$  and opposite momentum  $-\vec{k}_e$  but with the same group velocity  $\vec{v}$  pairs up with the first one to form a Cooper pair and have become

<sup>16</sup>Current per unit length  $J = dI/dx$ .

<sup>17</sup>Above and below the superconducting gap  $\Delta$  electrons can form quasi-particles and the charge transfer is accompanied by a single charge  $e$ .

part of the condensate in the superconductor. The second electron has left a hole behind with an inverted momentum  $\vec{k}_e$  and group velocity direction  $-\vec{v}$  and thus the hole retraces the path backwards. This is shown in Fig. 2.7c in real space, with in Fig. 2.7b the corresponding energy dispersion in graphene where the Fermi energy is larger than the superconducting gap  $|E_F| > \Delta$ . The total charge that is transferred is  $2e$  and thus the conductance across the interface is doubled compared to the normal state resistance.

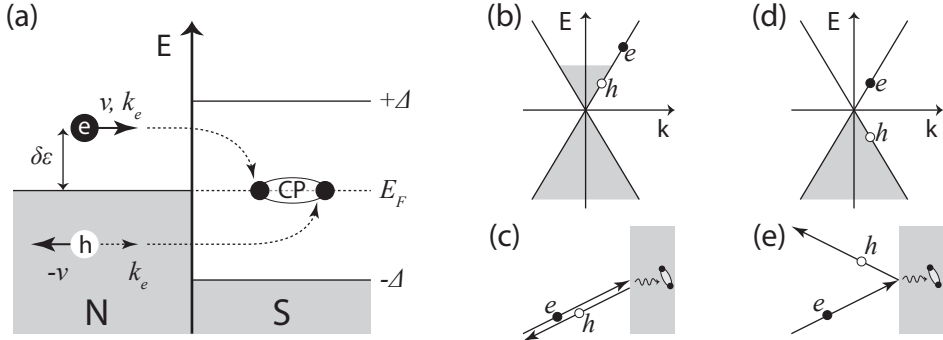


**Figure 2.7:** (a) Andreev Reflection occurs at a normal-superconductor (N-S) interface, where an electron impinging on the interface pairs up with a second electron to form a Cooper pair. The resulting hole that is left behind travels backward. The total charge transferred is doubled, which in experiments is detected as a doubling of the conductance. In (b) and (d) the linear band dispersion of graphene at high charge carrier density and at zero charge density. In the latter specular Andreev reflection, in (e) occurs by the interchange of a subband. This effect has not been seen yet in experiments. (c) The retro-reflected situation occurs at high densities and is so far always seen in experiments.

The chirality is conserved in an Andreev reflection process, this has an important implication [99]. Backscattering is prohibited within the same sublattice. Thus at normal incidence, an electron cannot backscatter at the graphene/superconductor interface and the Andreev reflection probability is unity. This is analogous to the Klein tunnelling situation with a potential barrier [77, 100].

Another effect that can exist in graphene/superconductor interfaces is specular Andreev reflection. This is illustrated in Fig. 2.7d and 2.7e. When the Fermi energy is smaller than the superconducting gap (i.e. undoped graphene)  $|E_F| < \Delta$ , the reflected hole will appear in lower subband, which has a different band index. The hole still has the same momentum but since it resides in a different subband its group velocity is this time aligned with the momentum and is thus specularly reflected.





---

## CHAPTER 3

---

# Experimental Methods

### 3.1 Introduction

In this chapter the experimental methods are treated that have been used in most of the experiments described in this thesis. Device fabrication is usually done in the following order:

- Graphene deposition by mechanical exfoliation
- Characterization
- Transfer to hBN
- Contacting graphene
- Cleaning processing

These steps are treated one by one in the next sections. For some experiments we used different processing steps, which are treated separately in the chapters. Here we provide the general approach. In the last section we describe the measurement setup.

### 3.2 Graphene by exfoliation

For most of the experiments described in this thesis graphene is made by mechanical exfoliation of graphite as first demonstrated by Novoselov et al. [1]. We have peeled off flakes from natural graphite<sup>1</sup> with blue Nitto tape<sup>2</sup>. It has just enough adhesion to peel off graphite with minimal glue contamination. About 10 to 20 times of successive peeling of a graphite chunk of  $\sim 3$  mm is enough to spread graphite over an area of approx.  $25 \times 25$  mm<sup>2</sup>, this is shown in Fig. 3.1a-c. On that area we press quite firmly a  $19 \times 19$  mm<sup>2</sup> diced Si/SiO<sub>2</sub> substrate on the tape. We then release carefully the tape, as in Fig. 3.1d. A part of the graphite remains on the substrate, shown in Fig. 3.1e. Graphite and graphene are randomly distributed and need to be searched with an optical microscope. An example of graphite on SiO<sub>2</sub> is shown in Fig. 3.1f.

---

<sup>1</sup>NGS Naturgraphit GmbH

<sup>2</sup>SWT 20+ Nitto Dekko Corp.

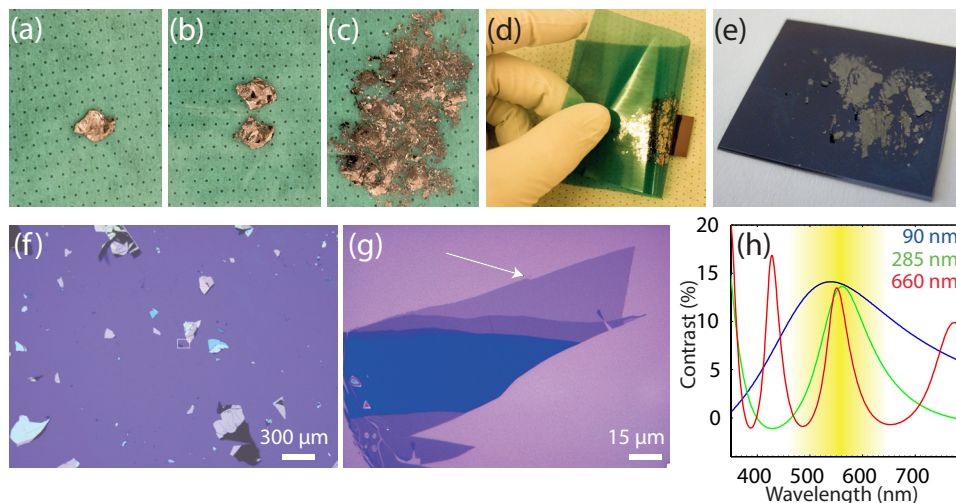


**Figure 3.1:** (a) A graphite chunk of  $\sim 3$  mm on blue tape. (b,c) This chunk is exfoliated. (d) The tape is pressed onto a Si/SiO<sub>2</sub> substrate and gently released. (e) The resulting graphite on a chip after exfoliation. (f) Small graphitic flakes under an optical microscope at 5x magnification. (g) Monolayer graphene is indicated by the arrow. (h) The resulting contrast as function of wavelength for different oxide thicknesses. The yellow bar indicates at which wavelengths the human eye is most sensitive to contrast.

### 3.2.1 Visibility of Graphene

Graphene monolayers made by the exfoliation method are typically of the size of 1 – 30  $\mu\text{m}$  and are searched with an optical microscope<sup>3</sup>. Finding monolayer flakes larger than 5  $\mu\text{m}$  is most efficient with 20x magnification, for smaller flakes we need 50x or 100x. In Fig. 3.1g a 100x magnification image of a typical graphene monolayer is shown.

The thickness of the SiO<sub>2</sub> top layer determines the contrast of graphene [24]. A thickness of 90 nm oxide has the best contrast. However, 285 nm oxide gives also a decent contrast. In some more recent experiments 660 nm oxide was used in order to minimize the chance of electrical leakage through the oxide<sup>4</sup>. With the same method as in Blake et al. [24] we calculated the optical contrast as function of wavelength for different thicknesses of SiO<sub>2</sub>, given in Fig. 3.1h. Under white light illumination the human eye is most sensitive to green ( $\sim 550$  nm) light [101], and therefore oxide thicknesses of 90, 285 and 660 nm give optimal contrast.

In some cases graphene is prepared on other substrates than SiO<sub>2</sub>, such as on thin polymer films, such as PMMA<sup>5</sup>. The contrast is optimised by the right thickness according to the index of refraction of the particular polymer used.

<sup>3</sup>Olympus BX51.

<sup>4</sup>We have encountered quite some back gate leakages through the oxide. A thicker oxide minimized this. But switching to other metals, such as sputtered tungsten (W) also reduced leakages presumably occurring during ultrasonic wire bonding.

<sup>5</sup>PMMA stands for Polymethylmethacrylate.

## 3.3 Characterization Methods

Here we discuss the most common characterization methods that are used for the experiments described in this thesis.

### 3.3.1 Atomic force microscopy

Atomic force microscopy (AFM) is used to look at the surface topography of graphene and hexagonal Boron Nitride (hBN) at a sub-nanometer height resolution. This is done in tapping mode, where the tip oscillates and is never in contact with the surface. With this method we are able to extract the layer thickness of graphene and hBN and so the number of atomic layers. A typical height measurement is shown in Fig. 3.5.

Another possibility is to judge whether graphene or hBN is sufficiently clean. For that we record the amplitude-error, which is sensitive to height differences and is more suitable for topography measurements. The value of the amplitude is related to the setpoint and is cantilever specific, thus the color scale is meaningless and usually omitted. A typical image is shown in Fig. 3.6.

For surface scanning we have used a Veeco Nanoscope IIIa in tapping mode with Olympus OMCL-AC160TS-W2 tapping mode cantilevers. The mechanical cleaning is done in contact mode and stiffer cantilevers are used, Olympus OMCL-TR800PSA-1.

A concise introduction to atomic force microscopy is found in the introduction of a review by Giessibl [102].

### 3.3.2 Raman microscopy

We can use Raman microscopy to determine the number of layers of graphene. Raman scattering is inelastic photon scattering. An incident photon excites an electron from the ground state to a virtual state, which subsequently makes a transition to a higher vibrational state than it started in, thereby emitting second photon. The scattered photon has a slightly lower energy than the incident one, this is called Stokes Raman Scattering<sup>6</sup>. The energy difference or Raman shift corresponds to the energy of a certain vibrational mode of the lattice. The scattered light is led through a narrow band-pass filter (notch filter) to a spectrometer. The notch filter blocks only the incident (excitation) wavelength. The resulting light is measured in a spectrometer.

A typical spectrum of monolayer graphene is given in Fig. 3.2. Here two resonances are visible: the so-called G mode ( $\sim 1580 \text{ cm}^{-1}$ ) and 2D mode ( $\sim 2690 \text{ cm}^{-1}$ ). The G mode is the stretching-bond mode of pairs of  $\text{sp}^2$ -bond carbon atoms, which involves an intra-valley one-phonon process. This mode is always present in graphene and does not require sixfold rings.

In the case of defects or close to edges the D mode (defect related mode) appears, shown in the upper curve at  $\sim 1350 \text{ cm}^{-1}$ . This spectrum is of a monolayer with disorder. The D mode is a breathing mode of a sixfold ring and is not allowed for

---

<sup>6</sup>The reverse is also possible and is called Anti-Stokes Raman scattering. Here an electron is already in an excited vibrational state makes the transition to the ground state via a virtual state. Anti-Stokes resonances are in general weaker than Stokes and in this thesis we solely look at Stokes resonances.

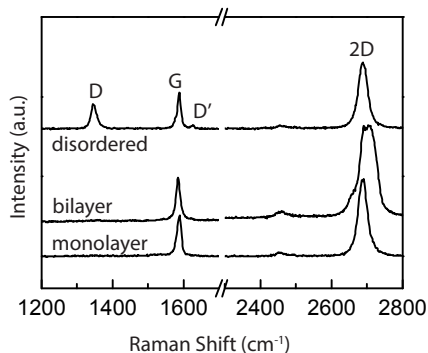


**Figure 3.2:** Bottom curve: Typical Raman spectrum for monolayer graphene, with its G and 2D mode. Middle curve: The Raman spectrum for bilayer graphene. Top curve: Raman spectrum of defected graphene, where a defect (D-mode) is present.

the case of pristine (defect free) graphene. The D mode is only observed near edges and when graphene is defected<sup>7</sup>. In the latter case a low charge carrier mobility is expected.

Even in absence of disorder the second order of the D mode is visible, this is the 2D mode. The 2D mode is a doubly resonant process carried by two phonons and does not require a defect for its activation.

The spectra of monolayer and bilayer are quite distinct from each other. Raman is a good quantitative measurement for making a distinction. Their 2D mode differs in intensity (with respect to the G mode) and shape. In monolayer graphene the 2D is a sharp resonance, but in bilayer graphene the peak splits off in four overlapping peaks [103]. The origin of these four peaks is the electron dispersion splitting in bilayer graphene. Multi-layer graphene or graphite also show asymmetric 2D resonances in their Raman spectra. In this way we are able to distinct monolayer from bilayer and multi-layer graphene. Raman is a non-invasive and quick measurement, which makes it a powerful method for characterizing the number of layers in graphene. For good reviews about Raman spectroscopy on graphene we refer to Malard et al. [104] and more recently Ferrari and Basko [105].

In almost all our experiments we have used a Renishaw InVia system with a 514 nm Ar laser. The laser spot size is diffraction limited with a maximum power of 10 mW applied.

### 3.4 Electron-beam lithography

The devices discussed in this thesis are quite diverse, and involve diverse fabrication procedures. In this section the fabrication methods are explained that are in common for most of the experiments.

<sup>7</sup>for instance by the presence of  $sp^3$  bonds or vacancies.

### 3.4.1 Contacting graphene

Electron-beam lithography is used to define contacts in PMMA thin films (100-300 nm thick) with an electron-beam pattern generator, EBPG (Vistec EBPG5000+HR B017). The acceleration voltage is 100 kV. Small features (100 nm) are written with typically 1-5 nA beam currents yielding a spot size of  $\sim 20 - 40$  nm and for coarse features ( $> 3 \mu\text{m}$ ) a beam current of 100 nA is used which gives a spot size of  $\sim 100$  nm. For 100-300 nm thick PMMA films a dose of  $1200 \mu\text{C cm}^{-2}$  is sufficient exposure for regular structures<sup>8</sup>. This is illustrated in Fig. 3.3a.

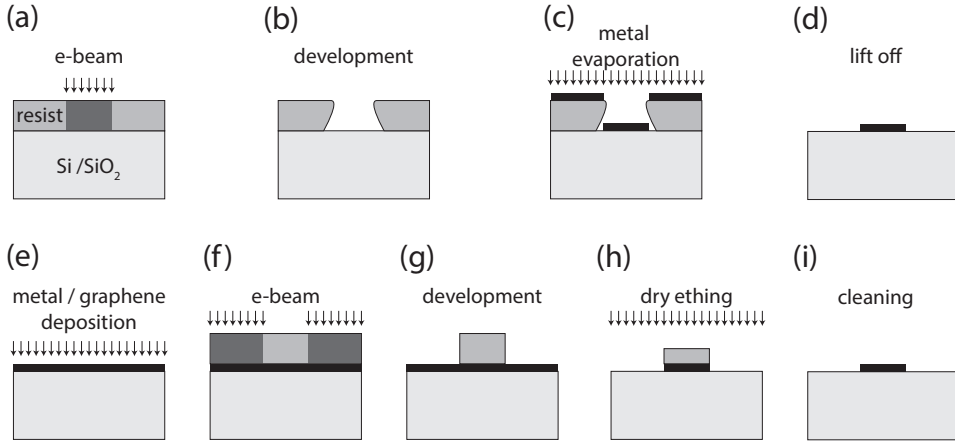


**Figure 3.3:** Standard electron beam lithography techniques. (a) A resist layer is exposed by e-beam. (b) It is chemically developed where the exposed area is removed (positive resist). (c) Metal is evaporated or in some cases sputtered. (d) The metal/resist film is lifted off. (e) Metal (usually sputtering) or graphene is deposited. (f) Etching mask defined by e-beam. (g) The mask is developed and (h) subsequently (dry) etched. (i) The mask is cleaned in acetone, in case of PMMA.

The exposed chips are developed in a 1:3 mixture of MIBK:IPA<sup>9</sup> for at least 30 sec, usually 2 min and rinsed in IPA to stop the development, Fig. 3.3b.

Contacts are made by e-beam evaporating from a metal target onto the chip with the developed mask, Fig. 3.3c. This is then lifted off, Fig. 3.3d. Au or AuPd contact graphene sufficiently well. To improve the adhesion on  $\text{SiO}_2$ , a thin ( $\sim 3$  nm) film of Ti is used as sticking layer. On different substrates, in particular hexagonal Boron Nitride (hBN), Ti is not suitable as adhesion layer, so we use Cr instead. Cr can diffuse quite easily in Au at elevated temperatures. This can be prevented by adding a stop layer of Pd ( $\sim 4$  nm). So the resulting stack to contact graphene is Cr/Pd/Au and sustains temperatures up to at least  $250^\circ\text{C}$ .

<sup>8</sup>For less common structures such as thin lines or entirely exposed areas it is necessary to adjust the dose for compensating proximity effects. In addition the ebeam software has an algorithm for proximity effect correction.

<sup>9</sup>MIBK is 4-methyl-2-pentanone or Methyl isobutyl ketone, IPA is isopropanol.

### 3.4.2 Etching graphene and bottom split gates

Local bottom gates are made by sputtered tungsten (W), Fig. 3.3e, where the patterned resist acts as an etch mask. The areas of the resist that are to be removed are exposed<sup>10</sup>, Fig. 3.3f. After development, Fig. 3.3g, the tungsten is dry etched in a plasma, Fig. 3.3h. At last the etch mask is cleaned, Fig. 3.3i.

There are numerous advantages for using W: (1) It can sustain very high temperatures (up to 600 °C or even higher<sup>11</sup>); (2) The films are in general smoother compared to evaporated metals; (3) Etching of W can be done very anisotropically in our etching system, which can yield well defined e-beam markers and very small gaps between gates (resulting in split gates); (4) Ultra sonic bonding on W has a higher success rate than i.e. Ti/Au. Usually less power is needed, which reduces the chance to damage the oxide.

Graphene is etched by reactive ion etching (RIE) in an O<sub>2</sub> plasma. It is very similar to the process of metal etching where we start with graphene instead of metal, Fig. 3.3e. With an e-beam defined pattern in PMMA we can etch graphene in a desired shape, Fig. 3.3f. The following conditions<sup>12</sup> are sufficient to etch graphene: 30 sec, 25 sccm O<sub>2</sub>, 50  $\mu$ bar and 20 W power, Fig. 3.3h. The etch rate of PMMA is  $\sim 3$  nm/s. This means that a mask of at least 100 nm thick is necessary. The etch mask is cleaned in acetone, Fig. 3.3i.

## 3.5 Transfer

In this section we will discuss transfer methods for graphene and hBN. We have developed our own water-based method, which is treated in full detail in Chapter 4. Here we discuss our version of a dry transfer method<sup>13</sup> adapted from Ref. [32].

### 3.5.1 Substrate effect

The electronic quality of graphene is strongly determined by its underlying substrate. Graphene on SiO<sub>2</sub> has charge carrier mobilities of  $\sim 2000 - 6000$  cm<sup>2</sup> V<sup>-1</sup> s<sup>-1</sup>, four orders lower than its intrinsic value of  $\sim 10^7$  cm<sup>2</sup> V<sup>-1</sup> s<sup>-1</sup> [9]. This is due to charged impurities present in the oxide. And secondly when graphene conforms the rough surface of SiO<sub>2</sub> it becomes more reactive to form sp<sup>3</sup> bonds, leading to short range scatterers [106, 107]. By removing the substrate below and thus suspending graphene the charge carrier mobility is improved by two orders of magnitude,  $\sim 2 \cdot 10^5$  cm<sup>2</sup> V<sup>-1</sup> s<sup>-1</sup> [30].

Another possibility is to replace the SiO<sub>2</sub> substrate by one that is inert and atomically flat, such as hBN flakes. This has first been demonstrated by Dean et al. [32], where the authors show a charge carrier mobility of  $\sim 60000$  cm<sup>2</sup> V<sup>-1</sup> s<sup>-1</sup>. More recently, graphene encapsulated in hBN has been found by Mayorov et al. [34] to exhibit ballistic transport over a  $\sim 1$   $\mu$ m at room temperature. Although graphene on hBN

<sup>10</sup>In case of negative resist, such as NEB, we expose the areas that are not removed.

<sup>11</sup>This is not the case in ambient air, only in vacuum or in Ar/H<sub>2</sub>.

<sup>12</sup>Recently we found that 12 sec, 25 sccm O<sub>2</sub>, 50  $\mu$ bar and a power of 10 W is also sufficient for etching graphene. Longer timing and higher power may result in over-etching and damaging edges.

<sup>13</sup>“Dry” means here that the graphene is never in contact with water or solvents.

shows most of the time lower charge carrier mobility than suspended, it is much more practical for device fabrication, as free hanging graphene is very fragile. To stack graphene onto hBN we need an ultra-clean (i.e. no water) transfer method.

### 3.5.2 Dry transfer methods

Here we describe a method for transferring exfoliated hBN onto local bottom gates. This method can be equivalently used for exfoliated graphene stacking onto hBN.

hBN is prepared on a Si substrate coated with a PVA/Elvacite film by mechanical exfoliation using the blue Nitto tape. Optimal contrast for observing thin hBN flakes is optimised by the right<sup>14</sup> thickness of PVA<sup>15</sup> and Elvacite<sup>16</sup>. A 0.25 mm thick Lexan frame is stuck by double-sided tape to the Elvacite side, illustrated in Fig. 3.4a. Next the sacrificial PVA film is dissolved in H<sub>2</sub>O to release the Elvacite film from its substrate. The result is illustrated in Fig. 3.4b, where the frame with the Elvacite polymer is floating on water with the graphene facing up. It is gently taken out and dried. The frame with film is attached to a micro-manipulator. The hBN can be observed from the bottom in an optical microscope and is aligned onto the target substrate, Fig. 3.4c. During the transfer the stage is heated to 80 °C above the glass transition temperature of Elvacite (36 °C). Once the film is molten on the surface, the target substrate with film is peeled off the frame and left on a hot plate at 80 °C for at least an hour to improve adhesion of the hBN to the substrate. The polymer film is then removed by dissolving it in acetone. hBN is then cleaned by oven annealing (Sec. 3.6.2).

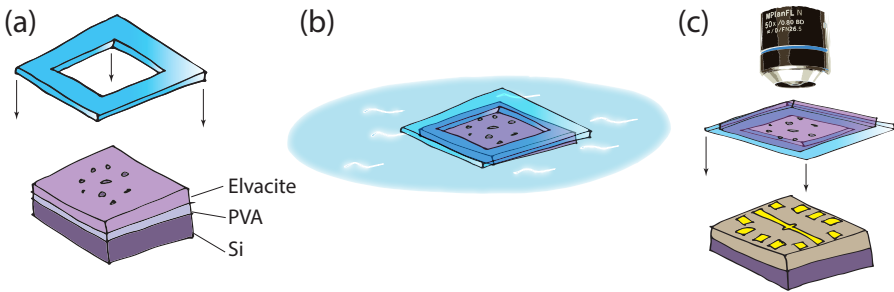


**Figure 3.4:** (a) A Lexan frame is hand cut and stick to the Elvacite side of the stack. (b) Next it is put in water, in order to dissolve the PVA film, which detaches the Elvacite from the substrate. (c) The frame with film is transferred upside down onto a second substrate with a gate structure, while aligning under optical microscope.

CVD graphene on Elvacite films are transferred in a similar way, which is described in more detail in Chapter 9.

<sup>14</sup>The optimisation is not very precise. We usually aim for a colour close to purple right after the spin coating of the layers.

<sup>15</sup>Polyvinyl alcohol in 6 wt% H<sub>2</sub>O, Sigma Aldrich 360627.

<sup>16</sup>Elvacite 2550 Acrylic Resin dissolved in MIBK, Lucite International, Inc. See Ref. [33]



## 3.6 Cleaning Graphene

Polymer residues tend to stick to graphene surfaces. This lowers the electron mobility considerably and therefore it is ultimately necessary to remove these residues. In this section we discuss possible solutions to clean graphene from residues.

### 3.6.1 Chemical cleaning

Most of the polymer films (PMMA, MMA, Elvacite, etc) on graphene and hBN are removed by acetone. However, a thin residue will stick to the surface which then needs to be removed by other methods. An AFM image of a surface with residues is shown in Fig. 3.5a. Attempts using chloroform or dichloroethane were not as successful as reported by Ref. [108].

### 3.6.2 Oven annealing

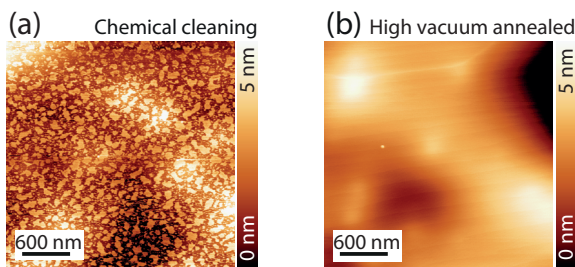


**Figure 3.5:** (a) An AFM image of a hBN surface after only acetone cleaning. Polymer residues are clearly visible. (b) The result after high vacuum annealing

Residues are usually successfully removed by oven annealing in forming gas Ar/H<sub>2</sub>. The samples are placed inside a  $\sim 1$  inch quartz tube. A mixture of Ar/H<sub>2</sub> 600/400 sccm is led through the tube. The tube with samples inside is placed in a tube oven, Lundberg Blue M. The temperature is set to at least 250 °C with an up-rate of 7 °C/min. In some cases this is sufficient, if not we repeat the process at 300 °C. Devices without gold are not limited by  $\sim 300$  °C and usually annealed up to 550 °C.

Oven annealing in high vacuum ( $< 10^{-6}$  mbar) at  $\sim 600$  °C effectively removes residues on hBN surfaces. In Fig. 3.5a an AFM image is shown of a hBN surface right after transfer, where it is only cleaned in acetone. Polymer residues are clearly visible. In Fig. 3.5b the result after annealing in high vacuum is shown.

For annealing graphene/hBN stacks it is possible to apply higher temperatures than on graphene solely on SiO<sub>2</sub>. We have routinely annealed graphene/hBN stacks up to  $\sim 600$  °C in either high vacuum or in forming gas. In Raman no D-mode is measured, in contrast to graphene on SiO<sub>2</sub>. After such treatment wrinkles and bubbles often are found, which is discussed in Sec. 3.7.

Another possibility to remove organic residues is to perform current-induced annealing [10]. We pass a large current through a graphene device,  $\sim 1$  mA  $\mu\text{m}^{-1}$ , which

generates enough heat in the graphene to anneal itself. We have performed current-induced annealing in various experiments, but we were never able to reach a desired result with consistency.

### 3.6.3 Mechanical cleaning

Mechanical cleaning is done by sweeping an AFM tip in contact mode over the graphene surface and proved to be effective to clean up residues. This method is developed by us and described in full detail in Chapter 8.

In Fig. 3.6a we show a graphene Hall bar device on hBN that has been etched and mechanically cleaned to the extent that no damage was done. Most organic residues (here MMA) are displaced aside on the hBN surface. To illustrate the surface mobility of organic residues during heating, it is put on a hotplate for only 10 min at 300 °C. An AFM image in Fig. 3.6b shows that residues have moved back onto the graphene. Next an annealing step in Ar/H<sub>2</sub> at 500 °C is done with the purpose to remove again the organic residues. In Fig. 3.6c the result is given. Here we would have expected most organic residues to be gone, but the AFM image shows no improvement at all. The organic residues are stuck on the graphene surface and annealing has no effect anymore. Most likely heating in air at 300 °C chemically modifies the residues to an extent that it is no longer possible to remove them by oven annealing. Depending on the process that has been undergone, oven annealing is not always effective.

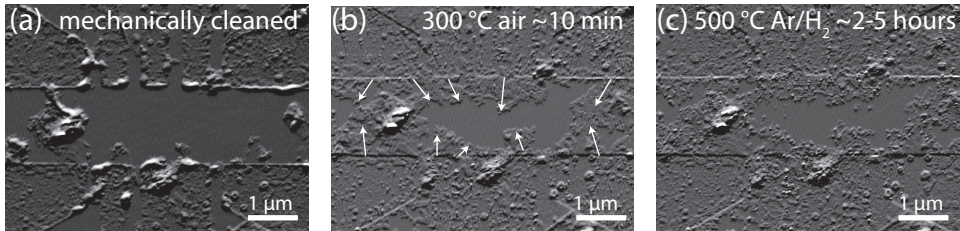


**Figure 3.6:** (a) An AFM image of a mechanically cleaned surface of a Hall bar. (b) An AFM image of the result after a short time in air at 300 °C. (c) Subsequent annealing in forming gas at 500 °C has no effect.

## 3.7 Bubbles and wrinkles in graphene

Bubbling and wrinkling of graphene on various surfaces is a commonly observed phenomenon by many groups. Since there are various causes we make here a distinction between different types:

- **Wrinkles due to wet transfer.** They have been observed by us and are treated in detail in chapter 5.
- **Wrinkles in CVD graphene from Cu during growth.** The origin is a mismatch in thermal expansion coefficient between copper and graphene. The growth occurs at high temperatures, typically  $\sim 1000$  °C. During cool down

copper shrinks<sup>17</sup>, while graphene expands<sup>18</sup>, leading to bulging and wrinkling. The typical size of these wrinkles is  $\sim 1$  nm in height and width with an inter-distance of  $\sim 10 - 50$   $\mu\text{m}$ . When the graphene sheet is subsequently transferred the wrinkles maintain.

- **Wrinkles and bubbles in graphene on hBN.** This type of wrinkles and bubbles are often seen in graphene that is transferred onto hBN. It is only seen in graphene on hBN and not in the same graphene on  $\text{SiO}_2$ . Its exact origin is at time of writing under debate. Here we will discuss further this type.

### 3.7.1 Wrinkles and bubbles in graphene on hBN

CVD graphene that is transferred onto hBN shows typical wrinkling. Initially we have used a wet transfer method for transferring CVD graphene. In Fig. 3.7a an AFM image is taken of such a surface. Wrinkles and bubbles appear in somewhat different shapes and on the flat areas a rougher surface than usual is measured (0.9 nm rms roughness). This suggests that residues are likely to be present underneath. Next to prevent or minimize contamination from residues, we employed a dry transfer method with CVD graphene. The result is shown in Fig. 3.7b. Similar network is formed as is routinely observed in exfoliated graphene that is transferred with a dry method by others [111]. In between the wrinkles and bubbles the RMS roughness is estimated to be 1.9 Å which is the limit of the AFM height resolution, which does not exclude an atomically flat surface.

Haigh et al. [112] have revealed that energy dispersive X-ray (EDX) and electron energy loss spectroscopy (EEL) measurements in a cross section of a bubble mainly consists of hydrocarbons. We note that this observation cannot exclude the possibility that these hydrocarbons occupy the bubble after cutting it through.

Next we will illustrate its spurious formation without being able to clarify the source of hydrocarbons. In Fig. 3.7c an optical microscope image of exfoliated graphene monolayer is shown. The graphene monolayer flake is on a Elvacite surface, which can be subsequently transferred onto hBN. But before that we have taken an AFM image to find out whether residues are already present on the graphene surface. In the inset an AFM image is shown and the RMS roughness is below the height resolution of the AFM. It is clear that there are no residues present at all before transfer. In Fig. 3.7d the monolayer graphene is transferred onto a hBN flake. In the inset an AFM image shows wrinkling on the hBN surface. The hBN had undergone a similar annealing treatment as in Fig. 3.5b.

We observe that two clean surfaces of graphene and hBN still yield wrinkles and bubbles after transfer. The source of hydrocarbons is not clear. One possibility is that during transfer once the polymer scaffold is in close contact with the target substrate polymer residues diffuse onto the graphene due to mild heating of  $80^\circ\text{C}$ . Another possibility, less likely though, is that there are actually small amounts of contaminants present on the surfaces, with a roughness below the resolution of the AFM height resolution. Another explanation could be a strong friction force between graphene and

<sup>17</sup>Copper has a linear thermal expansion coefficient of  $16.5 \times 10^{-6}\text{K}^{-1}$  [109].

<sup>18</sup>Graphene has a negative linear thermal expansion coefficient of  $-8 \times 10^{-6}\text{K}^{-1}$  [110].

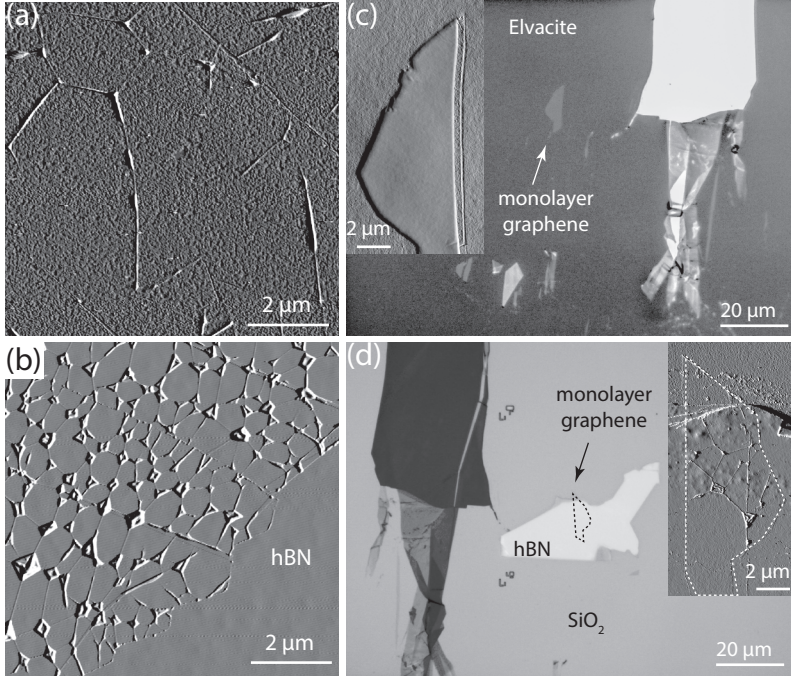


**Figure 3.7:** (a) An AFM image of wet transferred CVD graphene. (b) An AFM image of dry transferred CVD graphene. (c) exfoliated graphene on Elvacite before transfer with in the inset an AFM image of the monolayer. (d) Monolayer graphene is transferred onto hBN with in the inset an AFM image. Wrinkles and bubbles have appeared.

hBN combined with the mismatch between thermal expansion coefficients of graphene and hBN<sup>19</sup>, as is claimed by Pan et al. [114].

### 3.8 Measurement Setup

Electrical measurements are initially carried out in a room temperature probe station to test the device quality. To do low temperature measurements the chip is glued with silver paint to a chip carrier and wires are connected with an ultra-sonic bonding machine, West-Bond. In some cases the chip with bonds is oven annealed again at 250 °C to reduce doping from contaminants and hydrocarbons. The carrier is mounted in a socket and connected to the wiring of the cold finger, as shown in Fig. 3.8b. Low temperature measurements are done in a Leiden Cryogenics MCK-50 <sup>3</sup>He/<sup>4</sup>He dilution fridge. The setup is equipped with a superconducting magnet<sup>20</sup>.

In Fig. 3.8a, a photo of the cold finger with a sample connected is shown. It hosts 24 wires that are optimised for low-noise DC measurements. The wires are led through an RC filtering stage (10 kHz - 500 MHz) and next through copper powder filters<sup>21</sup>

<sup>19</sup>The linear thermal expansion coefficient is  $-2.9 \times 10^{-6} \text{ K}^{-1}$  at room temperature Ref. [113].

<sup>20</sup>Up to 12 T at 4K with a magnet power supply SMS Cryogenics Bipolar 5V 120A, Cryogenics Ltd.

<sup>21</sup>In total six Cu powder filters are used, each containing four manganin wires, 50 cm long, twisted

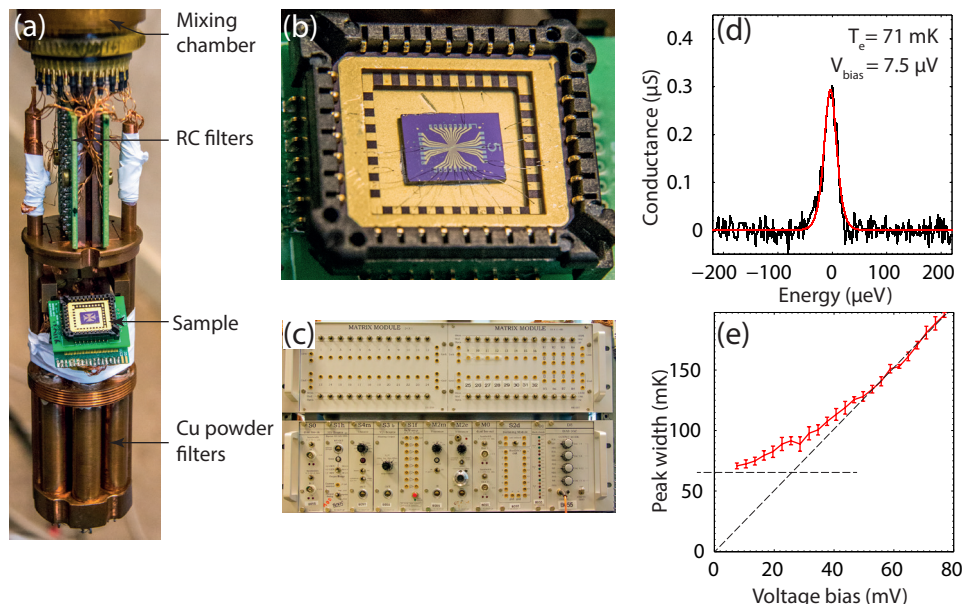


**Figure 3.8:** (a) a photo of the cold finger of the low-temperature setup. Mixing chamber is located at the top. RC filters and Cu powder filters are necessary for low-noise DC measurements. (b) a close-up of a sample with bond wires in a chip carrier. (c) IVVI rack, our home-built measurement equipment. (d) A Coulomb oscillation in electrostatically defined quantum dot in GaAs/AlGaAs heterostructure. From the shape and width of the Coulomb oscillation we estimate a electron temperature of 71 mK. (e) The peak width as a result from the fits as function of the applied voltage bias. The peak width saturates to the electron temperature at zero bias.

(10 MHz - above 40 GHz). At room temperature the wires pass a  $\pi$ -filter (10 MHz - 10 GHz). The DC resistance of a wire is measured to be 2.53 k $\Omega$ . A copper cylinder encloses the sample space, that acts as a Faraday cage (not shown in the photo).

Electrical measurements are done with a battery-powered, home-built measurement equipment, the so-called 'IVVI'-rack<sup>22</sup>, Fig. 3.8c. A voltage source or a current source module can be inserted and are controlled by DAC's (digital analog converters). These components are galvanically isolated from peripheral equipment in order to avoid any interference. Voltages and currents are measured with a voltage amplifier and an I-V converter respectively and are as well galvanically isolated and communicate optically. The resulting voltages are recorded either with a digital multimeter<sup>23</sup> or a lock-in amplifier<sup>24</sup>.

In this experimental setup a base temperature of  $\sim 35$  mK is reached. For measuring the electron temperature<sup>25</sup>  $T_e$ , we have used a GaAs/AlGaAs quantum dot

in pairs in Cu powder, the tube diameter is 10 mm and the length is 54 mm.

<sup>22</sup>Designed and made by R. Schouten. Specifications can be found here: <http://qtnwork.tudelft.nl/~Schouten/>

<sup>23</sup>Keitley 2700.

<sup>24</sup>Stanford SRS 830.

<sup>25</sup>The temperature defined by the broadening of the Fermi-Dirac distribution.

calibration sample. A quantum dot is electrostatically formed by top gates. We intentionally tuned thick energetic tunnel barriers<sup>26</sup> and measure transport through the quantum dot. A voltage bias of  $V_{bias} = 7.5 \mu\text{V}$  across the quantum dot is applied and a current is measured. In Fig. 3.8d conductance as function of gate energy is measured through a quantum dot, where a Coulomb oscillation<sup>27</sup> is recorded. The gate energy is set by the gate, that controls the energy levels inside the quantum dot. A  $1/\cosh^2(E/2.5kT_e)$  function<sup>28</sup> is fitted and yields an electron temperature of  $T_e = 71 \text{ mK}$ . A possible voltage offset of a few  $\sim \mu\text{V}$  from the voltage amplifier has not been subtracted. In Fig. 3.8e we show the peak width from fits as function of the voltage bias. At low bias the peak width approaches the electron temperature, which is close to the value found in Fig. 3.8d. This result is in very close agreement with measurements in other devices in the same setup, see Ref. [111].

---

<sup>26</sup>The tunnel rates are small compared to the thermal broadening ( $\hbar\Gamma \ll kT$ ).

<sup>27</sup>When the energy level is aligned with the chemical potentials in the leads, transport occurs through sequential tunneling and it is measured as an increase in the conductance, which is called a Coulomb oscillation or Coulomb peak. From the shape of the Coulomb oscillation we can extract whether transport is determined by the barriers itself or by the thermal broadening of the 2DEG in the leads [115]. In this case it is determined by the thermal broadening.

<sup>28</sup>This function applies in the classical regime where the level quantization energy is negligible compared to the temperature broadening and charging energy, see Ref. [115].



---

## CHAPTER 4

---

# Wedging Transfer of Nanostructures

G. F. Schneider, V. E. Calado, H. Zandbergen, L. M. K. Vandersypen  
and C. Dekker

In this chapter, we report a versatile water-based method for transferring nanostructures onto surfaces of various shapes and compositions. The transfer occurs through the intercalation of a layer of water between a hydrophilic substrate and a hydrophobic nanostructure (for example, graphene flakes, carbon nanotubes, metallic nanostructures, quantum dots, etc) locked within a hydrophobic polymer thin film. As a result, the film entrapping the nanostructure is lifted off and floats at the air-water interface. The nanostructure can subsequently be deposited onto a target substrate by the removal of the water and the dissolution of the polymeric film. We show examples where graphene flakes and patterned metallic nanostructures are precisely transferred onto a specific location on a variety of patterned substrates, even on top of curved objects such as microspheres. The method is simple to use, fast, and does not require advanced equipment.

## 4.1 Introduction

### 4.1.1 Motivation

In applications ranging from soft lithography [116] to three-dimensional electronics [117], the controlled transfer of nanostructures from one substrate to another is crucial [118]. Despite the fact that nanofabrication methods have advanced substantially [119], there is no general and robust approach yet available for transferring and precisely aligning (nano)structures onto a specific device with submicrometer precision. Existing transfer methods are often limited in scope because they suffer from process-specific drawbacks, such as optimizing the pressing force versus chemical adhesion (for transfer printing by stamping) [120–123], the use of reactive chemicals (in lift-off by etching) [73, 124–127], the use of irreversible mechanical stripping methodologies (e.g. peeling) [128–130] to separate two solid surfaces brought in contact, or

---

This chapter is based on the paper titled ‘Wedging Transfer of Nanostructures’ *Nano Letters* **10**, 1912-1916 (2010).



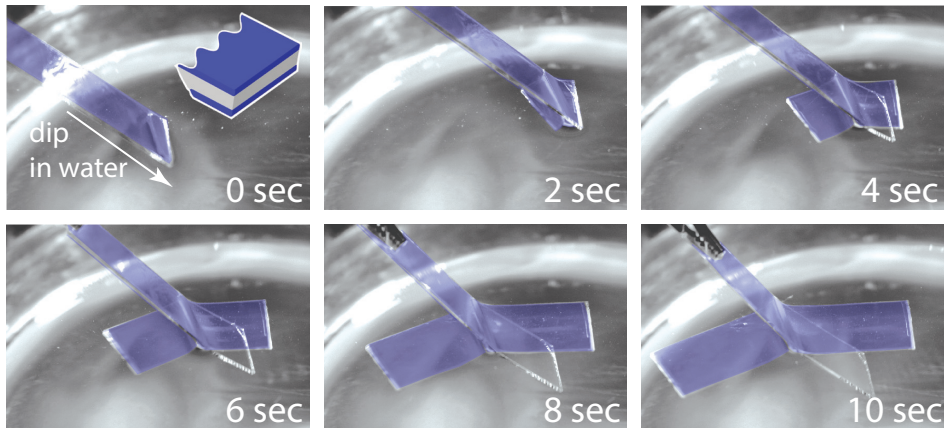


**Figure 4.1:** Time-lapse optical imaging of the simultaneous wedging of two hydrophobic polymer layers that were deposited on both sides of a microscope glass cover slip.

exposure to high temperatures needed for baking polymer sticking layers or for releasing thermal adhesives [131]. This list is not exhaustive but is representative of the most popular techniques used for transferring.

### 4.1.2 Wedging principle

The technique that we introduce here, wedging transfer, is versatile, suitable for transfer onto many different type of substrates, including curved surfaces, and intrinsically combines transfer and alignment. The technique is based on the simplest view of the hydrophobic effect [132, 133]: water wets hydrophilic surfaces and avoids hydrophobic ones [134, 135], and is inspired from methods generally used to prepare polymer-coated transmission electron microscopy grids [136]. As we will demonstrate, this implies that water can lift off a hydrophobic object from a hydrophilic substrate. For instance, a graphene monolayer flake can be lifted off and transferred from one substrate to another one, simply by using water as the active-transfer component.

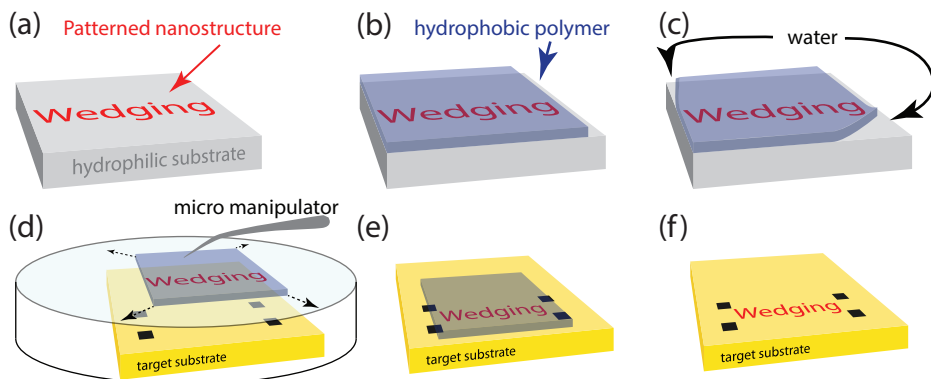
## 4.2 Glass slide example

Fig. 4.1 depicts the principle of the wedging transfer. A microscope glass slide is coated on both sides with a cellulose acetate butyrate polymer thin film (see Sec. 4.7). Dipping the slide into water releases the polymer film from the glass slide. As a result, the polymer film floats on water. The wedging is observed to work for at least two incidence angles, here  $\sim 30^\circ$  and  $\sim 150^\circ$  between the polymeric films and the water meniscus. The wedging process is found to be intrinsically reversible: by retracting the glass slide again from water, the polymer film is re-deposited on the initial substrate (data not shown). The physical driving force yielding the lift-off is the capillary force exerted by water that invades the hydrophilic/hydrophobic interface, resulting in the dynamic separation of both surfaces. The wedging only depends on

the kinetics and thermodynamics of water invasion, and is therefore independent of the experimentalist's skills: wedging will always occur if the experiment is performed slowly enough (few seconds as a time scale).

### 4.3 Transfer & alignment

The wedging principle can be used for transferring nanostructures, as schematically illustrated in Fig. 4.2. In Fig. 4.2a a hydrophobic pattern (e.g., the word WEDGING) that has been fabricated on a hydrophilic substrate (such as glass, quartz, mica,  $\text{SiO}_2$ ) is dipped into a solution of a hydrophobic polymer<sup>1</sup>, thus forming a solid polymer layer covering the pattern after the evaporation of the solvent at room temperature, Fig. 4.2b. Subsequently, the polymer film which now includes the pattern that is to be transferred is wedged in water and floats at the water/air interface because of surface tension forces, Fig. 4.2c. Transfer to the new location occurs when the water level is lowered enough for the polymer film to reach the receiver substrate, Fig. 4.2d. Once deposited onto a selected target spot of the receiver substrate (target markers shown in black in Fig. 4.2e, the polymer film is removed by dissolving it into the solvent used for its initial dissolution (here ethyl acetate), Fig. 4.2f.



**Figure 4.2:** Illustration of the handling steps involved in the wedging transfer technique.

### 4.4 Graphene transfer

As a first demonstration of our method, we transferred a flake of graphene [1, 46, 137–140]. While it is now a routine to obtain single-layer graphene by mechanical exfoliation of bulk graphite and to identify the single-layer flakes by means of their optical contrast against the bare substrate [24], one of the major drawbacks of this technique is that graphene flakes are arbitrarily distributed on the substrate. It would be of great use if specific flakes could be picked up from the substrate, and redeposited in a precise location on another substrate, for instance on top of prefabricated contacts,

<sup>1</sup>Cellulose acetate butyrate, 30 mg/mL in ethyl acetate, Sigma-Aldrich.

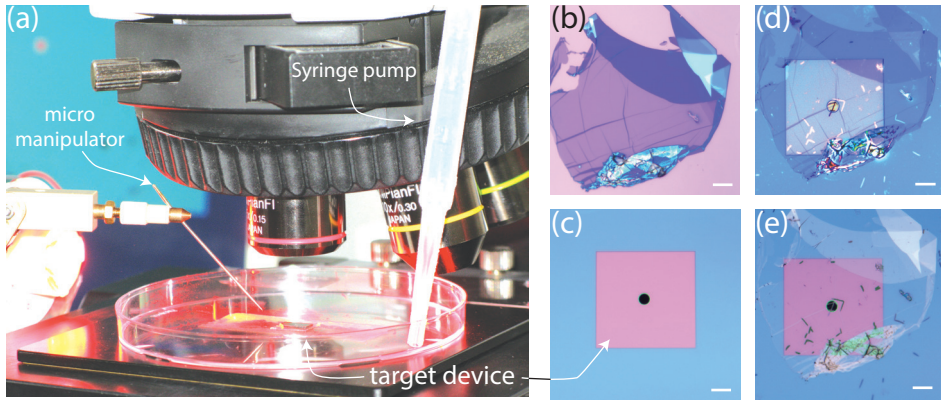


**Figure 4.3:** Demonstration of the wedging transfer technique with the controlled transfer of a multilayer graphene flake. (a) The experimental setup consists of a conventional low magnification optical microscope, and a standard sewing needle connected to a micrometric screw to precisely align the wedged polymer film (including the graphene pattern) on top of a target device. (b) Optical microscope image of a few graphene layers on a Si/SiO<sub>2</sub> wafer obtained through the standard mechanical-exfoliation method (oxide thickness of 285 nm). (c) The target device which is a SiN membrane with a 5  $\mu\text{m}$  diameter hole. (d) Graphene/polymer layer deposited onto the target device after the wedging and drying under ambient conditions. (e) Graphene flake on the target device after dissolution of the hydrophobic polymer film. Scale bars are 10  $\mu\text{m}$  in all images.

a TEM grid, or other fabricated nanostructures. Graphene thus is an excellent model material to demonstrate the applicability of the wedging transfer technique.

The wedging transfer and alignment of a graphene sample onto a target spot on the receiver substrate is depicted in Fig. 4.3. In our setup (Fig. 4.3a), we laterally moved the graphene flake (Fig. 4.3b) along the water/air interface by using a probe needle that contacts the polymer layer and thereby aligned the flake over the target spot (square pattern with a round hole of 5  $\mu\text{m}$  diameter, Fig. 4.3c). The probe needle is manually or electrically moved in the lateral and height directions with three orthogonal micrometric screws. Because of the high transparency of the film, we can use an optical microscope to align the position of the graphene flake with respect to the target with sub-micrometer accuracy. During the aligning, the water level in the Petri-dish is lowered using a syringe pump. Upon pumping out the water, the graphene is deposited onto the target spot of the receiver substrate. Its shape is preserved during the transfer (Fig. 4.3d), and, importantly, also after the dissolution of the polymeric scaffold (Fig. 4.3e). For example, we performed 49 wedging transfers with graphene so far. All flakes were always successfully transferred onto SiN and Si/SiO<sub>2</sub> receiver substrates (Fig. 4.4a), and also onto mica surfaces. Mica is difficult to use as a substrate for graphene with the mechanical exfoliation method, since layers of mica will also exfoliate when using the Scotch tape. Fig. 4.4b shows the successful wedging transfer of graphene onto mica, observed in the transmission mode of an optical microscope [141].

## 4.5 Versatility

We have explored the applicability of the wedging transfer to a variety of other structures. Figures 4.4c and 4.4d show examples of gold microelectrodes and gold nanostructures respectively. The polymer solution is supplemented with an aliphatic thiol<sup>2</sup>, to increase the sticking between the gold and the polymer. This enabled us to transfer with a success rate of 100%, gold microelectrodes patterned on Si/SiO<sub>2</sub> wafers<sup>3</sup>, onto substrates such as SiO<sub>2</sub> already covered with other microelectrodes (Fig. 4.4c). We also successfully transferred gold nanofabricated letters<sup>4</sup> onto highly curved objects such as polystyrene microspheres (Fig. 4.4d). Some nanostructures (~ 10%) were not fully transferred (note some missing letters), possibly because the polymer film is not elastic enough to conform totally to the curved object. Increasing the elasticity of the film can possibly be achieved by lowering the concentration of the polymer in the solvent or adding plasticiser molecules to the polymer.

## 4.6 Conclusion

We have developed the wedging transfer method that is simple, fast and versatile, and can readily be employed in a standard equipped lab.

As a final illustration of the extreme simplicity of the method, one can take a white board marker, write a line onto a microscope slide or a stainless-steel spoon, dip it into a glass of water and immediately see the line wedging and floating on top of water. Subsequently, the line can be redeposited with a backwards movement onto the original substrate, or onto another material. To the best of our knowledge, there are no other transfer techniques that are so effective and straightforward.

## Acknowledgments

This research was funded by the Netherlands Organisation for Scientific Research (NWO) and the Foundation for Fundamental Research on Matter (FOM).

## 4.7 Methods

### 4.7.1 Preparation for wedging transfer

A hydrophilic wafer is dipped in a solution of cellulose acetate butyrate (30 mg/mL in ethyl acetate). After dipping (the total dipping procedure lasts about three seconds), the substrate is removed from the polymer solution and the solvent is left to evaporate under ambient conditions. At this point in time, the edges of the substrate are still covered with the polymer (hindering the water to intercalate at the

---

<sup>2</sup>0.1 vol% of 1-dodecanethiol, Fluka Analytical Ref. #44130, a hydrophobic self-assembled monolayer will spontaneously form onto the gold surface [141]. This hydrophobic self-assembled monolayer increases the sticking between the polymer and the gold by means of the hydrophobic interactions.

<sup>3</sup>The gold is ebeam evaporated without a chromium or titanium sticking layer.

<sup>4</sup>70 nm line width, also in the presence of thiolates.

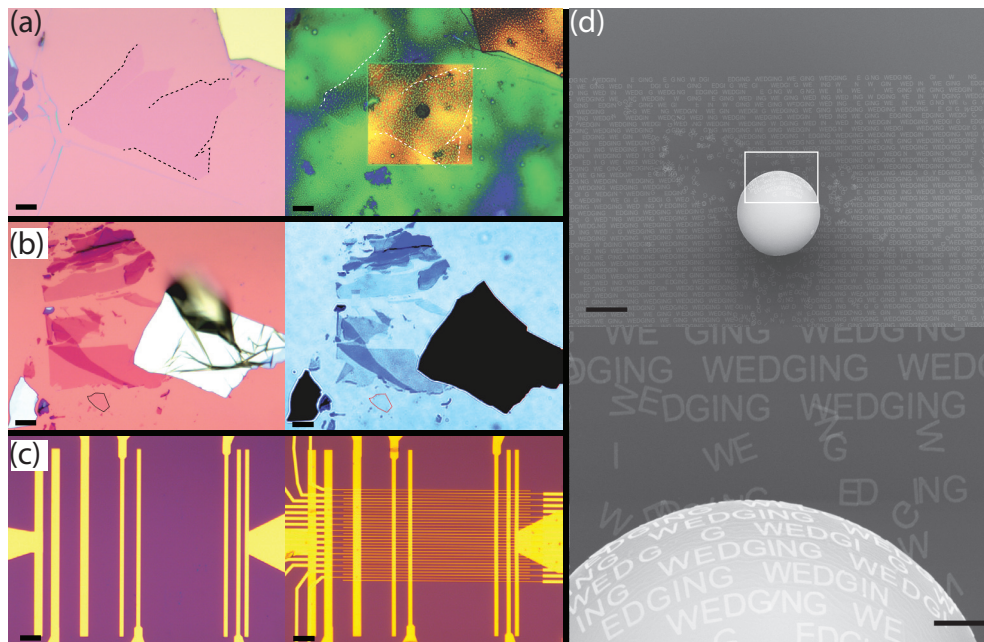


**Figure 4.4:** Four examples of wedging transfer of nanostructures. (a) Wedging transfer of a graphene monolayer from a Si/SiO<sub>2</sub> wafer (left) onto a SiN membrane with a patterned 5  $\mu\text{m}$  hole. The polymer film has not yet been dissolved (right micrograph) to enhance the contrast and the optical visibility of the monolayer onto the target substrate. Scale bar represents 10  $\mu\text{m}$ . (b) Wedging transfer of graphene multilayers (including a monolayer, see dashed lines pointed near the arrow) from a Si/SiO<sub>2</sub> wafer (left) onto mica, observed in the transmission mode of the optical microscope (right). Scale bar represents 10  $\mu\text{m}$ . (c) Scanning electron microscope image of patterned gold microelectrodes (left, smallest lines 2  $\mu\text{m}$  wide, 50 nm thick, without titanium sticking layer). These electrodes were transferred from a Si/SiO<sub>2</sub> wafer onto another Si/SiO<sub>2</sub> wafer that contained a previous pattern of perpendicularly oriented microelectrodes (smallest line 200 nm wide, 20 nm Ti, 50 nm gold). Scale bar represents 10  $\mu\text{m}$ . (d) Scanning electron microscope image of the letters WEDGING that have been transferred from Si/SiO<sub>2</sub> onto a 10  $\mu\text{m}$  diameter polystyrene microsphere (the scale bar is 5  $\mu\text{m}$ ). An enlargement of the square is shown on the right (the scale bar is 1  $\mu\text{m}$ ). The gold letters were made by e-beam lithography (see methods) and have 70 nm line width and 20 nm thickness.

hydrophilic/hydrophobic interface) [136]. Therefore, by using a cotton swab impregnated with the same solvent as the one used to solubilise the polymer, the edges are cleaned so that water can intercalate at both interfaces. Alternatively one can use a sharp razor blade and scratch the polymer at the edges of the wafer. Both methods yield indistinguishable results. The substrate is then dipped into water with an incidence angle of  $\sim 30^\circ$ .

### 4.7.2 Preparation of graphene samples

We prepared graphene sheets on clean and freshly plasma oxidized 285 nm Si/SiO<sub>2</sub> substrates (O<sub>2</sub>, Diener) by mechanical exfoliation, See Sec 3.2. To ensure the intercalation of water between the substrate and the polymer, especially if the graphene flakes were prepared more than a few hours before being wedged, we usually remove junk graphite with a cotton swab impregnated with ethanol from the substrate. Only the region of interest is left untouched and is further covered with a small drop of the polymer ( $\sim 2 \mu\text{L}$ ). This now acts as a protection mask once the wafer is exposed to air plasma (5 s, SPI Plasma Prep II). The protective mask is then dissolved in the polymer solution (30 dips are enough to solubilize the mask) and the procedure above (e.g., preparation for the wedging transfer) is performed.

### 4.7.3 Nanofabrication of the gold WEDGING patterns and microelectrodes

A  $60 \times 60 \mu\text{m}^2$  field with many copies of the word WEDGING (letter line width is 70 nm) is written by electron-beam lithography in a 495K/950K double spun PMMA layer. A 20 nm gold layer is evaporated. Subsequently, the PMMA/Au layer is gently lifted-off in acetone. Prior to dipping the wafer in the cellulose acetate butyrate solution<sup>5</sup>, the wafer was plasma oxidized under an O<sub>2</sub> plasma for thirty seconds<sup>6</sup>. The patterns are then wedged onto 10  $\mu\text{m}$  polystyrene microspheres<sup>7</sup> previously adsorbed from solution on a Si/SiO<sub>2</sub> substrate. The SEM image is taken with a FEI XL30S microscope operating at 30 kV. The same method was used to fabricate the gold microelectrodes.

---

<sup>5</sup>Supplemented with 0.1 vol% of 1-dodecanethiol.

<sup>6</sup>SPI plasma cleaner.

<sup>7</sup>Polybead Polystyrene, Cat# 17136, lot #597574, Polysciences, Inc.



---

## CHAPTER 5

---

# Formation and control of wrinkles in graphene by the wedging transfer method

V. E. Calado, G. F. Schneider, A. M. M. G. Teulings, C. Dekker and  
L. M. K. Vandersypen

We study the formation of wrinkles in graphene upon wet transfer onto a hydrophilic target substrate, whereby draining of water appears to play an important role. We are able to control the orientation of the wrinkles by tuning the surface morphology. Wrinkles are absent in flakes transferred to strongly hydrophobic substrates, a further indication of the role of the interaction of water with the substrate in wrinkle formation. The electrical and structural integrity of the graphene is not affected by the wrinkles, as inferred from Raman measurements and electrical conductivity measurements.

### 5.1 Introduction

Although graphene is a 2D crystal, it is so far only found on a substrate, as a membrane with a supporting construction [137] or grown at the surface of SiC [142]. Therefore it is considered to be a quasi 2D crystal. Quasi-2D graphene is in general not flat, but has a tendency to form corrugations, including ripples, wrinkles and bubbles [137, 143]. The curvature associated with such corrugations is predicted to alter graphene's electronic and structural properties [144, 145]. Corrugations are often regarded as undesirable, but they can be exploited for inducing pseudo-magnetic fields [146], creating chemically reactive sites [147], and for specific device applications such as optical lenses [148]. Numerical simulations have been done to understand the formation of wrinkles and their impact on graphene [149–152].

Wrinkles are commonly found in chemical-vapor-deposition (CVD) grown graphene that is transferred to other substrates [153–156]. In CVD graphene wrinkles are formed at metal step edges due to thermal stress. The morphology of the metal growth surface can still be seen after transfer. In many cases additional wrinkles, ripples, and bubbles are formed upon transfer. Exfoliated graphene mostly conforms to the corrugations

---

This chapter is based on the paper titled ‘Formation and control of wrinkles in graphene by the wedging transfer method’ *Applied Physics Letters* **101**, 103116 (2012).



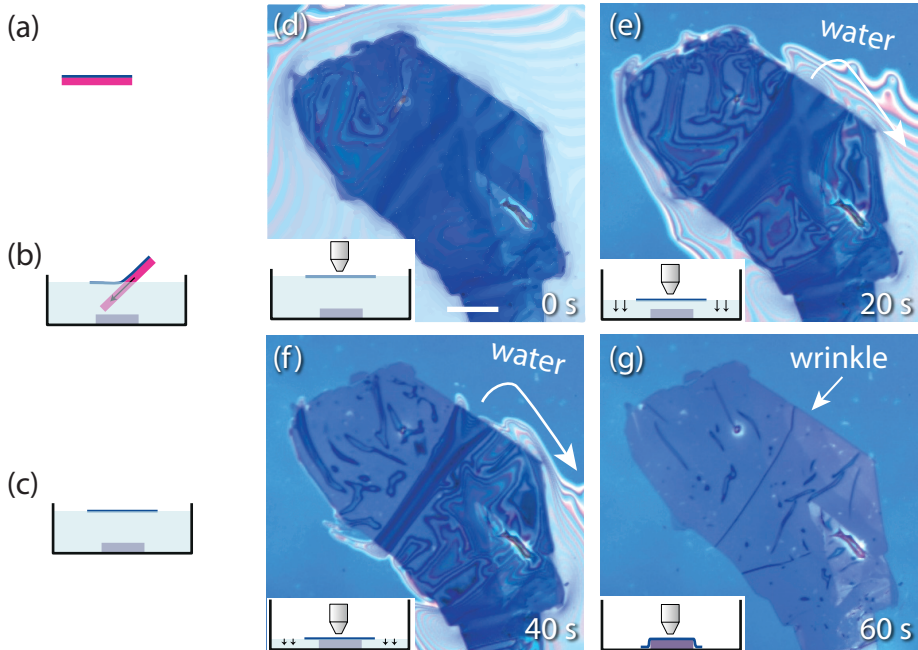


**Figure 5.1:** (a) a  $\text{SiO}_2$  substrate with graphitic flakes covered with a polymer (cellulose acetate butyrate (CAB)). (b-c) The polymer film is “wedged off” the substrate and floats on water. (d-f) Film-strip of a wet transfer process seen through an optical microscope (the time stamps are approximate). The arrow points at a large corrugation that is already present when the flake is floating on water. Once water is drained, the corrugation is left behind as a wrinkle. The scale-bar is  $50 \mu\text{m}$ . The schematics in the insets show the water level.

of the underlying substrate [157], although small additional wrinkles can be observed in a scanning tunnelling microscope [158].

In this chapter we study the formation of wrinkles in graphene during the so-called wedging transfer process, a water-based transfer process (Ch. 4). We give insight in the driving forces for wrinkle formation and suggest different routes to control the wrinkle orientation and abundance, or to eliminate wrinkles altogether. We also examine to what extent the electronic and structural integrity of graphene is preserved upon wrinkle formation.

## 5.2 Wrinkle formation

The wrinkle formation can be already seen with an optical microscope, as illustrated for a graphitic flake in Fig. 5.1 (the entire process is carried out under ambient conditions). Graphitic flakes of varying thicknesses are prepared by mechanical exfoliation, see Sec 3.2. A hydrophobic polymer film covers the substrate (Fig. 5.1a), and is “wedged off” the substrate by intercalation of water (Fig. 5.1b), along with the graphitic flakes. As a result, the film with the flakes is floating on top of the water surface (Fig. 5.1c). Then the water is gradually drained, which brings the polymer

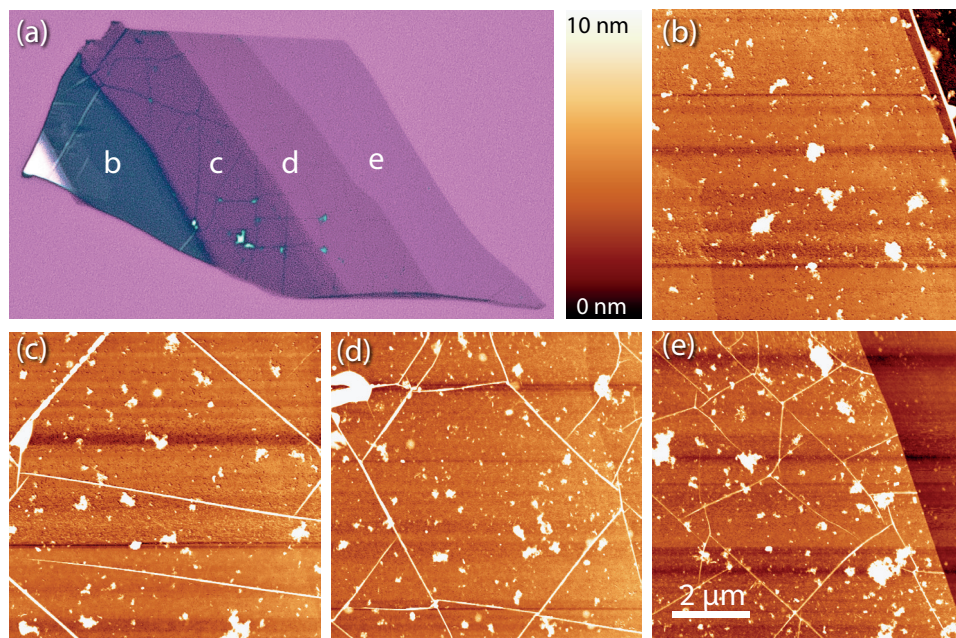


**Figure 5.2:** (a) An optical microscope image of a wrinkled graphite flake of different thicknesses (down to  $\sim 3$  nm thickness). (b-e) Atomic force microscope (AFM) image of the different parts as indicated in (a).

film closer to the target substrate underneath (Fig. 5.1d-e). Here the target substrate is just another Si/SiO<sub>2</sub> substrate, but the transfer can be done onto arbitrary structures [159]. As water is drained further the polymer film comes in contact with the target substrate and pre-existing wrinkles will act as channels that drain water (Fig. 5.1f). Finally, the water is drained away completely and the channels are left behind as wrinkles (Fig. 5.1g).

As the thickness of a graphitic sheet is reduced, the wrinkles increase in density and decrease in height (Fig. 5.2). This can be expected given the lower stiffness of thinner sheets. Fig. 5.2a shows a graphitic flake with pieces of different optical contrast, corresponding to different sheet thicknesses (the lower the contrast, the thinner the flake). Fig. 5.2b-e show atomic force microscopy (AFM) images taken on the respective parts of the flake, as indicated. The mean wrinkle height is (c)  $12 \pm 7.9$  nm, (d)  $7.6 \pm 3.4$  nm and (e)  $4.4 \pm 1.5$  nm, respectively, see Sec. 5.6.

The highest density and lowest height of the wrinkles is obtained for single-layer graphene (SLG). Fig. 5.3 shows an AFM image of a SLG flake (a) before and (b) after transfer, showing no wrinkles before transfer and a large wrinkle density afterwards.

The Raman spectrum of this SLG flake taken after transfer (Fig. 5.3c, wrinkled) is very similar to that taken before transfer (pristine). It is characteristic of single layer graphene [103], and there is no detectable defect-related D band near  $\sim 1350$  cm<sup>-1</sup>. There is no evidence for degradation of the structural integrity of SLG upon wedging transfer.

### 5.3 Transport measurements

Next we perform electrical transport measurements in order to estimate the charge-carrier mobility and the mean-free path. We contact several wrinkled SLG flakes with 10/60 nm Cr/Au electrodes using e-beam lithography. A typical device is shown in the inset of Fig. 5.3d. In a four-point field effect transistor (FET) geometry we measure the resistance as a function of applied back-gate voltage, Fig. 5.3d. The measurement is done in high vacuum ( $\sim 10^{-5}$  mbar) at room temperature. The flake geometries are irregular. For estimating the conductivity from the conductance we choose an aspect ratio such that the mobility values obtained are an underestimate. The charge-carrier density is calculated by applying the parallel plate capacitor model, taking the usual conversion factor for 285 nm SiO<sub>2</sub> of  $7.56 \cdot 10^{10}$  cm<sup>2</sup> V<sup>-1</sup>, see Eq. 2.16 in Sec. 2.3. From the slope in Fig. 5.3d we calculate a hole mobility of 3800 cm<sup>2</sup> V<sup>-1</sup>s<sup>-1</sup> and an electron mobility of 4400 cm<sup>2</sup> V<sup>-1</sup> s<sup>-1</sup>. These are typical values found for SLG on SiO<sub>2</sub>. We have no indication that the wrinkles limit the mobility. This is not surprising given that the mean free path is around  $\sim 20$  nm and the wrinkle-to-wrinkle distance is  $\sim 1\mu\text{m}$ . The mobility is thus limited by other sources.

Fig. 5.4a shows an AFM height profile of a typical wrinkle. The mean height along the wrinkle is  $H = 3.3 \pm 0.4$  nm with a mean full width at half maximum (FWHM) of  $W < 6.8 \pm 2.2$  nm (due to the width of the AFM tip, the width measurement is an upper bound). These dimensions are well in the regime of  $H^2/Wa > 1$  ( $a = 0.24$  nm is the graphene lattice constant), where the pseudo-magnetic field from the corrugations is predicted to be large enough to induce a zero-energy Landau level [160].

### 5.4 Wrinkle orientation and density

In Fig. 5.4b we demonstrate that using the morphology of the substrate we are able to control the orientation of the wrinkles to a certain degree. We have fabricated 1  $\mu\text{m}$  spaced metal strips of 200 nm wide and 55 nm high. SLG is transferred onto these periodic structures, and is partially suspended between the top edge of the step edges and the substrate, as can be seen in Fig. 5.4b. It shows that there is room for water to evacuate near the steps. Wrinkles form in the direction perpendicular to the steps (Fig. 5.4c), presumably so that water can be evacuated towards the steps, and outwards from there. In this way we demonstrate the possibility to align nm sized wrinkles in graphene. We propose that milling small trenches ( $< 50$  nm width) in a substrate would yield a similar result, if graphene can freely suspend over these trenches. This could be used to study electronic transport across multiple aligned wrinkles.

The density of wrinkles in graphene may also be controlled by using other polymers for the transfer or by performing the transfer at different temperatures, see Sec. 5.6. We speculate that the wrinkle density and height depend not only on the polymer viscoelastic properties, but also on the polymer film thickness and the polymer concentration in the solution the substrate is dipped in to cover it with the polymer.

Finally, we show that wrinkle formation can be prevented altogether by transferring flakes onto hydrophobic substrates, as shown in Fig. 5.4d for a SLG flake. To render the surface hydrophobic, it was functionalized with a fluoroalkane molecule

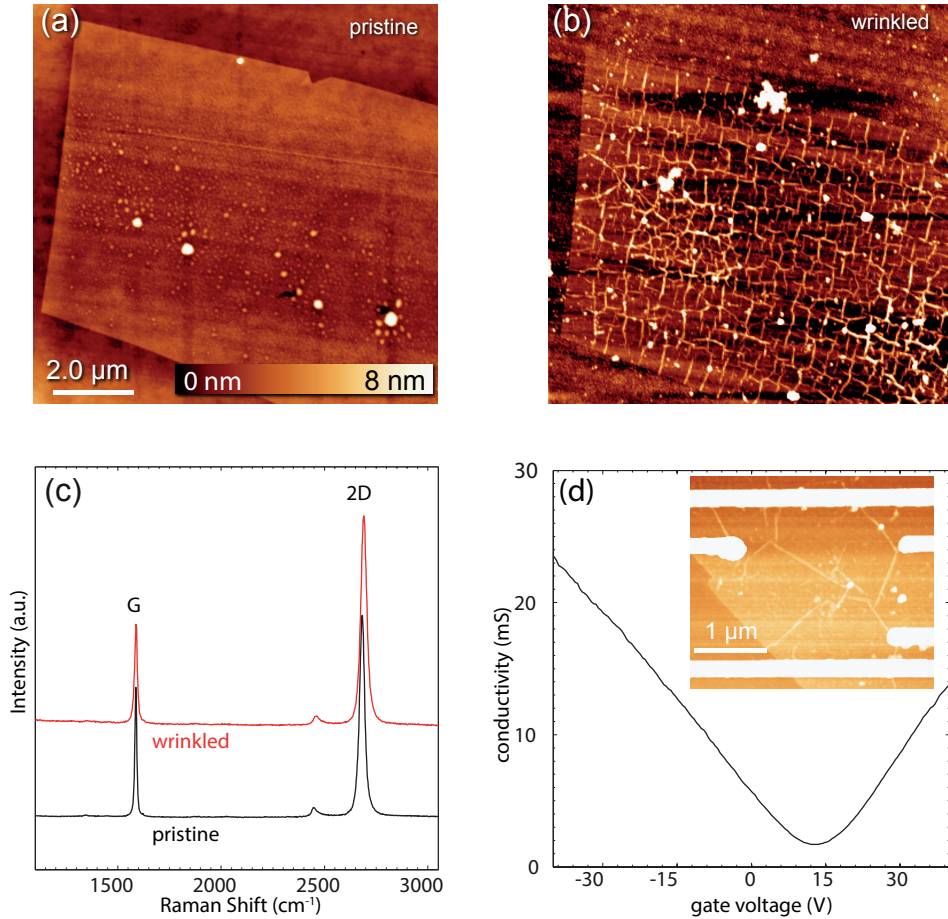


**Figure 5.3:** (a) AFM image of a pristine SLG sheet as prepared by exfoliation. (b) An AFM image of the SLG sheet after transfer, now containing many wrinkles. (c) The Raman spectra for the pristine and wrinkled graphene layer of (a,b). (taken on a Renishaw Raman system 2000 with a 514 nm argon laser, 1 μm spot size, 1 mW power and spectral resolution of  $\sim 3 \text{ cm}^{-1}$ ). (d) Conductivity as a function of applied back-gate voltage, measured at room temperature and at low pressure ( $\sim 10^{-5}$  mbar). Inset: AFM image of the device.

( $\text{CF}_3(\text{CF}_2)_8(\text{CH}_2)_2\text{SiCl}_3$ ). This observation supports the hypothesis that water plays a key role in wrinkle formation during wedging transfer.

## 5.5 Conclusion

In summary, we find that wet transfer of graphene onto commonly used hydrophilic substrates induces wrinkles in graphene. Raman measurements show no detectable defect-related D-peak in this wrinkled graphene, and transport measurements show mobilities comparable to those found before transfer. It is possible to control to a certain extent the density and orientation of the wrinkles. This could be useful for studying electronic transport across a controlled number of (aligned) wrinkles. It also opens up the possibility to explore a number of other experiments. In the presence of a magnetic field, the angle between field and flake will vary on a nm length scale. In addition, the curvature of the wrinkles are such strong that it exhibits local pseudo-magnetic fields according to predictions [146, 160]. The curvature also increases chemical reactivity which can be exploited to chemically bind atoms or molecules [64, 147, 161] in one-dimensional patterns along the wrinkles.

## 5.6 Supplementary

The wrinkle height is dependent on the graphite thickness. Fig. 5.5a shows the atomic force microscope (AFM) image of Fig. 5.6c where the height is calculated by taking a trace across each wrinkle. This is also done for the wrinkles in Fig. 5.6d and e. The mean height is plotted in Fig. 5.5b as function of the optical contrast.

The wrinkle density depends on the polymer used during transfer. Using polystyrene (Fig. 5.6b) rather than cellulose acetate butyrate (CAB) (Fig. 5.6a), the wrinkle density is somewhat lower, as can be expected given that polystyrene is stiffer than CAB. Also the temperature plays a role. Heating the water to 90 °C during the transfer decreases the wrinkle density, as is seen by comparing Fig. 5.6c and 5.6(d). Here we have used a 1:1 mixture of CAB and polystyrene in water.

## Acknowledgments

We thank Bart van der Linden for assistance with the Raman measurements, and Andrea Ferrari, Amelia Barrero, Xing Lan Liu and Stijn Goossens for useful discussions. This work is part of the research program of the Foundation for Fundamental Research on Matter (FOM), which is part of the Netherlands Organization for Scientific Research (NWO).



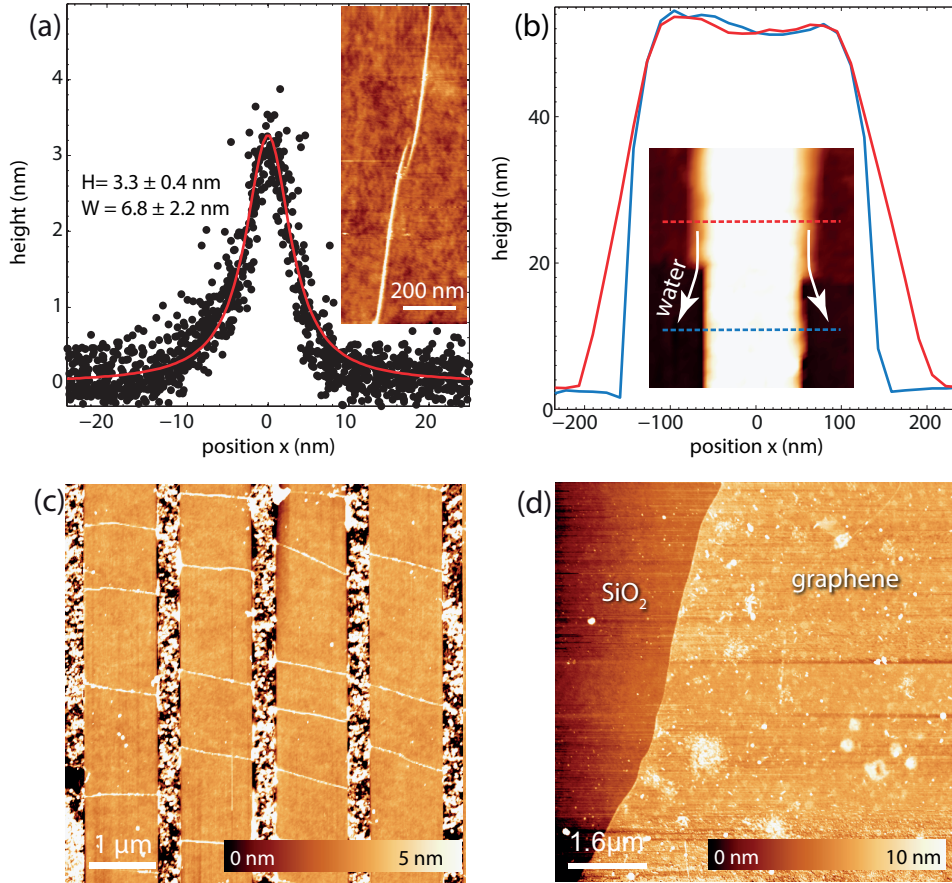


**Figure 5.4:** (a) The height profile of a typical wrinkle. The black dots are a subset of data taken from the inset and plotted together on the same horizontal axis. The red curve is a fit, which is the result of an average over 294 traces. Inset: AFM image of a single wrinkle. The middle part is excluded in the fit. (b) The cross-section height profile across a bare metal strip on the substrate (blue) and across a strip covered with graphene (red), as indicated in the AFM image in the inset. (c) AFM image of SLG transferred onto a periodic step structure. The wrinkles tend to align perpendicularly to the steps. (d) AFM image of SLG transferred to a hydrophobic substrate.

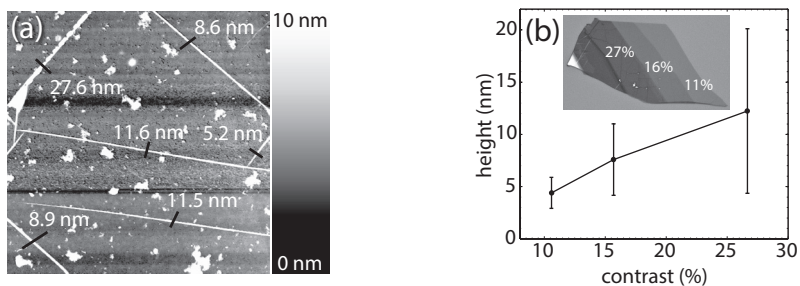


**Figure 5.5:** (a) The atomic force microscope (AFM) image from Fig. 5.6c, where the black lines indicate the traces taken to calculate the height of the wrinkle. (b) The mean height of the wrinkle plotted as function of the graphite layer contrast (error bars indicate  $\pm$  one standard deviation). The layer contrast is calculated by the grey tones relative to the background in the optical image shown in the inset.

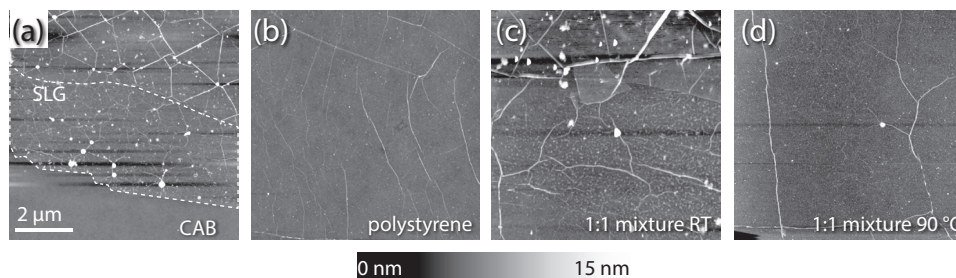


**Figure 5.6:** (a) AFM image of a single layer graphene flake (within the dotted lines) transferred with cellulose acetate butyrate (CAB) as described in the main text. (b) An AFM image of a single layer graphene transferred with polystyrene. (c) An AFM image of a single layer graphene transferred with a 1:1 mixture of polystyrene and CAB at room temperature and (d) at 90 °C

---

## CHAPTER 6

---

# DNA Translocation through Graphene Nanopores

G. F. Schneider, S. W. Kowalczyk, V. E. Calado, G. Pandraud,  
H. Zandbergen, L. M. K. Vandersypen and C. Dekker

Nanopores, nanosized holes that can transport ions and molecules, are very promising devices for genomic screening, in particular DNA sequencing. Solid-state nanopores currently suffer from the drawback that the channel constituting the pore is long,  $\sim 100$  times the distance between two bases in a DNA molecule (0.5 nm for single-stranded DNA). This paper provides a proof of concept for ultrathin nanopores fabricated in graphene monolayers, which is used for single-molecule DNA translocation. The pores are obtained by placing a graphene flake over a micron sized hole in a silicon nitride membrane and drilling a nanosize hole in graphene using an electron beam. As individual DNA molecules translocate through the pore, characteristic temporary conductance changes are observed in the ionic current through the nanopore, setting the stage for future single-molecule genomic screening devices.

## 6.1 Introduction

In the past few years, nanopores have emerged as a new powerful tool to interrogate single molecules [162–164]. They have been successfully used to rapidly characterize biopolymers like DNA [165, 166], RNA [167], as well as DNA-ligand complexes [168] and local protein structures along DNA [169] at the single-molecule level.

A key driving force for nanopore research in the past decade has been the prospect of DNA sequencing. However, a major roadblock for approaching high-resolution DNA sequencing with pores is the finite length of the channel constituting the pore. In a typical solid-state nanopore in say a 30 nm thick membrane, the current blockade resulting from DNA translocation is due to a large number of bases ( $\sim 100$ ) present in the pore, Fig. 6.1a. Here, we demonstrate that this limitation can be overcome by realizing an ultimately thin nanopore device in a graphene monolayer, Fig. 6.1b.

---

This chapter is based on the paper titled ‘DNA Translocation through Graphene Nanopores’ *Nano Letters* **10**, 3163–3167 (2010)



Furthermore, we show the translocation of individual DNA molecules through such graphene nanopores.

Fabrication of nanopores in graphene layers was reported previously in the vacuum of a transition electron microscope (TEM) [140, 170], but graphene nanopore devices that ionically probe the translocation of single molecules were so far not realized.

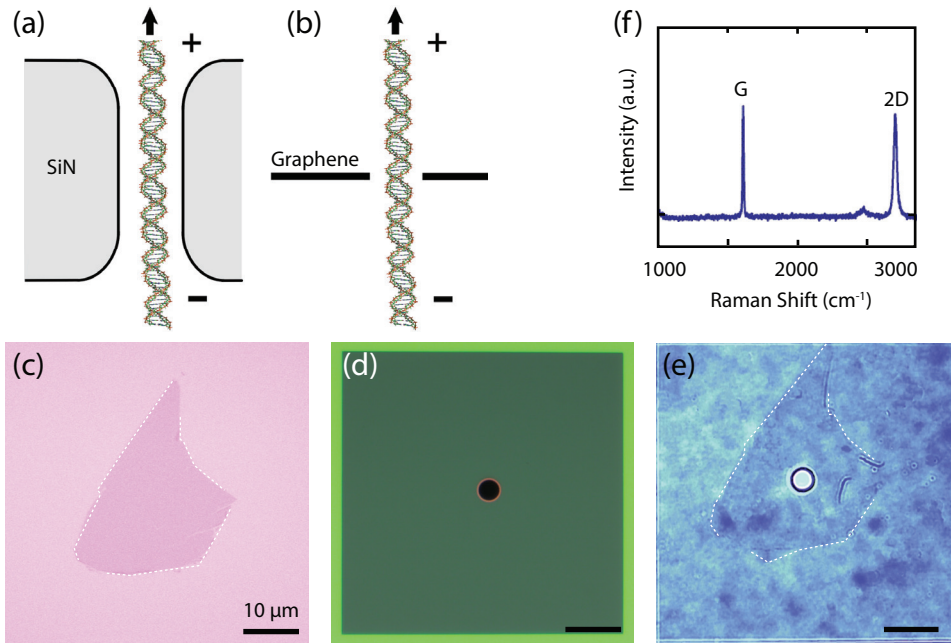


**Figure 6.1:** Graphene nanopores for DNA translocation (a) Side-view illustration comparing DNA translocation through a SiN solid-state nanopore with that through a free-standing one-atom thick graphene nanopore (b). (c) Optical microscope images depicting the transfer of graphene from Si/SiO<sub>2</sub> (c) onto a microfabricated silicon nitride chip containing a 5  $\mu\text{m}$  hole (d). (e) After the transfer by wedging, the flake entirely covers the hole. (f) Raman spectrum of the flake on Si/SiO<sub>2</sub> before the transfer.

Graphene is a two-dimensional layer of carbon atoms packed into a honeycomb lattice with a thickness of only one atomic layer ( $\sim 0.3$  nm) [1]. Despite its minimal thickness, graphene is robust as a free-standing membrane [137, 171]. In addition, graphene is a very good electrical conductor [172]. Graphene therefore opens up new opportunities for nanopores such as new analytical platforms to detect, for example, local protein structures on biopolymers or sequencing with single-base resolution. Indeed, theoretical calculations of DNA translocation through a nanopore in graphene have already indicated the possibility for single-base resolution by probing the translocating molecule electrically in the transverse direction by use of the intrinsic conductive properties of graphene [173].

We obtain graphene by the mechanical exfoliation method, see Sec. 3.2. The advantage here of exfoliated graphene to CVD graphene is that it allows to select sheets with a range of thicknesses (i.e., number of layers). An example of a monolayer graphene is shown in Fig. 6.1c, with its corresponding Raman spectrum in

Fig. 6.1f. This flake is transferred onto a SiN support membrane with a  $5\ \mu\text{m}$  sized hole (Fig. 6.1d) by use of the wedging transfer method (Ch. 4). The result is a suspended graphene flake on a  $5\ \mu\text{m}$  hole, Fig. 6.1e.

## 6.2 Graphene nanopore

We drill a nanopore in the suspended graphene monolayer using a highly focused electron beam of a transmission electron microscope (TEM). The acceleration voltage is 300 kV, well above the 80-140 kV knockout voltage for carbon atoms in graphene [174] (see Sec. 6.6). Drilling the holes by TEM is a robust well-reproducible procedure (we drilled 39 holes with diameters ranging from 2 to 40 nm, in monolayer as well as in multilayer graphene; some examples of pores are shown in Fig. 6.2).

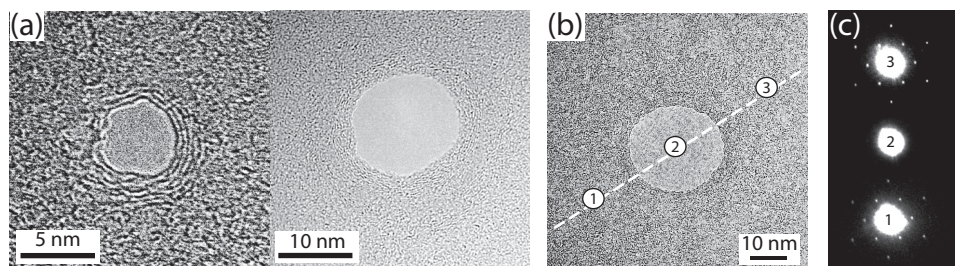


**Figure 6.2:** Drilling of graphene nanopores. (a) Transmission electron microscopy (TEM) of some nanopores drilled into multilayer graphene (b) TEM image (top) and diffraction patterns (bottom) across a 25 nm diameter pore in a monolayer of graphene. Numbers of the diffraction images indicate the spots where the patterns were recorded. (c) Diffraction patterns measured across the monolayer nanopore of panel (b). The diffraction pattern was measured at three spots indicated in panel (b) with a 3 nm electron beam. The hexagonal lattice of diffraction spots is highlighted by the solid lines for clarity.

Because of the high acceleration voltage of the electron beam, drilling could potentially induce damage to the graphene around the pore. However, electron beam diffraction measurements across the hole (Fig. 6.2b and 6.2c) confirm the crystallinity of the monolayer surrounding the hole, as evidenced by the well-defined hexagonal diffraction patterns (Fig. 6.2c).

## 6.3 Measurement setup

We mount the pore into a microfluidic flow cell, add a 1 M saline solution<sup>1</sup> on both sides of the graphene membrane, and measure current-voltage (I-V) curves from ion transport through the graphene nanopore (inset of Fig. 6.3). The resistance value ( $5.1\ \text{M}\Omega$  in the example of the inset of Fig. 6.3) and the linearity of the I-V curve indicate that the current is consistent with ion flow through the pore and does not arise from electrochemical processes at the conductive graphene surface [175]. Furthermore, samples with a graphene layer but without a nanopore exhibit a very high

<sup>1</sup>1 M KCl, room temperature (TE), pH 8.0

ionic resistance ( $> 10 \text{ G}\Omega$ ), which indicates that the graphene flake adheres well to the SiN surface and forms an insulating seal.

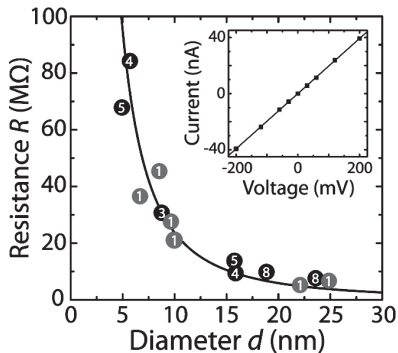


**Figure 6.3:** Nanopore resistances. Measured values of pore resistance versus diameter for a number of graphene nanopores ( $n=13$ ). For each pore, the number of graphene layers is indicated by the number within the circle: 1 denotes graphene monolayers (gray);  $x$  denotes  $x$  layers of graphene (black). The solid line denotes a  $1/d^2$  dependence. The inset shows an I-V curve of a 22 nm nanopore in a graphene monolayer recorded in 1M KCl. A linear resistance of 5.1  $\text{M}\Omega$  is observed.

We measured I-V curves for a number of pores ranging from 5 to 25 nm in diameter, in six monolayer graphene devices and seven multilayer graphene devices. Sample thickness is determined based on transmitted light intensity (2.3% reduction per layer) [6]. Fig. 6.3 shows the obtained resistances versus pore diameter, for both monolayers and multilayers up to eight layers (with a total layer thickness between 0.3 and 2.7 nm). We do not observe a strong dependence on the number of layers constituting the nanopore membrane. The thickness  $L$  can be determined by fitting the pore resistance  $R$  scales with the pore diameter  $d$ , by the following equation [176]:

$$R = \rho_0 \left( \frac{1}{d} + \frac{4L}{\pi d^2} \right) \quad (6.1)$$

From this equation we found<sup>2</sup> that  $L = 14 \text{ nm}$ . This is much thicker than the graphene, which can be attributed to the pre-coating of the pore with a self assembled monolayer to reduce DNA sticking<sup>3</sup>.

## 6.4 DNA translocations

Double-stranded DNA (dsDNA) can be driven electrophoretically through the nanopore and detected by monitoring the ion current. Upon addition of the  $\lambda$ -dsDNA (16  $\mu\text{m}$  long) on one side of the pore and applying a voltage of 200 mV across the graphene membrane, a series of spikes is observed in the conductance traces (Fig. 6.4a).

<sup>2</sup>We have used the fitting parameters from the supporting information of Ref. [177]

<sup>3</sup>See Ref. [178] for a discussion about this.

Each temporary drop in the measured conductance,  $\Delta G$ , arises from a single DNA molecule that translocates through the pore. As for conventional SiN nanopores [179], three characteristic signals are observed, corresponding to three types of translocation events: nonfolded<sup>4</sup>, partially folded<sup>5</sup>, or fully folded molecules<sup>6</sup> [166]. Example events are shown in Fig. 6.4b. The events are color coded in black (nonfolded), red (partially folded), and blue (fully folded). From a large number ( $n = 1222$ ) of such events, we obtain a histogram of conductance blockade levels  $\Delta G$ , as presented in Fig. 6.4c. Three peaks are visible, the first being the open-pore current at 0 nS (i.e., the baseline); the peak at  $\sim 1.5$  nS which corresponds to one strand of DNA in the pore; and the peak at  $\sim 3$  nS due to two strands of the same DNA molecule in the pore. We measured DNA translocations on seven graphene nanopores<sup>7</sup> and collected good statistics on three devices<sup>8</sup>.

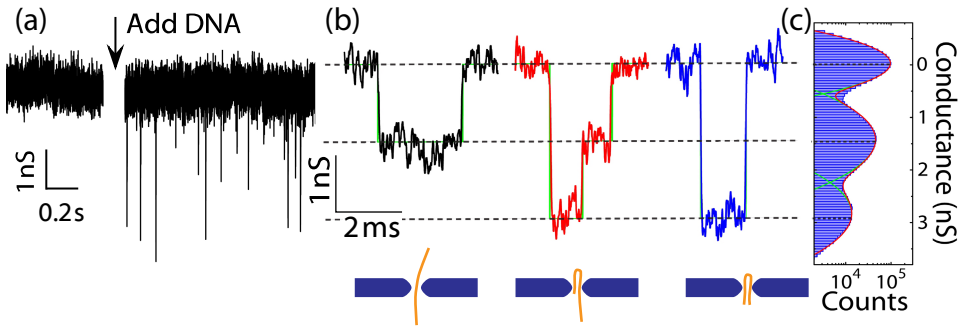


**Figure 6.4:** DNA translocation through a graphene monolayer. (a) Translocation of 48 kbp double-stranded  $\lambda$ -DNA across a 22 nm nanopore within a graphene monolayer, showing the baseline conductance (left) and blockade events upon addition of DNA (right). (b) Examples of translocation events of nonfolded (black), partially folded (red) and fully folded (blue) DNA molecules recorded at 200 mV. (c) Conductance histogram of 1222 translocation events, including 1 ms of open-pore conductance before and after the event. Note that counts in this histogram correspond to a single current measurement, not to a single event.

A scatter plot of  $\Delta G$  versus the time duration of the events is shown in Fig. 6.5, with the same color coding as used in Fig. 6.4b. Each dot in this diagram represents a single DNA translocation event. The blockade amplitude  $\Delta G = 1.5 \pm 0.4$  nS for nonfolded DNA in these graphene pores is quite similar in magnitude to that measured for pores of similar sizes in a 20 nm thick SiN membrane ( $1.4 \pm 0.3$  nS) for the same conditions. This is unexpected as we would expect the ionic current blocked by a DNA molecule to scale as the inverse of the thickness of the nanopore membrane [174], leading to higher blockade amplitudes for DNA in graphene pores.

In addition to the event amplitude, we studied the translocation times of the events.

<sup>4</sup>Nonfolded is when the molecule translocates in a linear head-to-tail fashion.

<sup>5</sup>Partially folded is when the molecule is randomly grabbed from the side of the DNA coil, and first translocates in a singly folded fashion.

<sup>6</sup>Fully folded molecules is when the DNA happens to be grabbed in the middle of the molecule.

<sup>7</sup>Monolayer and multilayer graphene membranes with pore diameters ranging from 10 to 25 nm.

<sup>8</sup>Two monolayers and an eight-layer multilayer with pore diameters of 22, 25, and 24 nm, respectively.

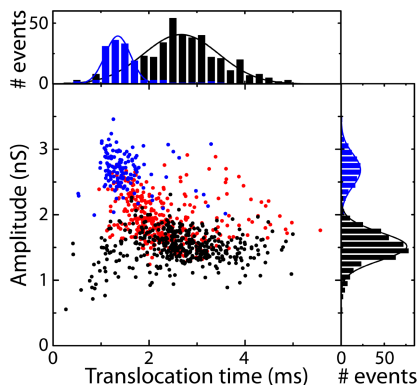


**Figure 6.5:** Event analysis. Scatter diagram of the amplitude of the conductance blockade versus translocation time with the accompanying histograms for the nonfolded and fully folded data at the top and the right. Color coding as in Fig. 6.4b. Each point in this scatter diagram corresponds to a single translocation event. For the labelling of events, each conductance data point within a translocation event (defined as an excursion of more than 6 times the standard deviation of the open-pore rms noise) is attributed to one of the peaks in the conductance histogram shown in Fig. 6.4c. The minimum required subsequent duration at one level is set to 100  $\mu$ s, given by the rise-time resulting from the 10 kHz low-pass filtering.

The average translocation time is  $2.7 \pm 0.8$  ms for the nonfolded DNA (Fig. 6.5), a value that is similar, albeit slightly larger, to that for solid-state nanopores in a 20 nm SiN membrane for which the translocation time is  $1.2 \pm 0.3$  ms under the same applied voltage of 200 mV and for a similar pore diameter. A slightly larger translocation time compared to SiN pores was also observed for our other monolayer device for which we also got good statistics. We note that the translocation time is expected to be independent of the membrane thickness because the driving electrostatic force is the same: in a thinner membrane, the electric field over the graphene pore is higher (same voltage applied over a shorter distance) which however is exactly compensated by the smaller number of charges present on the piece of the DNA molecule that resides in the pore [180]. This is only a crude scaling argument however, and there can be various reasons why the translocation time is somewhat different for ultrathin nanopores. At a practical level, a slower translocation will be helpful for analytical applications where maximizing spatial resolution is needed.

## 6.5 Conclusion

The establishment of double-stranded DNA translocation through single-layer graphene nanopores represents an important first step toward pushing the spatial-resolution limits of single-molecule nanopore analytics to subnanometer accuracy. Future research will be aimed at exploring single-strand DNA translocation, single-base detection, and ultimately sequencing.

## 6.6 Methods

### 6.6.1 Graphene sample fabrication

Graphene flakes were prepared by the mechanical exfoliation method on 90 nm Si/SiO<sub>2</sub>, see Sec 3.2. The Si/SiO<sub>2</sub> wafers were plasma-oxidized (O<sub>2</sub>, Diener) just before graphene preparation.

Graphene flakes were transferred onto microfabricated Si/SiO<sub>2</sub>/SiN chips described before using the wedging transfer method, Chapter 4.

Contrary to the design described by Ref. [181], prior the transfer of graphene, we etched the 20 nm thin SiN membrane using hot phosphoric acid (200 °C) for 45 min.

### 6.6.2 Fabrication of Nanopores in Graphene

Nanopores were fabricated and imaged using a Cs-corrected Titan Cubed Super-twin/STEM FP5600/40 microscope operated at an accelerating voltage of 300 kV. An electron beam with a diameter of 15 nm at full width at half-maximum height and a beam density of 106 electrons/(snm<sup>2</sup>) was used for drilling. Gatan 2k × 2k CCD with binning 1 was used for image recording. Diffraction patterns were acquired with a beam size of 3 nm and a beam density of 105 electrons/(s nm<sup>2</sup>). To remove contamination, samples were heated at 200 °C for at least 20 min prior to their insertion in the vacuum chamber of the microscope. After being drilled, samples were stored in ethanol.

### 6.6.3 Nanopore Experiments

For the electrical measurements, a membrane with a single graphene nanopore is mounted in a polyether ether ketone (PEEK) microfluidic flow cell and sealed to liquid compartments on either side of the sample. Measurements are performed in 1 M KCl salt solution containing 10mM Tris-HCl and 1mM EDTA at pH 8.0 at room temperature (or TE, as abbreviated in the manuscript). Ag/AgCl electrodes are used to detect ionic currents and to apply electric fields. Current traces are measured at 100 kHz bandwidth using a resistive feedback amplifier<sup>9</sup> and digitized at 500 kHz. Before dsDNA was injected, the graphene-SiN microchip was flushed with a 1 mg/mL solution of 16- mercaptohexadecanoic acid in 8:2 toluene/ethanol and additionally rinsed in respectively clean 8:2 toluene/ethanol and ethanol. This is expected to form a flat self-assembled monolayer on the graphene surface which demotes DNA adhesion [182]. dsDNA was unmethylated  $\lambda$ -DNA<sup>10</sup>. The event-fitting algorithm used to analyze and label the translocation events was the same as the one described before [166]. Only events exceeding six times the standard deviation of the open-pore root-mean-square noise are considered. Due to possible baseline fluctuations, we only considered events whose current before and after the event does not change more than 10% of the event amplitude. We additionally filtered the data at 10 kHz for better signal-to-noise ratio, and we discarded events shorter than 200  $\mu$ s.

<sup>9</sup>Axopatch 200B, Axon Instruments

<sup>10</sup>20 ng/  $\mu$ L, reference no. D152A, lot no. 27420803, Promega, Madison, WI.

## **Acknowledgments**

We thank M.-Y. Wu and Q. Xu for their assistance in TEM, H. Postma for discussions, V. Karas and K. van Schie for technical assistance, G. Buchs for the Raman measurements and The Netherlands Organisation for Scientific Research (NWO), the NanoSci- E+ Program, the Foundation for Fundamental Research on Matter (FOM), and the EC project READNA for funding

---

## CHAPTER 7

---

# Zero-bias conductance peak and Josephson effect in graphene-NbTiN junctions

M. Popinciuc\*, V. E. Calado\*, X. L. Liu, A. R. Akhmerov,  
T. M. Klapwijk and L. M. K. Vandersypen

We report electronic transport measurements of graphene contacted by NbTiN electrodes, which at low temperature remain superconducting up to at least 11 Tesla. In devices with a single superconducting contact, we find a more than twofold enhancement of the conductance at zero bias, which we interpret in terms of reflectionless tunneling. In devices with two superconducting contacts, we observe the Josephson effect, bipolar supercurrents and Fraunhofer patterns.

## 7.1 Introduction

There has been a lot of interest in studying quantum transport in graphene (G) contacted by superconductors (S). So far, most experiments have focused on electrical transport in SGS Josephson junctions. Tunable Josephson supercurrents [96], multiple Andreev reflections [183–185], Andreev bound states [186], phase diffusion phenomena [187], macroscopic quantum tunnelling [188], and superconducting phase transitions [189, 190] have been observed in devices employing Al [96, 183, 185, 191–196], W [184], Ta [197], Pb [186, 187, 198], PbIn [188], Sn [189, 190] as superconductors.

An interesting and experimentally yet unexplored direction is to demonstrate specular Andreev reflection [99] by realizing a superconducting gap larger than the potential fluctuations in the graphene. Another interesting possibility is to study the interplay between superconductivity and the quantum Hall effect [199–203] which requires contacting high-mobility graphene with a superconductor with a large critical magnetic field. While we were finalizing the manuscript, measurements on graphene with Nb and ReW contacts at high magnetic field were posted, see Ref. [204].

In this study we report electronic transport through NbTiN based SGN and SGS junctions, where N is a normal, non-superconducting metal electrode. NbTiN has a

---

This chapter is based on the paper titled 'Zero-bias conductance peak and Josephson effect in graphene-NbTiN junctions' *Physical Review B* **85**, 205404 (2012)

\* Contributed equally to this work



large gap, a high critical temperature ( $T_C$ ) and a high upper critical perpendicular magnetic field ( $B_{C_2}^\perp$ ). We present electrical measurements in a field-effect geometry as a function of source-drain bias, temperature (50 mK-5 K) and external magnetic field (0-11 T) applied perpendicular to the sample. In SGN devices at sub-Kelvin temperatures and up to moderate magnetic fields, we observe a zero-bias conductance peak. We analyze this peak in terms of reflectionless tunneling [205–207]. In SGS devices, we observe gate-tunable supercurrents and discuss their magnetic field response, which exhibits characteristic Fraunhofer patterns.

## 7.2 Sample fabrication

Graphene samples were prepared as described in Sec. 3.2 The electrodes were defined by standard electron beam lithography. The normal contacts consist of a 8 nm Ti adhesion layer with a 50 nm AuPd alloy on top. The  $\sim 30$  nm thick NbTiN superconducting contacts were made by DC sputtering of a NbTi target (30% Ti, 70% Nb atomic percentage) in a Ar/N<sub>2</sub> plasma in a Nordiko-2000 system using an unbalanced parallel plate configuration [208]. The Ar and N<sub>2</sub> flows were 100 sccm and 4 sccm and the deposition pressure was about 6 mTorr. The deposition conditions were optimized for producing high quality NbTiN films with low stress [209, 210] and a  $T_C$  of about 13 K corresponding to a BCS superconducting gap of 2 meV. The electrical measurements indicate an upper critical perpendicular magnetic field  $B_{C_2}^\perp$  in excess of 11 T at 50 mK<sup>1</sup>.

We investigated three ways of contacting graphene with NbTiN: (1) direct sputtering of NbTiN on the graphene, (2) sputtering of NbTiN on a Ti protective layer and (3) sputtering of NbTiN on a Ti/Au protective layer. Direct sputtering of NbTiN on graphene leads to very high contact resistances of hundreds of k $\Omega$  and measurements of these devices are not discussed further. This is attributed to damage to the graphene layer underneath the S electrode due to its exposure to the sputtering plasma and/or the highly energetic particles involved in the sputtering process<sup>2</sup>. In order to prevent this problem we fabricated devices in which we protected the graphene by two different approaches. For the type A (Fig. 7.1a) devices, we first covered graphene with a thin layer of Ti (10 nm)<sup>3</sup>. Next, in 3 to 5 minutes the sample was transferred through air into the sputtering system, which unavoidably leads to oxidation of the Ti. Prior to the sputter deposition of NbTiN, the oxidized Ti was cleaned by an Ar RF plasma of 200 W for 5 min in a pressure of 6 mTorr. This cleaning procedure leaves about 7 nm Ti. For the type B devices (Fig. 7.5a) we e-beam evaporated Ti(2 nm)/Au(2.5 nm) as a protective layer. Since no oxide is expected to form during the sample transfer, no RF plasma cleaning was done before depositing NbTiN.

---

<sup>1</sup>The exact value is not known.

<sup>2</sup>DC voltages are of the order of 380 V.

<sup>3</sup>Ti was evaporated in an Eva 450 e-beam evaporator, which involves particles with energies of the order of only 1 eV.

## 7.3 Measurements

The electrical measurements are done as described in Sec. 3.8. All measurements were done in a two-terminal configuration and the data presented here were corrected for the RC filter series resistance of 2.5 k $\Omega$  per filter.

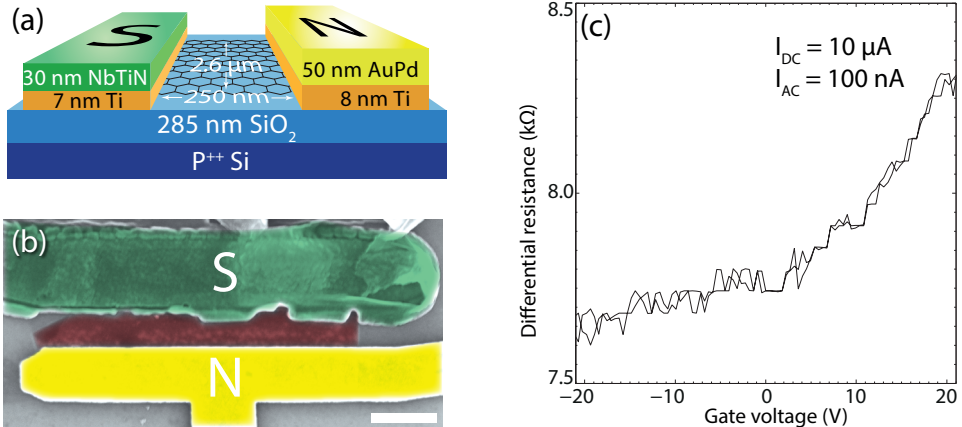


**Figure 7.1:** Type A SGN device with 7 nm Ti. (a) Schematic showing dimensions and electrodes configuration. (b) False color SEM image (the white scale bar represents 500 nm). (c) Differential resistance versus gate voltage at  $I_{DC} = 10 \mu\text{A}$  and  $I_{AC} = 100 \text{nA}$  in two gate sweep directions.

### 7.3.1 SGN junction: type A

In Fig. 7.1a and 7.1(b) we show a schematic and a false-color scanning electron microscope image (SEM) of a type A device. The graphene flake is 2.6  $\mu\text{m}$  wide. The S and N electrodes completely overlap the flake and are separated by about 250 nm (edge to edge). In Fig. 7.2a we present two-terminal differential resistance ( $dV/dI$ ) measurement at 50 mK as a function of the back-gate voltage ( $V_{gate}$ ) for the as-fabricated SGN junction. The measurement was done with an AC current of 100 nA superimposed on a DC current of 10  $\mu\text{A}$ . The differential resistance is rather high over the entire gate voltage range: given the device dimensions, the doping level and an estimated carrier mobility of  $\sim 2000 \text{cm}^2\text{V}^{-1}\text{s}^{-1}$  observed in a nearby device on the same flake, the graphene differential resistance should be well below 1 k $\Omega$ . Other devices made in the same batch show similar or even higher differential resistances, but type A devices with a thicker Ti protective layer (about 20 nm) and type B devices (without RF plasma cleaning) do not. Three-terminal measurements of the S and N contact resistances (to the graphene covered by the contacts) show values of 400  $\Omega$  and 700  $\Omega$ , respectively. Therefore, we conclude that most of the resistance is due to the transition region from the covered graphene to the uncovered graphene (denoted as G'). We believe that stress in the NbTiN films and/or RF plasma cleaning may cause damage to the graphene area around the S contacts.

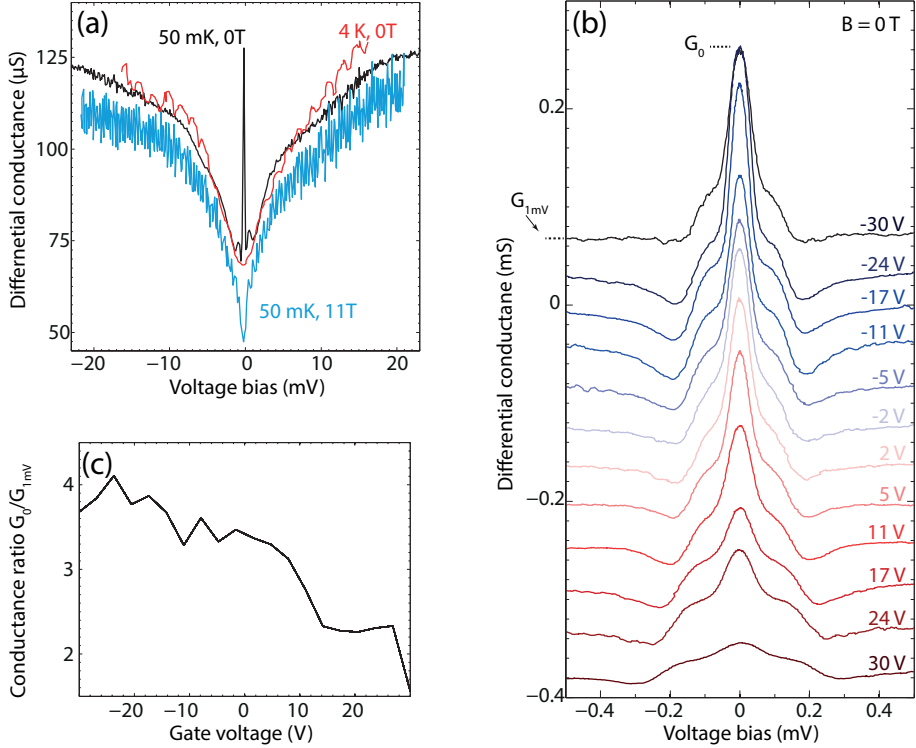
In Fig.7.2(a) we show the differential conductance ( $dI/dV$ ) for  $V_{gate} = 0$  V as a function of voltage bias at 60 mK (for two perpendicular magnetic field values of 0 T and 11 T) and at 4 K for 0 T. We see that the differential conductance ( $dI/dV$ ) is non-constant over the entire bias-voltage range of  $\pm 20$  mV. Since the NbTiN gap is only  $\sim 2$  mV, the non-constant differential conductance above 2 mV cannot be attributed to the superconducting contacts. Indeed, when normalized to a high bias value of 10 – 20 mV, the three differential conductance ( $dI/dV$ ) traces in Fig.7.2(a) fall on top of each other except for a bias range of less than 2 mV. The observed behavior is also incompatible with known mechanisms that lead to a bias-dependent graphene resistance [211–213]. Possibly it is caused by the damaged graphene near the contacts.

Fig. 7.2b shows differential conductance traces at low bias for several gate voltages. We observe a zero bias conductance peak for energies  $E_C$  smaller than 0.1 meV and a conductance dip at energies  $E_D$  of around 0.2 meV. Both features are present at all gate voltages. The zero bias conductance is enhanced by more than a factor of two compared with its value at  $\sim 1$  mV for almost all the gate voltages investigated, see Fig 7.2(c). Ignoring possible magnetic moments [214, 215], to the best of our knowledge only reflectionless tunneling can explain an enhancement a factor of more than two. Hereby the transmission of a tunnel barrier between a superconductor and a normal metal is enhanced due to the diffusive transport in the normal metal [205–207].

Following the semiclassical approach of Ref. [205] we sketch the principle behind reflectionless tunneling in Fig. 7.3. The quasi-particles move from the right normal metal reservoir towards the S electrode through the diffusive graphene. A potential barrier exists at the graphene/S interface, which in our case is assumed to be due to the damaged graphene around the S electrode. An electron ( $e_1$  in Fig. 7.3) that hits the barrier can be either Andreev reflected as a hole ( $h_1$ ) or normal reflected as an electron, continuing along path 2. Due to scattering on impurities the electron moving on path 2 has a chance to hit the barrier once again where it can retroreflect as a hole ( $h_2$ ). Retracing path 2, this second hole reaches the initial point where it can undergo normal reflection. Constructive interference between the first and the second hole increases the total Andreev reflection probability of the incoming electron  $e_1$ . In a diffusive sample there are a multitude of such paths and their respective contributions add up leading to an enhancement of the conductance. At finite bias, the phase of  $h_2$  averages out and the conductance enhancement disappears.

The order of magnitude of the cutoff energy  $E_C$  for which coherence is lost is determined by the phase coherence time  $\tau_\phi$  according to  $E_C \approx \hbar/\tau_\phi$ . Taking  $E_C \approx 0.065$  meV from the differential conductance at  $V_{gate} = 0$  V, we estimate  $\tau_\phi \approx 10$  ps which is comparable with the values obtained in Ref. [83]. The phase breaking length is given by  $L_\phi = \sqrt{D\tau_\phi}$ . Here,  $D$  is the diffusion constant given by  $D = v_F l_{mfp}/2$ , where  $l_{mfp}$  is the mean free path and  $v_F \approx 10^6$  m s $^{-1}$  the Fermi velocity. Taking  $\tau_\phi = 10$  ps and a mean free path of  $\approx 17$  nm (corresponding to a carrier mobility of 1000 cm $^2$ /Vs at 30 V from the Dirac point) gives  $L_\phi \approx 280$  nm, which is comparable to the sample length  $L = 250$  nm.

Now we turn our attention to the magnetic field and the temperature dependence. In Fig. 7.4a we show the differential conductance as a function of bias voltage for various magnetic fields applied perpendicular to the sample surface. A finite magnetic field breaks the time reversal symmetry and introduces a phase difference between the interfering holes. Coherence is lost when the loop formed by path 2 and the



**Figure 7.2:** Measurements of the SGN device shown in Fig. 1. (a) Differential conductance as a function of voltage bias for  $V_{gate} = 0$  V at 4 K ( $B = 0$  T) and 50 mK (for  $B = 0$  T and  $B = 11$  T). (b) Differential conductance vs. bias voltage at various gate voltages indicated by labels ( $T = 50$  mK,  $B = 0$  T). The curves are offset in 40  $\mu\text{S}$  steps; the top curve has no offset. (c) Zero-bias conductance ( $G_0$ ) normalized to the value at 1 mV vs. gate voltage. The zero bias conductance is enhanced by a factor larger than two at almost all gate voltages.

superconductor encloses one flux quantum  $\Phi_0 = h/e$ . Taking  $B = 4$  T as the field where reflectionless tunneling is suppressed (see Fig. 7.4), we estimate an effective area of  $1 \times 10^3$  nm<sup>2</sup>. At high magnetic fields one expects Landau levels to develop as the graphene enters the quantum Hall regime. However since we did not see clear signs of quantum Hall plateaus, it is likely that the disorder in the sample was too high.

In Fig. 7.4b we plotted the temperature dependence of the differential conductance at  $V_{gate} = 0$  V and  $B = 0$  T. The measurements were taken after a mild current annealing step [10] performed at base temperature. For about 10 minutes, we slowly ramped up a DC current applied between the S and N contacts, up to a current density of 4.5 A cm<sup>-1</sup>. While this led to a  $\approx 50\%$  increase in the overall conductance, the zero-bias conductance peak and the broader conductance dip remained at about the same energies. This behavior is similar to what was reported in Ref. [197]. From Fig. 7.4b we observe that the zero-bias peak drops at about 1 K. This thermal energy scale is consistent with  $E_c$  extracted from the width of the peak.

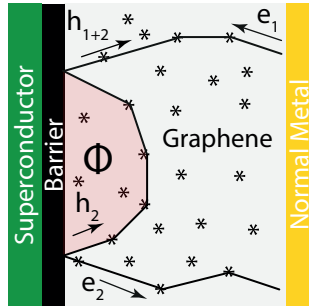


**Figure 7.3:** Illustration of reflectionless tunneling. Quasi-particles move from the right reservoir towards the superconductor through diffusive graphene. A potential barrier exists between graphene and the superconductor. The Andreev reflection probability at an otherwise poorly transparent interface is enhanced due to interference effects (see text for details).

### 7.3.2 SGS junction: type B

Now, we briefly discuss measurements of SGS junctions. In a type A SGS device with similar dimensions as the SGN device discussed earlier and made in the same batch, no supercurrent flowing through graphene (Josephson effect) was observed. We understand this in terms of the poor transparency of the G-G' interfaces which hinder the diffusion of the Cooper pairs into uncovered graphene. In another batch, with a thicker Ti layer (about 20 nm after the RF plasma cleaning), we did observe bipolar supercurrents and Fraunhofer patterns in several graphene junctions for electrode spacings of up to 400 nm [216]. This is indicative of less damage to the G-G' transition region. These data are not discussed further. In Fig. 7.5 we show measurements of a type B device. Given the Ti(2 nm)/Au(2.5 nm) protective layer, no oxide is expected to form during the sample transfer through air and the RF plasma cleaning step before deposition of NbTiN was not necessary. Fig. 7.5a and Fig. 7.5b show the schematic and a false color SEM image of the device. The graphene flake is 1.5  $\mu\text{m}$  wide and the electrode separation is 150 nm (edge to edge). In Fig. 7.5c we show the differential resistance as a function of current bias at  $V_{gate} = 0$  V and  $B = 0$  T. A critical current  $I_C$  of 4 nA is observed. We note that  $I_C$  is relatively small given the junction dimensions and the carrier density. Also, we did not observe supercurrents in type B junctions with 280 nm or larger electrode separations, possibly due to the weakening of the proximity effect in the Ti/Au bilayer. The sharp peaks in the differential resistance we interpret as self-induced Shapiro steps since the energies involved closely match those of standing waves formed in the metal box enclosing the sample, which has a size of 6.0 cm. [217, 218] In Fig. 7.5d we show the differential resistance as a function of the gate voltage and current bias as a 2D color plot. The dark region corresponds to a supercurrent through graphene. The magnitude of the critical current depends on the charge carrier density and decreases when going from metallic conduction towards the charge neutrality point (at  $\sim 22$  V), in agreement with previous reports [96]. In Fig. 7.5e we show the differential resistance as a function of a perpendicular magnetic field and bias current at zero gate voltage. The critical current is modulated by the

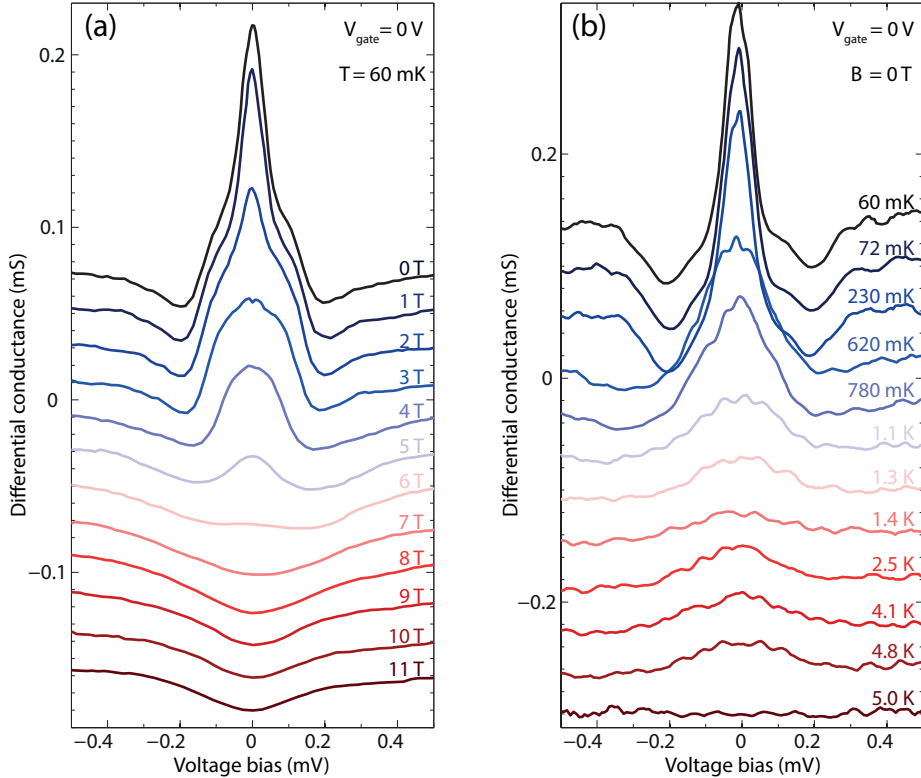


**Figure 7.4:** Measurements of the SGN device shown in Fig. 1. (a) Differential conductance vs. bias voltage at  $V_{gate} = 0$  V for different magnetic fields. (b) Temperature dependence of the differential conductance at  $V_{gate} = 0$  V and  $B = 0$  T. For clarity, the data in both panels is offset vertically by incrementally subtracting a value of  $20 \mu\text{S}$  in (a) and  $40 \mu\text{S}$  in (b). The top most curves have no offset.

magnetic field revealing the well-known Fraunhofer pattern. The area extracted from the periodicity of the Fraunhofer pattern amounts to  $0.16 \mu\text{m}^2$  in close agreement with the geometrical area of  $0.2 \mu\text{m}^2$  deduced from the SEM image. The width of the first lobe is smaller than twice the period of the higher order lobes which indicates non-uniform current flow.

## 7.4 Conclusion

In this paper we reported electrical transport measurements of SGN and SGS junctions with NbTiN superconducting electrodes. In SGN devices with a barrier region near the S contacts, we observe a zero-bias conductance peak, which we think may arise from reflectionless tunneling. While we are unable to identify its origin unambiguously, this peak has a striking resemblance to the recently measured zero-bias anomaly in a candidate topological superconductor  $\text{Cu}_x\text{Bi}_2\text{Se}_3$  [219]. In junctions with transparent interfaces, supercurrents were observed for electrode separations of

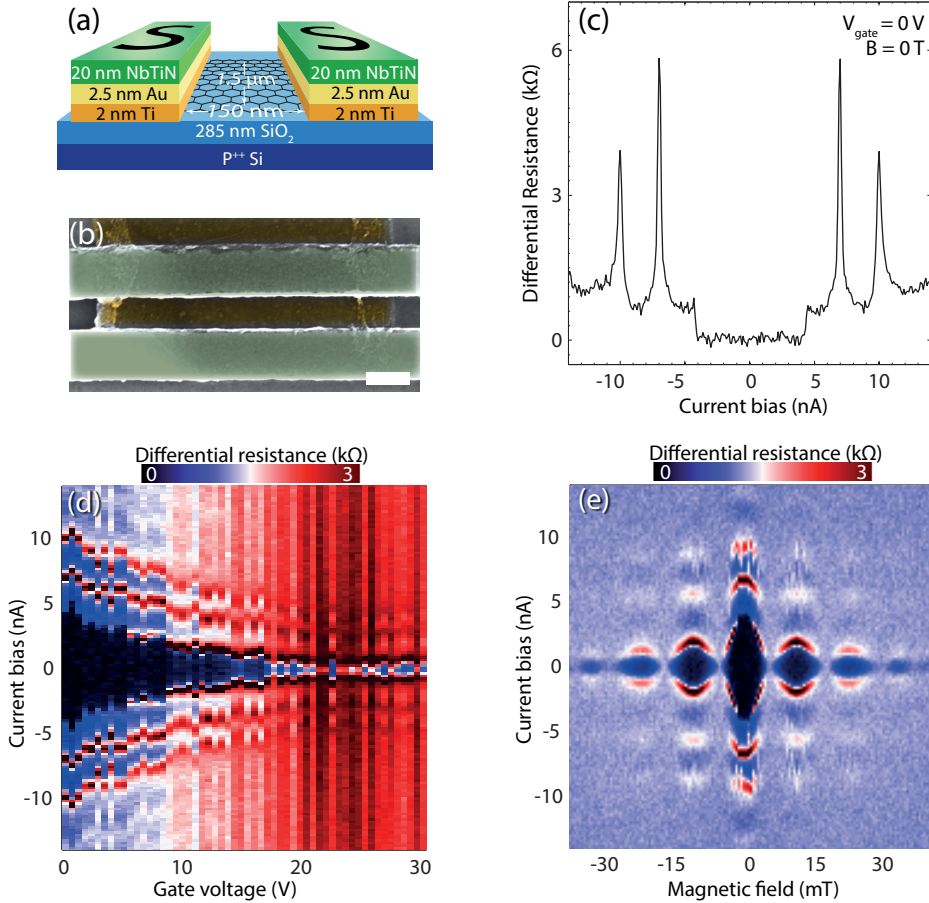


**Figure 7.5:** Type B SGS device with Ti/Au/NbTiN electrodes made without RF cleaning prior to depositing NbTiN. (a) Schematic of the device structure with the relevant dimensions. (b) False color SEM image (scale bar 200 nm). (c) Differential resistance at  $V_{gate} = 0$  V,  $B = 0$  T. (d) Color plot of the differential resistance vs. current bias and gate voltage at  $B = 0$  T. (e) Color plot of the differential conductance vs. magnetic field and current bias at  $V_{gate} = 0$  V.

up to 400 nm. By improving the fabrication procedure we believe that high carrier mobility graphene samples and clean graphene-NbTiN interfaces can be obtained for experimentally investigating specular Andreev reflection and the interplay between Andreev reflection and the quantum Hall effect.

## Acknowledgments

We acknowledge N. Verbruggen, D.J. Thoen, T. Zijlstra, A.M. Goossens, A. Barreiro, C.J.H. Keijzers and S.M. Frolov for discussions and technical support. This work is supported by the Dutch Science Foundation NWO/FOM and by the Eurocores program EuroGraphene.

---

## CHAPTER 8

---

# Mechanical cleaning of graphene

A. M. Goossens, V. E. Calado, A.M. Barreiro, K. Watanabe,  
T. Taniguchi and L. M. K. Vandersypen

Contamination of graphene due to residues from nanofabrication often introduces background doping and reduces electron mobility. For samples of high electronic quality, post-lithography cleaning treatments are therefore needed. We report that mechanical cleaning based on contact mode atomic force microscopy removes residues and significantly improves the electronic properties. A mechanically cleaned dual-gated bilayer graphene transistor with hexagonal boron nitride dielectrics exhibited a mobility of  $\sim 36,000 \text{ cm}^2 \text{ V}^{-1} \text{ s}^{-1}$  at low temperature.

### 8.1 Introduction

High electronic quality is demanded for many graphene experiments [172, 220], but is not easily realized. Graphene samples for electronic measurements are typically made with lithographic methods. Lithography makes a myriad of devices possible, but always leaves resist residues behind. Making contacts to graphene with shadow mask evaporation solves this contamination issue, but this method has many drawbacks concerning the flexibility of the fabrication process. Hence cleaning after lithography is a crucial step towards obtaining high electronic quality samples. There are different methods at hand: chemical cleaning [108], thermal cleaning (annealing in an oven) [157, 221] and current-induced cleaning [10, 30]. Each of these can be very useful but has its own limitations.

In this chapter we present an alternative cleaning method: mechanical cleaning. Scanning a contact mode atomic force microscope (CM AFM) tip over a graphene surface removes residues, removes doping and improves the electronic mobility without damaging the graphene.

---

This chapter is based on the paper titled 'Mechanical cleaning of graphene' *Applied Physics Letters* **100**, 073110 (2012).



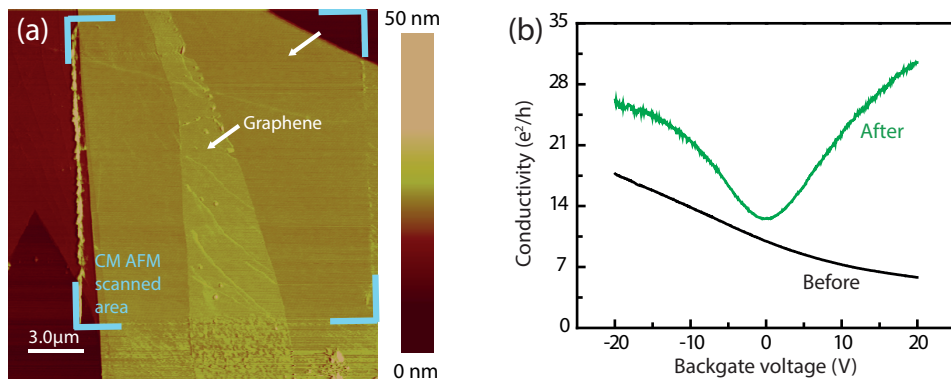


**Figure 8.1:** (a) Tapping mode image of sample A after annealing at 440 °C and contact mode scanning (both with a Veeco Nanoscope IIIa AFM). Only the part within the marked window was scanned with the CM AFM. We chose to show this device because it was much more contaminated than other devices before scanning, so that the effect of the CM AFM scan is easily visible. Wrinkles and some tears on the upper right side of the graphene are induced by the tip but were not observed in other devices. On the left and right of the bounding box, walls of deposited residue are visible. The contacts of the device are not visible in this image. (b) Backgate traces of sample B at room temperature in vacuum ( $I_{bias} = 100$  nA). The black curve is before CM AFM imaging and the green curve after. Using the geometric capacitance, we convert the backgate axis into carrier density. Then we extract the field effect mobility by fitting a straight line to the steepest part of the backgate trace:  $\mu = \left( \frac{t_{SiO_2}}{\epsilon_0 \epsilon_{r,SiO_2}} + \frac{t_{hBN}}{\epsilon_0 \epsilon_{r,hBN}} \right) \frac{d\sigma}{dV}$ , where  $\epsilon_{r,SiO_2} = 3.9$  and  $\epsilon_{r,hBN} = 3.0$ , as calculated from Fig. 8.2a. We extracted the thickness  $t_{hBN}$  from TM AFM images of the devices.

## 8.2 Heat cleaning ineffective

We demonstrate the effectiveness of this method for 4 bilayer graphene on hexagonal boron nitride (hBN) samples. hBN flakes are deposited by mechanical exfoliation on silicon wafers coated with a silicon oxide ( $SiO_2$ ) layer of thickness  $t_{SiO_2} = 285$  nm. On top of the hBN we transfer a bilayer graphene flake using a dry transfer method<sup>1</sup> following the protocol of Ref. [32]. Samples are subsequently annealed in an oven at 400 °C in forming gas<sup>2</sup> to remove residues induced by the transfer process. Cr/Au electrodes are fabricated using electron-beam lithography. We annealed the samples again to remove fabrication residues. While trying to clean the graphene, we repeatedly performed annealing steps with increasing temperatures from 300 °C to a maximum of 440 °C.

After the final annealing step, the samples were often still contaminated. The tapping mode AFM (TM AFM) image of sample A (Fig. 8.1(a)) shows lots of deposited material outside the marked window. The RMS roughness in this area is  $\sim 1$  nm. Before lithography all samples were almost atomically flat with a RMS

<sup>1</sup>The transfer is done at a temperature of 100 °C to remove any water absorbed on the surface of the graphene and hBN flakes.

<sup>2</sup>Ar 2400 sccm, H<sub>2</sub> 700 sccm.

roughness of at most 0.2 nm (limited by the resolution of the AFM).

We characterize the electronic quality of the samples via the residual doping and field effect mobility. Fig. 8.1b (black trace) shows the resistance of sample B as a function of the backgate voltage at room temperature (RT) in vacuum. From this and similar traces for the other devices, we extracted the charge neutrality point ( $V_{np}$ ) and mobility ( $\mu$ ). Depending on the device geometry, we performed 2, 3 or 4 terminal measurements<sup>3</sup>. The results for all samples are summarized in table 8.1. The electronic measurements indicate that most of the devices were highly doped and had a relatively low mobility. Most likely residues on top of the graphene as seen in the AFM images induce doping and provide scattering centers that degrade the electronic quality [222].

### 8.3 Mechanical cleaning with contact mode AFM

To remove the residues we scanned the samples in contact mode AFM with a constant force (Veeco OTR8-35 tip with a stiffness of 0.15 N/m). Hereby the tip is held in contact with the sample surface. We engaged the tip with the lowest force possible. When the tip made contact, we confirmed a reasonable set-point force with the help of a force distance measurement, discussed further below. Then we started scanning the sample with a rate of 0.5 – 1 Hz. For most samples we scanned the same area several times, but without further visible effect.

Tapping mode images taken after scanning in CM AFM show that we cleaned the graphene (Fig. 8.1a inside marked window). The roughness is at most 0.2 nm, similar to the values measured before processing the devices. Further evidence that we removed residues from the graphene are the banks of deposits that are visible in Fig. 8.1a, exactly at the boundaries of the area that was scanned in contact mode.

After CM and TM AFM imaging we again recorded backgate traces at room temperature in vacuum (green curve in Fig. 8.1b). Not only the mobility increased twofold,

<sup>3</sup>In the two and three terminal measurements, contact resistances make the mobility appear lower. To calculate the conductivity from the measured conductance we need the aspect ratio of the devices. As some devices were not rectangular, the aspect ratio was hard to determine and we used an underestimated value in our calculations. Those two factors make the measured mobility a lower bound of the actual mobility.

**Table 8.1:** Results summary for four different samples (measurements in vacuum).

Sample Measurement		A		B	C	D
		2p RT	4p 50mK	3p RT	3p RT	4p RT
$T_{anneal}$	(°C)	440	"	360	360	360
$N_{pass}$	(-)	6	"	1	2	5
$F_{scan}$	(nN)	2.3	"	-2.9	-4.6	-22
$V_{np}$ before	(V)	4	n.a.	>20	>20	17
$V_{np}$ after	(V)	-7	-3	0	1	-1
$\mu$ before	(cm <sup>2</sup> V <sup>-1</sup> s <sup>-1</sup> )	3400	n.a.	1700	260	2700
$\mu$ after	(cm <sup>2</sup> V <sup>-1</sup> s <sup>-1</sup> )	8900	36000	2800	920	6700

but also doping was reduced. For other samples we observed similar behavior (see table 8.1).

### 8.3.1 Double gated device

An attractive feature of mechanical cleaning is that it can be naturally followed by further sample processing. We fabricated sample A into a double gated bilayer device [63, 223]. With the same dry transfer method as mentioned before we stamped an hBN flake on sample A that will act as a topgate dielectric. We defined a topgate electrode across the flake and two voltage probes by e-beam lithography (lower left inset Fig. 8.2a). Resistance as function of the topgate and backgate voltages is plotted in Fig. 8.2a. The resistance peaks that run horizontally are caused by the regions next to the topgated region. The diagonal ridge shows the typical increase of resistance due to opening of the gap with increasing perpendicular electric field [63]. From the upper right inset we extract a (hole) mobility  $\mu$  of  $\sim 36,000 \text{ cm}^2 \text{ V}^{-1} \text{ s}^{-1}$  at carrier density  $n \sim 5 \times 10^{10} \text{ cm}^{-2}$  (corrected for the change in slope due to the neutrality point around 17 V). This value is among the highest found in the literature for bilayer graphene devices, including suspended devices [32, 224, 225].

### 8.3.2 Discussion

We now turn to the mechanism by which CM AFM removes residues from the sample surface. Presumably the tip is plowing through a layer of physisorbed contaminants and thereby 'brooms' the graphene clean, which means the interaction of the tip with the surface is larger than the interaction of the contaminants with the surface. We believe that removing residues is the main explanation for the improvement of the electronic quality of the graphene. In principle the CM AFM might also flatten the graphene, reducing ripples and thereby enhancing mobility. However, we observe no difference in the flatness of graphene before fabrication (presumably equal to the state after lithography) and after mechanical cleaning. Flattening of the graphene should thus play little or no role. The hBN substrate does appear to play a role in improving electronic quality. Jalilian et al. [226] deployed the mechanical cleaning on single layer graphene samples on a  $\text{SiO}_2$  substrate. They also observed an improvement in surface morphology, but electronic quality did not improve. We observed the same behavior in a single layer graphene on  $\text{SiO}_2$  sample.

To gain more insight in the interplay of the surface and the CM AFM tip we took force-distance curves (Fig. 8.2b) in the area we scanned in contact mode. From these curves we can extract the force we were exerting on the sample during scanning, which ranged from  $-22 \text{ nN}$  to  $+2.3 \text{ nN}$  depending on the device. A positive force means the tip was pushing and a negative force that the tip was pulling on the surface. In pulling configuration the tip is held in contact by the Van der Waal's interaction and adhesive forces due to water. The broad range of scanning forces that gave good results illustrates the robustness of the mechanical cleaning method.

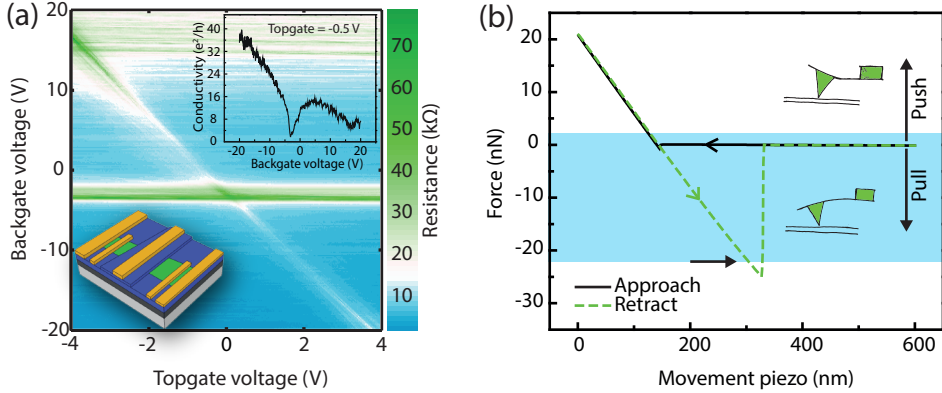


**Figure 8.2:** (a) Measurements on a double gated bilayer graphene transistor fabricated out of sample A. The 4-probe resistance at  $T = 50$  mK is plotted as a function of backgate and topgate voltage ( $V_{bg}$  and  $V_{tg}$  respectively). From the slope of the diagonal line we calculated the relative dielectric constant of the hBN to be 3.0 assuming a parallel plate capacitor model and  $\epsilon_{r, SiO_2} = 3.9$ . The thickness of the bottom hBN flake was 14 nm and the top hBN flake 50 nm, values extracted from AFM images. Lowerleft inset: schematic of the device. Blue colored regions are hBN, green is bilayer graphene and yellow are the contacts and gate. Upperright inset: resistance as a function of  $V_{bg}$  at  $V_{tg} = -0.5$  V. The dip at  $V_{bg} \sim 17$  V is caused by the uncovered graphene part. (b) Force-distance curve of sample D, measured by holding the tip of the AFM in a fixed lateral position and approaching and retracting the tip in the vertical direction. While making these vertical movements, the deflection of the tip is recorded. Assuming that when the tip is in contact with the surface the tip deflects the same distance as the piezo moves, we can calibrate the deflection scale. With the spring constant of the tip we convert that deflection to a force. The horizontal axis has an arbitrary offset. The blue region indicates the range of forces that we used for cleaning the samples. Sample D was scanned at a force of  $-22$  nN as indicated by the arrow. The illustrations picture the pulling and pushing regime.

## 8.4 Conclusions

In summary, scanning bilayer graphene on hBN in CM AFM removes contaminants from the surface, reduces residual doping and significantly improves electronic mobility. A double gated bilayer graphene transistor which was mechanically cleaned in the fabrication process, showed mobilities up to  $\sim 36,000$   $\text{cm}^2 \text{V}^{-1} \text{s}^{-1}$  at 50 mK, and opening of a bandgap. This illustrates the effectiveness of CM AFM for obtaining high-quality graphene devices. Possibly, AFM and scanning tunneling microscope (STM) setups in vacuum could benefit even more from mechanical cleaning as it can be applied in situ, avoiding subsequent contamination by molecules absorbed from the air [157, 227]. This new method is particularly relevant when other cleaning methods are not effective or desirable.

## **Acknowledgments**

We acknowledge useful discussions with A. Castellanos-Gomez and T. van der Sar, experimental support from L. Cantley and financial support from the Foundation for Fundamental Research on Matter (FOM) and the European Research Council (ERC).

---

## CHAPTER 9

---

# Ballistic transport in CVD graphene

V. E. Calado\*, S.E. Zhu\*, S. Goswami, Q. Xu, K. Watanabe,  
T. Taniguchi, G. C. A. M. Janssen and L. M. K. Vandersypen

In this chapter we report the observation of ballistic transport on micron length scales in graphene synthesised by chemical vapour deposition (CVD). The synthesis is done with fine control over the growth parameters in a home-made furnace. This is critical to achieve a nucleation density down to  $\sim 1 \text{ mm}^{-2}$ , which allows us to grow mm scale single crystals. We have adapted a dry transfer method that minimizes contamination and used it to transfer monolayer graphene crystals onto hexagonal boron nitride (hBN) flakes, which are ultra-clean and atomically flat. Transport measurements were done on Hall bar geometries in a liquid He cryostat. We found mobilities in the range of  $10000 - 40000 \text{ cm}^2 \text{ V}^{-1} \text{ s}^{-1}$ . Using non-local measurements we show that electrons can be ballistically directed by a magnetic field (transverse magnetic focussing) over length scales of  $\sim 1 \mu\text{m}$ . Comparison with atomic force microscope measurements suggests a correlation between the absence of wrinkles and the presence of ballistic transport in CVD graphene.

## 9.1 Introduction

High electronic quality in graphene is a key requirement for many experiments and future applications [50]. This has so far been achieved in exfoliated graphene [1] either suspended [30] or on hexagonal boron nitride (hBN) substrates [32]. A hallmark of high electronic quality, apart from carrier mobility, is ballistic transport. Ballistic transport can be detected by a negative resistance in a bend geometry [34, 228]. A more direct observation is by transverse magnetic focussing (TMF), seen two decades ago in GaAs/AlGaAs 2-dimensional electron gas [229] and recently in exfoliated graphene [35].

Chemical vapor deposition (CVD) synthesis of monolayer graphene is a scalable and controllable method for the production of monolayer graphene. The CVD method has shown that large and predominantly monolayer graphene of very high quality can be synthesized on copper foils [73]. Considerable effort has been made to scale it up to meters [7, 230] and to achieve single crystals up to  $\sim\text{mm}$  [231–233]. Despite this

---

\* Contributed equally to this work

effort the electronic quality of CVD graphene is still considered to be inferior to that of exfoliated graphene. The highest charge carrier mobilities are found in CVD graphene on hBN substrate, reaching up to  $30000 - 50000 \text{ cm}^2 \text{ V}^{-1} \text{ s}^{-1}$  [234, 235]. Up to now there are no reports of ballistic transport phenomena in CVD graphene. Polycrystalline CVD graphene contains grain boundaries, which are atomically disordered and thus a cause for (inter-valley) scattering [236, 237]. Therefore they drastically affect the electronic quality [238, 239]. Avoiding grain boundaries (i.e. producing large single crystals) is a prerequisite for achieving long mean free paths. Further processing after growth, such as transferring to hBN flakes, typically causes further degradation. A clean (contaminant-free) and dry procedure is required to transfer CVD graphene to hBN flakes while preserving its quality.

Here we report ballistic transport in graphene grown by the CVD method. In this device ballistic transport emerges in the form of transverse magnetic focussing (TMF). Large-grain-size single crystals of graphene are grown on a folded copper foil enclosure [231] and are dry-transferred to hBN flakes. Hall bars are defined by e-beam lithography and DC transport measurements are done in a liquid He cryostat at 4 K and at room temperature (RT).

## 9.2 CVD growth

A copper foil with a thickness of  $25 \mu\text{m}$  is cut in  $\sim 2 \times 3 \text{ cm}^2$  sheets (Alfa aesar > 99.8% pure). The foil is folded to a fully enclosed pocket and placed inside a quartz tube in a home built tube oven.  $0.5 \text{ sccm CH}_4$  and  $2 \text{ sccm H}_2$  is fed through the tube with a  $\text{CH}_4$  partial pressure of less than  $20 \mu\text{bar}$ . To maximize the growth speed the temperature is set to  $1050 \text{ }^\circ\text{C}$ , close to the Cu melting point. With these parameters we obtain a low nucleation density in the inside of the foil pocket. In Fig. 9.1a we show a scanning electron microscope (SEM) image of seven graphene crystals on copper spread over an area of  $3.1 \times 2.0 \text{ mm}^2$ . This yields a nucleation density of  $\sim 1.1 \text{ mm}^{-2}$ . With such a low nucleation density we are able to grow crystals that have an average diameter of  $\sim 1 \text{ mm}$ . However, in this thesis we used isolated crystals, formed in the early stage of CVD growth, such as shown in Fig. 9.1b. These crystals are about  $150 \mu\text{m}$  across and are grown in about 30 min. The crystals have a sixfold dendritic shape. We note that at the nucleation site a small bilayer starts growing.

In Fig. 9.1c we show a Raman spectrum taken on a graphene crystal similar to those in Fig. 9.1a, after transfer to  $\text{SiO}_2$ . The spectrum confirms that the crystals are monolayer graphene [103] with a defect density below the Raman detection limit, as no D line at  $\sim 1350 \text{ cm}^{-1}$  is visible. In the inset of Fig. 9.1c a transmission electron microscope (TEM) diffraction pattern is shown. It confirms a hexagonal lattice [137]. We have recorded many more diffraction patterns, which show the same lattice orientation over a distance of  $\sim 50 \mu\text{m}$ , see the Supplementary Information, Fig. 9.5. This indicates that the graphene patches in Fig. 9.1a and Fig. 9.1b are monocrystalline, i.e. have no grain boundaries. CVD graphene on copper is transferred onto a hBN flake. The hBN flakes are prepared by mechanical exfoliation on a polymer substrate. From this substrate a  $250 \text{ nm}$  thick hBN is selected and transferred onto e-beam defined tungsten (W) gate electrodes, so that the hBN acts as a gate dielectric. For both transfers we have used a dry method, which is similar to existing methods

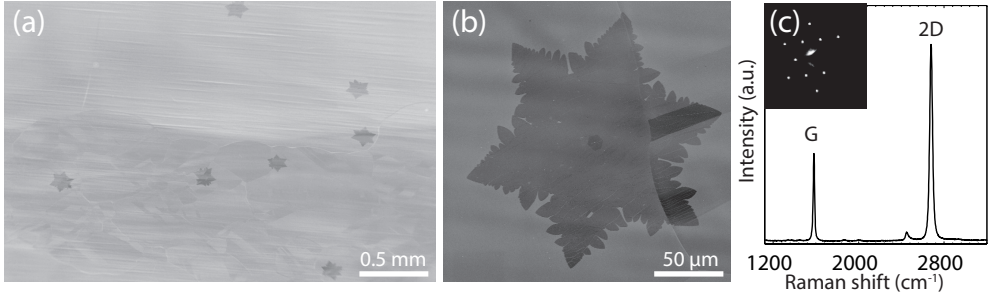


**Figure 9.1:** (a) Scanning electron microscope (SEM) image of a copper foil with isolated graphene crystals after a short growth time. (b) An SEM image of one of the crystals in (a), where the dendritic shape at the edges is visible. The dark stripes are different crystal orientations in the Cu. (c) Raman spectrum taken of another graphene flake transferred from copper to SiO<sub>2</sub>, grown in similar conditions. Inset: a typical diffraction pattern, recorded in a transmission electron microscope (TEM).

for transferring exfoliated graphene [32, 33], see Supplementary Information, Fig. 9.6.

### 9.3 Device

We have contacted the CVD graphene flake with e-beam lithography defined 3 nm Cr / 25 nm Au contacts, Fig. 9.2a, and subsequently etched Hall bars with reactive ion etching in oxygen. In Fig. 9.2b we give a device schematic.

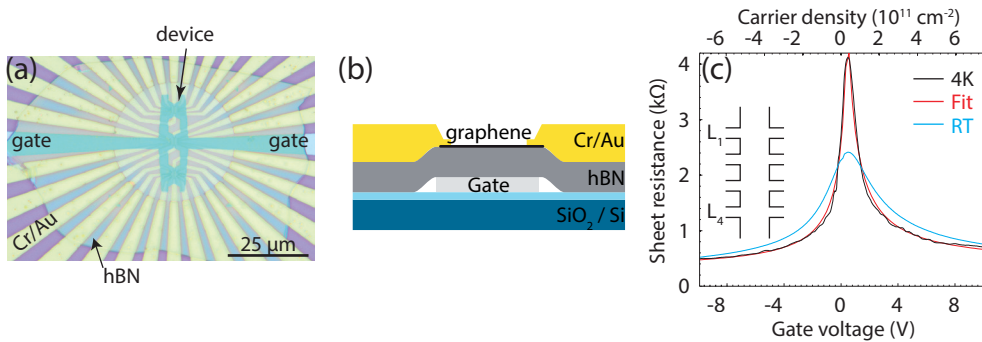


**Figure 9.2:** (a) Optical microscope image of the device. A hBN flake (light blue) is transferred onto a tungsten bottom gate. Yellow stripes are the gold contacts. (b) A schematic side view of the device, with the materials indicated. The hBN acts here as a dielectric between the graphene and W bottom gate. (c) Black and cyan: the sheet resistance as a function of gate voltage and carrier density taken at 4 K respectively room temperature between probes L<sub>1</sub> and L<sub>4</sub> (see inset). Red: a fit to the 4K data using the self-consistent equation for diffusive transport as a model.

Transport measurements were done in vacuum at 4 K and at RT. In Fig. 9.2c we show the sheet resistance measured at 4 K in black and at RT in cyan. The resistance



peak at the charge neutrality point (CNP) became taller and narrower upon cooling as expected. We applied a  $1 \mu\text{A}$  dc current bias across the Hall bar (in the inset) and measured the voltage drop between terminals  $L_1$  and  $L_4$  as a function of gate voltage on the tungsten bottom gate. The charge carrier density is tuned by the gate voltage with a coupling strength of  $7.45 \pm 0.02 \cdot 10^{10} \text{ cm}^{-2} \text{ V}^{-1}$ , extracted from Hall measurements, see Supplementary Information, Fig. 9.7. We find the CNP is offset by  $3.31 \cdot 10^{10} \text{ cm}^{-2}$ , indicating very little background doping.

We characterize the transport properties of the device by fitting the 4K data with the self-consistent Boltzmann equation for diffusive transport that includes long and short range scattering [240, 241]:  $\rho = (ne\mu_c + \sigma_0)^{-1} + \rho_S$ , where  $\mu_c$  is the mobility from long range scattering,  $\sigma_0$  the minimum conductivity at the CNP and  $\rho_s$  the resistivity from short range scattering. This model fits very well to the data when we account for the electron-hole asymmetry by using different fit parameters for the two sides. For the low temperature hole mobility we find  $\mu_h = 41500 \pm 800 \text{ cm}^2 \text{ V}^{-1} \text{ s}^{-1}$ , for the electron mobility  $\mu_e = 28700 \pm 600 \text{ cm}^2 \text{ V}^{-1} \text{ s}^{-1}$ . The RT mobilities are about a factor two lower, see Table S1 in the Supplementary Information.

For the resistivity from short range scattering we obtain  $\rho_S = 280 \pm 10 \Omega$  for holes and  $\rho_S = 380 \pm 10 \Omega$  for electrons. These are higher than what is found earlier for exfoliated flakes on hBN ( $\sim 70 \Omega$ ) [32]. For the residual conductivity  $\sigma_0$  we find a value of  $221 \pm 1.5 \mu\text{S}$ , which is  $5.70 \pm 0.04 e^2/h$ . The mobility values found here are for long range scattering only. The corresponding values for the mean free path are  $200 - 400 \text{ nm}$  for a density of  $7 \cdot 10^{11} \text{ cm}^{-2}$ .

## 9.4 Transverse Magnetic focussing

We further examine the electronic quality of the graphene sheet by looking for transverse magnetic focusing (TMF). The observation of TMF would directly imply the occurrence of ballistic transport. As shown in Fig. 9.3a, we apply a magnetic field perpendicular to the device with a current bias from contact  $L_2$  to  $R_2$ . The Lorentz force will act on the charge carriers and will steer them in a circular orbit with cyclotron radius  $R_c = \hbar k_F / eB$ , where  $R_c$  is the cyclotron radius. Electrons leaving contact  $L_2$  can reach contact  $L_3$  when the cyclotron radius matches one half the distance between the contacts  $L$  and they are not scattered while traveling along the semi-circle joining the contacts. This focussing condition occurs for specific combinations of magnetic field and gate voltage:

$$B = \frac{2\hbar k_F}{eL} \propto \sqrt{V_{gate}}. \quad (9.1)$$

The momentum of the charges,  $\hbar k_F$ , is tuned with the bottom gate voltage  $V_{gate}$ .

When electrons reach contact  $L_3$ , its potential will be raised. We probe this potential by recording the voltage  $V$  between terminal  $L_3$  and B, making the assumption that the potential of the far-away contact B remains constant. The gate voltage and magnetic field are swept and the resistance  $V/I_{bias}$  is plotted on a logarithmic color-scale in Fig. 9.3b.

In Fig. 9.3b above fields of  $\pm 1 \text{ T}$  Shubnikov-de Haas (SdH) oscillations are seen as straight lines diverging for larger magnetic field. However the lines marked with white

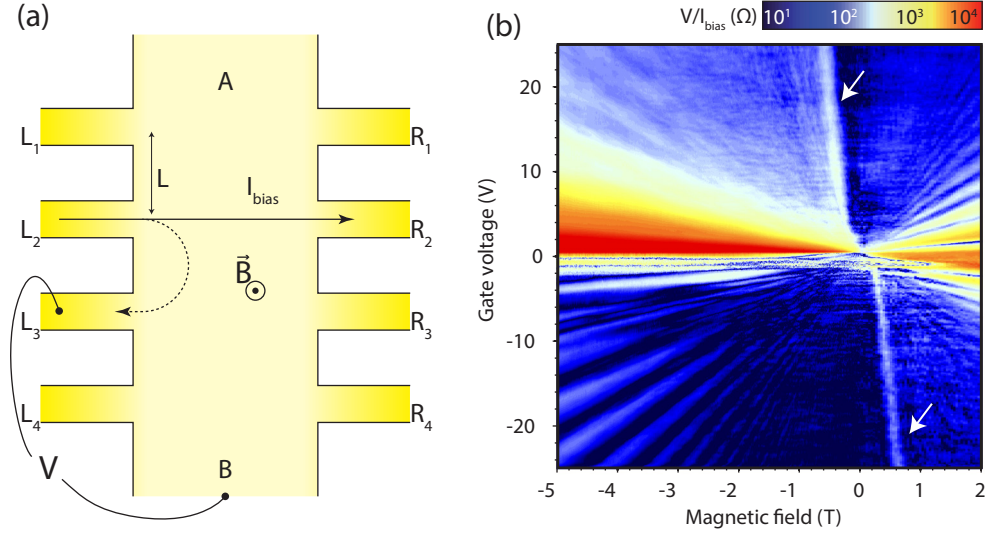


**Figure 9.3:** (a) The non-local measurement configuration for observing magnetic focussing.  $V$  is measured between  $L_3$  and  $B$  while a current bias is applied between  $L_2$  and  $R_2$ . (b) The resistance  $V/I_{bias}$  as function of gate voltage and magnetic field plotted in a logarithmic color scale. The straight lines are due to SdH oscillations and the square-root line is due to TMF, indicated by the arrows.

arrows do not fit the SdH pattern. These lines are attributed to TMF, following from the square-root dependence between the magnetic field and charge carrier density, see Eq. 9.1. For negative field and positive carrier density electrons leaving  $L_2$  are deflected towards contact  $L_3$ , where an increase of the voltage  $V$  is observed. For positive field we find the same square-root dependence, where holes are deflected instead of electrons, as they carry opposite charge. Such behavior can only be observed when the region between the contacts permits ballistic transport, i.e. little scattering takes place.

From a fit to the data, we find a distance of  $L = 570$  nm, which is somewhat larger than the expected lithographic distance of 500 nm, see Supplementary Information Fig. 9.10, for the fitting data. A similar mismatch between the extracted contact separation from TMF and the lithographic distance was recently reported in exfoliated graphene [35].

We have performed analogous measurements across the entire device and except between  $L_1$  and  $L_2$  (See Supplementary Information, Fig. 9.9) no focussing was found in other parts, pointing at the presence of inhomogeneities. In Fig. 9.4a we show an atomic force microscope (AFM) image of the device. In the device a bubble and two wrinkles are present, which may hinder transport. The wrinkles are 1 – 2 nm in height and less than  $\sim 40$  nm in width. The bubbles are about  $\sim 35$  nm high. Given the presence of such wrinkles and bubbles in the Hall bar, the mobility values are remarkably high, in the range of the highest reported mobilities in CVD graphene [234].

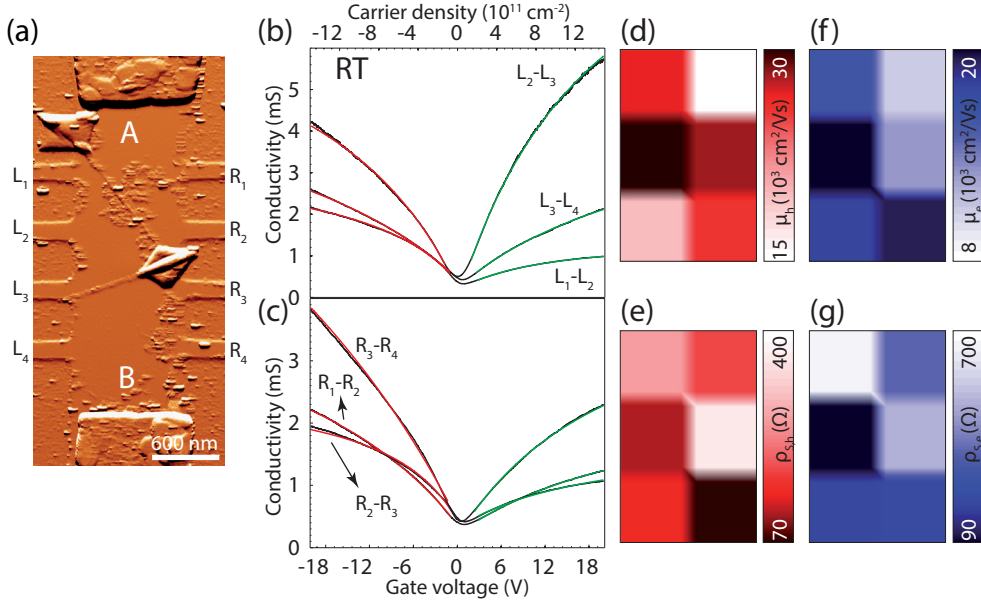


**Figure 9.4:** (a) AFM image of the device. It is shaped in a Hall bar geometry. Wrinkles and a bubble could not be avoided. (b) The conductivity as function of gate voltage and carrier density for the left terminals and in (c) the same measurement for the right terminals. The red and green lines are fits from the self-consistent Boltzmann model.

## 9.5 Inhomogeneous

In Fig. 9.4b and Fig. 9.4c we have plotted the conductivity measured between each pair of neighbouring terminals as a function of gate voltage taken at RT. We note that the curves are all different, which implies that the device is inhomogeneous as can be expected based on the AFM image. We fit the data with the self-consistent Boltzmann equation separately for the hole and electron side over the gate voltage range indicated by the red and green lines (Fig. 9.4b,c). The resulting fitting parameters are given in Table 9.1 in the Supplementary Information. In Fig. 9.4d-g the measured hole and electron mobility and residual resistivity are shown in colours as a spatial map in correspondence to the device. Both mobility and residual resistance vary across the hall bar. Some of the lowest values for the residual resistance and the highest mobility values are found where TMF was most pronounced, at L<sub>2</sub> – L<sub>3</sub>. Here the residual resistance is similar to what is found in exfoliated graphene on hBN [32]. In the other parts with more wrinkles we see most of the time higher values of ρ<sub>S</sub>, which suggests more short range scattering is taking place, presumably from the wrinkles and bubbles. Despite this correlation, we do not find a one-to-one correspondence between TMF and μ or ρ<sub>S</sub>, presumably since μ and ρ<sub>S</sub> are sensitive to scattering over a larger area than TMF. These observations suggest that (CVD) graphene must be flat and clean for it to show ballistic transport.

## 9.6 Conclusion

In summary, we have demonstrated that TMF can be observed in CVD graphene over a distance of almost one micron. The CVD process was optimized to obtain large single crystal flakes. In order to preserve its high quality we have transferred graphene flakes with a dry method onto hBN. The main limitation in electronic quality for the current device appears to be the presence of wrinkles and bubbles. If one can optimize the processing to reduce or eliminate the wrinkles and bubbles, it may be possible to routinely observe ballistic phenomena that only the best exfoliated samples have shown so far. The results are an import step forward in the direction of scalable and controllable graphene production not only for industrial applications but also for fundamental research.

### Acknowledgments

We thank A.M. Goossens for discussions and R. Schouten, R. Luttjeboer, P. van Holst, H. Jansen, L. Schipperheijn for technical assistance and G.F. Schneider and S.R.K. Malladi for preparing TEM samples and the Young Wild Idea Grant from the Delft Centre for Materials (DCMat) for financial support. This work is part of the research program of the Foundation for Fundamental Research on Matter (FOM), which is part of the Netherlands Organization for Scientific Research (NWO).

## 9.7 Supplementary Information

### 9.7.1 TEM

In Fig. 9.5 we show eight diffraction patterns recorded by TEM, using a FEI Titan cube equipped with Cs imaging corrector, operating at 300 kV and 600 °C [242] with a spot size of 100 nm. The measurements are taken in different locations on the same crystal, up to 50  $\mu\text{m}$  apart. The lattice orientation is for all of them the same within the measurement accuracy of 1°. From these measurements we conclude that single crystal domains can extend over at least  $\sim 50 \mu\text{m}$ . In the process of delivering TEM samples, the wedging method has been used to transfer CVD graphene [159].

### 9.7.2 Fabrication of tungsten bottom gates

We have used Si/SiO<sub>2</sub> wafers with 660 nm thermal oxide, supplied by IDB technologies. They are diced in 19 × 19 mm<sup>2</sup> pieces onto which tungsten is sputtered for 80 sec at 2  $\mu\text{Bar}$  using 150 W RF in an Alliance sputtering system. We spincoat a negative e-beam resist. NEB-22, using 1500 rpm for 55 s and bake it for 2 min in an oven at 110 °C. Then the chip is directly loaded into the vacuum of the e-beam pattern generator. A dose of 16  $\mu\text{C cm}^{-2}$  is used to define a bottom gate, bonding pads and e-beam search markers. The exposed substrate is without delay put back in the oven for 2 min at 105 °C for a post bake. The etching mask is developed in MF322 for 30 sec, then two times for 15 sec in 1:10 MF322:H<sub>2</sub>O and finally rinsed for 30 sec in H<sub>2</sub>O. The tungsten is etched in SF<sub>6</sub>/O<sub>2</sub> at a temperature of -70 °C for 30 sec in

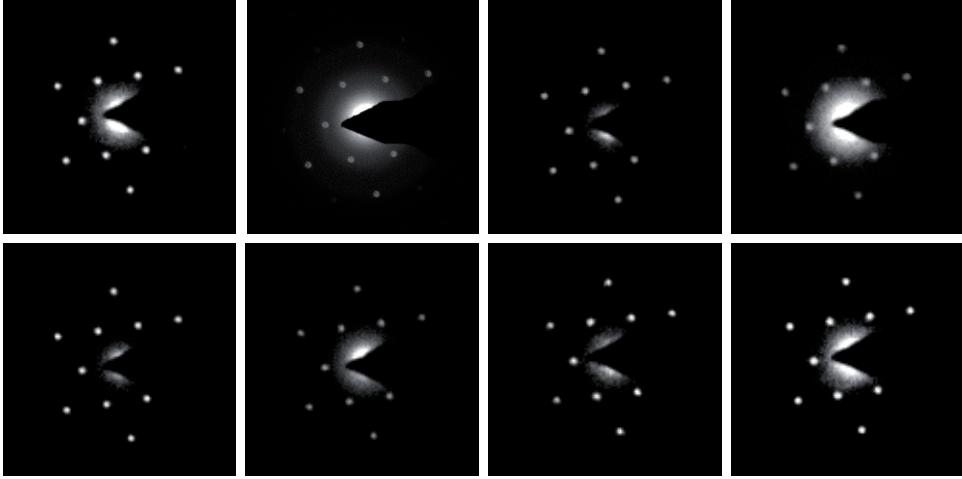


**Figure 9.5:** Eight diffraction patterns taken with TEM in different locations in the same graphene crystal.

a 1100 W DC / 80 W RF plasma with 300 sccm SF<sub>6</sub> and 15 sccm O<sub>2</sub> in a AMS100 Cryo etcher. The mask is removed in an ultrasonic bath of HNO<sub>3</sub> for 1 min, rinsed in H<sub>2</sub>O and subjected to ultrasonication in acetone for 2 min.

### 9.7.3 Preparation of hBN substrates

hBN crystals are produced by the method described in Ref. [243]. The crystals are exfoliated with blue Nitto tape and prepared onto an Elvacite/PVA polymer stack on Si substrates. Next, hBN flakes are located in a standard optical microscope. A Lexan frame is stuck to the Elvacite film and placed in water. While floating on the water surface, water dissolves the PVA layer (Polyvinyl alcohol in 6 wt% H<sub>2</sub>O, Sigma Aldrich 360627) and the Si chip is detached from the Elvacite film with hBN. The frame is gently taken out and flipped. The frame is attached to a micromanipulator in order to align it onto the tungsten bottom gate on the target substrate. Once the hBN with polymer scaffold are in contact with the target substrate a heating stage is set to a temperature of 80 °C, which is well above the 36 °C glass transition temperature of Elvacite. The polymer film is removed by dissolving it in acetone after curing at 80 °C for at least 1 hour. Polymer residues present on the hBN surface are effectively removed by annealing in high vacuum ( $\sim 10^{-6}$  mBar) at 600 °C (W can sustain temperatures > 600 °C). Next, a CVD graphene crystal is transferred and aligned on top of the hBN/gate structure.

## 9.8 Dry Transfer of CVD graphene

Large CVD crystals are present on the inside of the copper foil enclosure. The outside has predominantly small crystals, which are removed by reactive ion etching

in an oxygen plasma, Fig. 9.6a. An Elvacite film<sup>1</sup> is spun on a CVD graphene/Cu foil, which will act as a polymer support, Fig. 9.6b. The Elvacite/CVD graphene/Cu foil is attached to a support frame by a polyamide adhesive, the support frame is not shown in the illustrations. The copper is dissolved in a  $20 \text{ g l}^{-1}$  ammonium persulfate<sup>2</sup> solution for about 3 hours. The support frame is gently taken out of the etchant solution and dried. The result is a support frame with a free standing Elvacite/graphene film, illustrated in Fig. 9.6c without frame. This stack is transparent and is attached to the micromanipulator in a transfer setup and subsequently transferred onto hBN flakes, Fig. 9.6d.

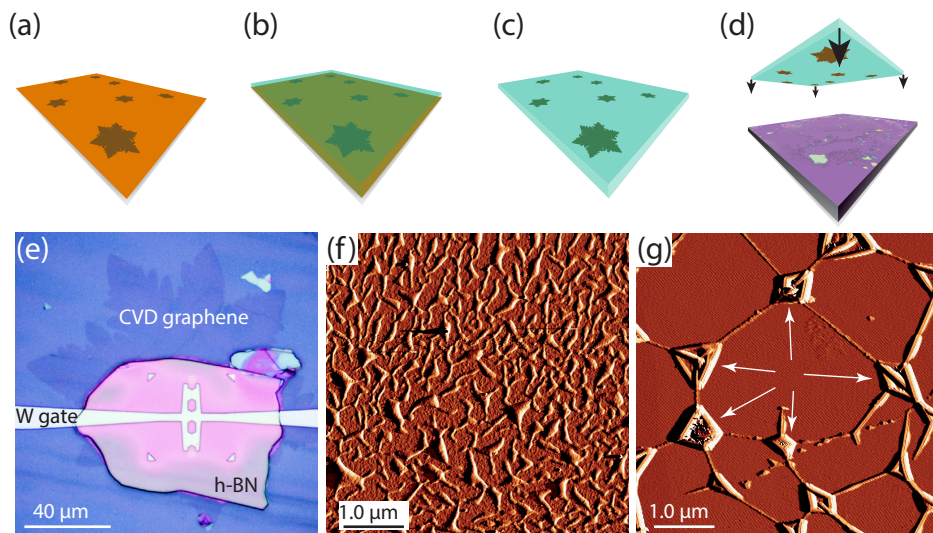


**Figure 9.6:** (a-d) Dry transfer process schematically shown in steps. (e) Optical microscope image of a CVD graphene crystal transferred onto a hBN flake with a W bottom gate. (f) AFM image of the surface of an as transferred CVD graphene crystal on hBN. A lot of residues are present. (g) AFM image of the same surface as in (f), but after annealing in high vacuum ( $\sim 10^{-6}$  mBar) at  $600^\circ\text{C}$

In Fig. 9.6e an optical microscope image is shown of a device consisting of W bottom gates with hBN and CVD graphene transferred on top. An AFM image (Fig. 9.6f) reveals that a lot of residues are present after the transfer of graphene on hBN. Subsequent annealing in high vacuum ( $\sim 10^{-6}$  mBar) at  $600^\circ\text{C}$  yields a surface shown in Fig. 9.6g. Many bubbles are present that are interconnected with each other by wrinkles.

Flat areas are present, where the surface roughness as measured by AFM is  $\sim 0.1$  nm, similar to that of a clean bare hBN surface. To find out what is inside the bubble we performed (on other samples) an oxygen plasma etching step. This removes graphene, but the bubble shape persists. This can also be seen in Fig. 9.3a in the upper left corner. From that we deduce that inside the bubbles a solid substance is present<sup>3</sup>.

<sup>1</sup>Elvacite acrylic resin 2550 dissolved in MIBK,  $\sim 100$  mg/mL, Lucite International, Inc.

<sup>2</sup> $(\text{NH}_4)_2\text{S}_2\text{O}_8$ , ACS reagent,  $\geq 98.0\%$ , Sigma-Aldrich 248614.

<sup>3</sup>Measurements using contact mode AFM on bubbles show that the bubbles are only partly com-

Presumably residues in between the graphene and hBN are present and are mobilised during the annealing process coalescing and forming bubbles.

### 9.8.1 Carrier Density

The charge carrier density is determined by standard Hall measurements. In Fig. 9.7a the resistances  $R_{xx}$  and  $R_{xy}$  are plotted as a function of magnetic field. Here  $R_{xx}$  is measured from the voltage drop between terminal L<sub>1</sub> and L<sub>4</sub> and  $R_{xy}$  from the hall voltage between L<sub>2</sub> and R<sub>2</sub>, while a DC current bias of 0.5  $\mu\text{A}$  was applied from A to B. We can find the carrier density by  $n = (dB/dR_{xy})/e$ . For the derivative we took the slope between 0 T and 1 T extracted from a linear fit. This is done over a gate voltage range of -10 V and +10 V, see Fig. 9.7b. The resulting data points are fitted with a linear function and the slope gives the gate coupling of  $7.45 \pm 0.02 \cdot 10^{10} \text{ cm}^{-2} \text{ V}^{-1}$ . The capacitance per unit area is then 11.9 nF/cm<sup>2</sup>. From the capacitance per unit area we calculate the dielectric constant of hBN by using the parallel plate capacitor model. The thickness of hBN is extracted from AFM measurements, giving 250 nm. This yields a dielectric constant for hBN of  $\epsilon = 3.37 \pm 0.007$ . This value falls in the range of values found in earlier experiments [32, 111].

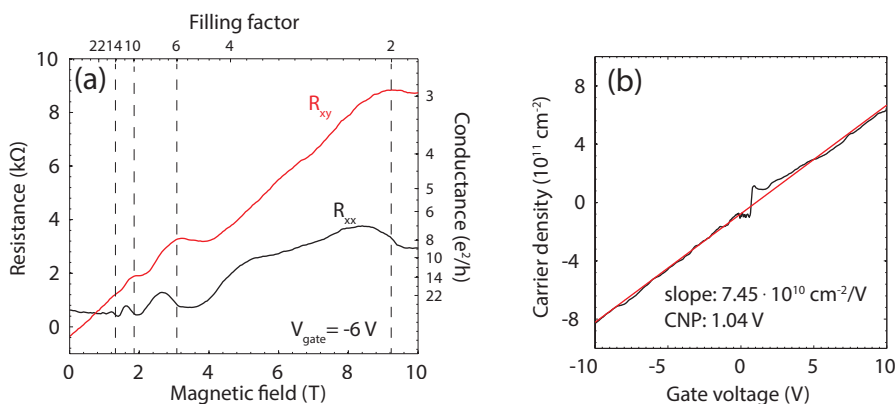


**Figure 9.7:** (a)  $R_{xx}$  and  $R_{xy}$  versus  $B$  at a gate voltage of  $-6 \text{ V}$ . We note that there is a slight offset of  $\sim -400 \Omega$  in  $R_{xy}$ , this could be due to the presence of a small  $R_{xx}$  component. In addition we see that the quantum hall states at filling factor 2, 6, 10, 14 are present but not well developed. (b) The carrier density as function of gate voltage. The data is extracted from the magneto-resistance measurements as in (a). From the linear fit the gate efficiency is calculated to be  $7.45 \cdot 10^{10} \text{ cm}^{-2} \text{ V}^{-1}$ .

### 9.8.2 Field effect mobility

The field effect mobility  $\mu_{FE}$  is calculated using the Drude model of conductivity and is given by  $d\sigma/dn = e\mu_{FE}$ . At zero magnetic field the conductivity is related to the sheet resistance by  $\sigma = 1/\rho$  and taken from Fig. 9.2c. The derivative is calculated by fitting piecewise a linear function over intervals of  $7.2 \cdot 10^{10} \text{ cm}^{-2}$ . From the

---

pressible, which is consistent with the presence of a solid substance inside [111].

resulting slope the mobility as function of carrier density is obtained and plotted in Fig. 9.8. Here the field effect mobility is plotted as a function of carrier density, in red the room temperature data and in black the data taken at 4 K. At high densities ( $7 \cdot 10^{11} \text{ cm}^{-2}$ ) the room temperature mobility is  $\sim 9000 \text{ cm}^2 \text{ V}^{-1} \text{ s}^{-1}$  and close to the CNP it is  $\sim 17000 \text{ cm}^2 \text{ V}^{-1} \text{ s}^{-1}$ . At 4 K this becomes  $\sim 7500 \text{ cm}^2 \text{ V}^{-1} \text{ s}^{-1}$  at high density and  $\sim 29000 \text{ cm}^2 \text{ V}^{-1} \text{ s}^{-1}$  close to the CNP. From comparison with the mobilities extracted from the Boltzmann model (see main text and next paragraph), we notice the effect of short range scatterers on the field effect mobility in some parts of the device.

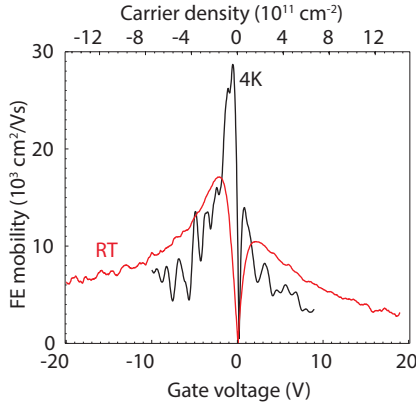


**Figure 9.8:** Field effect mobility as function of gate voltage and carrier density at room temperature in red and at 4 K in black.

### 9.8.3 Fits with self-consistent Boltzmann model

To distinguish between the short range and long range interactions we have fitted a self-consistent Boltzmann model to our data [240, 241]: given by

$$\rho = \begin{cases} \frac{1}{ne\mu_h + \sigma_0} + \rho_{S,h}, & \text{for } n < 0 \\ \frac{1}{ne\mu_e + \sigma_0} + \rho_{S,e}, & \text{for } n > 0 \end{cases}$$

where  $\mu_h$  and  $\mu_e$  is the hole and electron mobility for long range scattering,  $\rho_{S,h}$  and  $\rho_{S,e}$  the resistance from short range scattering for holes and electrons and  $\sigma_0$  the minimum conductivity. This function is fit to the 4K and RT data in the main text and its corresponding fitting parameters are given in Table 9.1.

### 9.8.4 TMF in other parts of the device

A voltage  $V$  is measured between the terminals  $L_1$  and A while a current of  $1 \mu\text{A}$  is applied from  $L_2$  to  $L_3$ , see Fig. 9.9. Here the focussing signal is hardly visible (note that all the features appear at opposite  $B$  as for Fig. 9.3 in the main text, since here the voltage contacts are on the other side of the current contacts). We presume this is due to a pronounced wrinkle that crosses the semi-circle connecting  $L_1$  and  $L_2$  and hinders ballistic transport, see Fig. 9.9b.



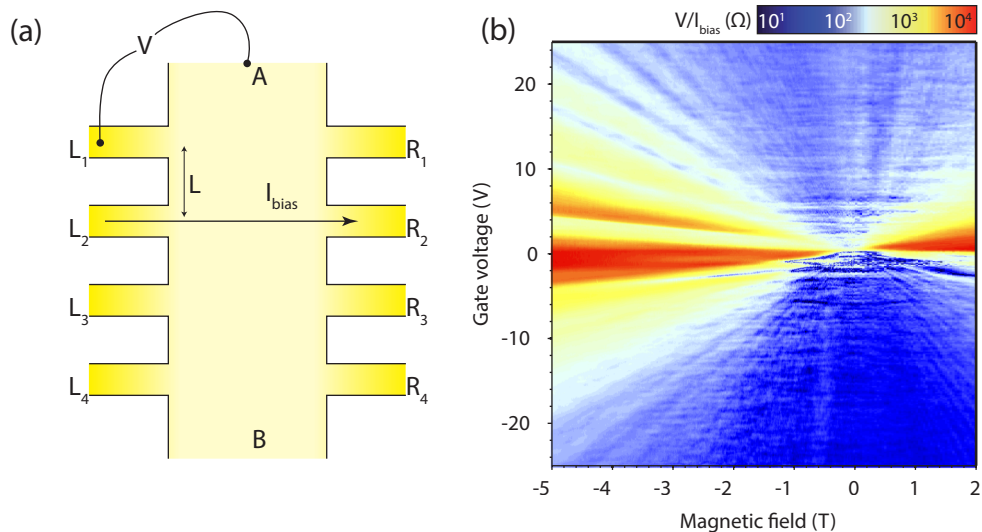


**Figure 9.9:** (a) Another non-local measurement configuration for observing magnetic focussing.  $V$  is measured between  $L_1$  and  $A$  while a current bias is applied between  $L_2$  and  $R_2$ . (b) The resistance  $V/I_{bias}$  as function of gate voltage and magnetic field plotted in a logarithmic color scale.

## 9.9 Extraction of $L$

In order to extract an effective distance  $L$  between the contacts involved in focussing, we zoom in Fig. 9.10a on the TMF feature, for a large range of gate voltages with the same configuration as in Fig. 9.3a. The positions of the resistance maxima

**Table 9.1:** The hole and electron mobility ( $\mu_h$ ,  $\mu_e$ ) are given for different locations in the device, as well as the resistance for short-range interactions  $\rho_{S,h}$  and  $\rho_{S,e}$ . The errors are the standard deviations from the fit parameters.

	$\mu_h$ ( $\text{cm}^2 \text{V}^{-1} \text{s}^{-1}$ )	$\mu_e$ ( $\text{cm}^2 \text{V}^{-1} \text{s}^{-1}$ )	$\rho_{S,h}$ ( $\Omega$ )	$\rho_{S,e}$ ( $\Omega$ )	$T$
$L_1 - L_4$	$41500 \pm 800$	$28700 \pm 600$	$290 \pm 10$	$380 \pm 10$	4 K
$L_1 - L_4$	$19500 \pm 100$	$19200 \pm 100$	$163 \pm 1$	$345 \pm 1$	RT
$L_1 - L_2$	$22200 \pm 100$	$11690 \pm 60$	$293 \pm 1$	$676 \pm 2$	RT
$L_2 - L_3$	$33170 \pm 80$	$48500 \pm 100$	$78 \pm 2$	$85.8 \pm 0.4$	RT
$L_3 - L_4$	$16230 \pm 40$	$14230 \pm 30$	$161.7 \pm 0.6$	$196.9 \pm 0.8$	RT
$R_1 - R_4$	$37300 \pm 500$	$20500 \pm 300$	$369 \pm 5$	$631 \pm 9$	4 K
$R_1 - R_4$	$17930 \pm 70$	$12130 \pm 50$	$199 \pm 1$	$399 \pm 1$	RT
$R_1 - R_2$	$14800 \pm 50$	$8630 \pm 40$	$199 \pm 1$	$370 \pm 2$	RT
$R_2 - R_3$	$24000 \pm 200$	$9500 \pm 100$	$373 \pm 2$	$540 \pm 4$	RT
$R_3 - R_4$	$20600 \pm 130$	$17800 \pm 100$	$74 \pm 2$	$212 \pm 2$	RT

are shown as black dots in Fig. 9.10b. In red we have used a square-root relation as the model dictates in Eq. 9.1, though with an additional magnetic field offset:  $B = a_0\sqrt{n} + a_1$ , where  $a_1 = 90 \pm 20$  mT is ideally expected to be zero. From the fit we find a larger separation than the lithographic separation  $L = 570 \pm 25$  nm. This value is larger than the lithographic distance of 500 nm, which calculated curve we plot in cyan for comparison. This discrepancy is also seen in exfoliated graphene [35]. We note that this model does not fit the data very well at low densities. The offset of  $a_1 = 90 \pm 20$  mT is not likely the cause of an offset in magnetic field, as such large offsets are not expected in our magnet. When forcing the fit through zero the best fit appears to be a sublinear fit with an exponent of  $\sim 0.37$ . This is anomalous to the square-root function, which could be the cause of a non-constant Fermi velocity. A renormalization of the Fermi velocity has been observed in very clean suspended devices [244]. However we can neither attribute this, because that is observed at much lower carrier densities  $< 10^{10}$  cm $^{-2}$ .

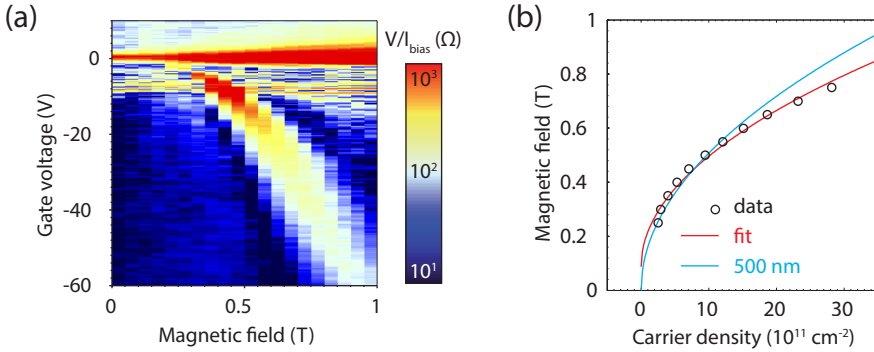


**Figure 9.10:** (a) Resistance as a function of gate voltage and magnetic field. (b) The magnetic field value corresponding to the maxima in the resistance extracted from (a) are plotted as a function of carrier density. In red the best fit square-root function and in cyan eq. 9.1 from the maintext for  $L = 500$  nm.



---

## CHAPTER 10

---

# Outlook

This thesis describes a very diverse set of experiments on graphene. Here we give the current status and discuss which steps can be taken next.

### 10.1 Current status

**Transfer Methods** Many methods have been developed for transferring graphene onto other structures [32, 33, 73, 120–131]. We have developed the wedging transfer method. This method is versatile and does not demand advanced lab equipment, Chapter 4. With this method we are able to quickly transfer exfoliated graphene from  $\text{SiO}_2$  to other substrates. The disadvantage is that the transfer takes place in water, where any contaminants may be trapped after transfer. Secondly wrinkling occurs on strongly hydrophobic surfaces. For achieving clean devices, we use a dry transfer technique for transferring hBN, exfoliated graphene and CVD graphene, adapted from Ref. [32, 33].

**Graphene nanopores** Graphene nanopores are a promising candidate for single molecule detection and DNA sequencing. With a graphene membrane, the thickness can be scaled down to one atomic layer, matching the DNA base pair distance. Using the wedging transfer method we were able to produce graphene nanopore devices with single layer graphene. We have realised translocation of single DNA molecules through a single layer graphene nanopore, Chapter 6. Garaj et al. [67] and Merchant et. al. [68] used few layer CVD graphene. Although their membranes are not as thin, it has the advantage that no alignment is needed during transfer. Currently, CVD grown single layer graphene is well developed too. There are a few proposals to realize single base pair detection. One is by detecting tunnel current through DNA base pairs [173] or by detecting edge currents flowing along a perfect graphene nanoribbon within the middle nanopore [245]. For either of these methods device fabrication is difficult and make the ultimate goal of sequencing very challenging.

**Graphene wrinkles** We have shown that nm sized wrinkles appear in graphene that is transferred on  $\text{SiO}_2$  by the wedging method do not significantly limit the

mobility, Chapter 5. The wrinkles have a height of  $\sim 3$  nm and a width of  $\sim 7$  nm, their interdistance depends on the hydrophobicity of the substrate, but occasionally in the order of  $0.5 - 1 \mu\text{m}$ . Wrinkles also appear in graphene transferred onto hBN, Chapter 9. These have different dimensions, they have a height of  $1 - 2$  nm and a width of  $\sim 40$  nm and they break ballistic transport. At this point it is not clear if that is due to the curvature or the presence of hydrocarbons underneath that are physisorbed to the graphene surface. In that case we have found that only in flat regions ballistic transport was observed and not across wrinkles, Chapter 9. In general wrinkles are not desirable for high-quality graphene devices. In Section 10.2.4 we propose a possible solution.

**Graphene surface cleaning** We have found that in almost all experiments presented in this thesis graphene's electronic properties are strongly dependent on its surface cleanliness. We have developed mechanical cleaning with contact mode AFM and have shown an improvement of the mobility and decrease in residual doping, Chapter 8. This method is useful when oven annealing is no longer successful even up to the highest temperatures we can apply without device damaging ( $\sim 500$  °C), Chapter 3.

**Graphene-superconducting junctions** With the prospect of observing quantum Hall effect with Andreev reflection we have fabricated NbTiN/graphene junctions. In Chapter 7 we found that reflectionless tunnelling takes place at a disordered NbTiN/graphene junction. We have not been able to see clear QHE in combination with Andreev reflection, for two reasons: (1) Our devices were too disordered possibly due to the intense sputtering of the NbTiN and (2) the device geometry was rather wide and short, which makes it harder to develop edge states. Rickhaus et al. [246] have used a square geometry with cleaner junctions. The authors observe a conductance anomaly in quantum Hall plateaus that disappears once the superconductor switched to the normal state at higher fields. Up to now this is the closest observation of the interplay of Andreev reflection with quantum Hall edge states.

**Ballistic transport** We have observed ballistic transport phenomena on micron length scales in CVD synthesized graphene, Chapter 9. This opens the possibility to use CVD graphene as a platform for experiments instead of exfoliated graphene. The main advantage here is that CVD graphene flakes can be as large as  $\sim 1$  mm, which allows easy handling. For instance it can be transferred without precise alignment. Secondly it makes a step forward in scalable and controllable fabrication. This technological improvement is useful for fundamental physics in the sense that it allows to fabricate more complex devices in much higher numbers. Next we may use this method for future experiments such as proposed below.

## 10.2 Near-future experiments

Here we propose experiments that can be executed as a follow up on this thesis, applying technology that has been developed in this thesis.

### 10.2.1 Veselago lens in a $p - n$ junction by CVD graphene

The Veselago lens in graphene was first proposed by Cheianov et al. [76]. The lensing occurs at a graphene  $p - n$  interface, which acts as a boundary between materials with opposite index of refraction, see Section 2.2. To our knowledge there is up to now no experimental work showing Veselago lensing. The closest experiments in that direction is angle dependent transport in  $p - n$  junctions reported by Sutar et al. [247]. However there is no clear experimental demonstration of negative refraction of electrons.

Here we propose a Veselago lens in a single  $p - n$  junction, Fig. 10.1a. In this figure a Hall bar geometry with contacts on either side inclined with angle  $\varphi$  is given. Below the device are split gates that can independently tune the carrier density in the left and the right part of the device. When the gates are biased oppositely a  $p - n$  junction is formed and both sides have opposite index of refraction. A current  $I_{bias}$  is injected in left contact  $i$  and drained in right contact  $g$ . Current is expected to be refracted at the  $p - n$  interface and focused in collector contact  $c$ . If that occurs we measure a voltage  $V$  increase between the collector contact  $c$  and a reference contact  $f$ , that is far away where no currents are expected to flow.

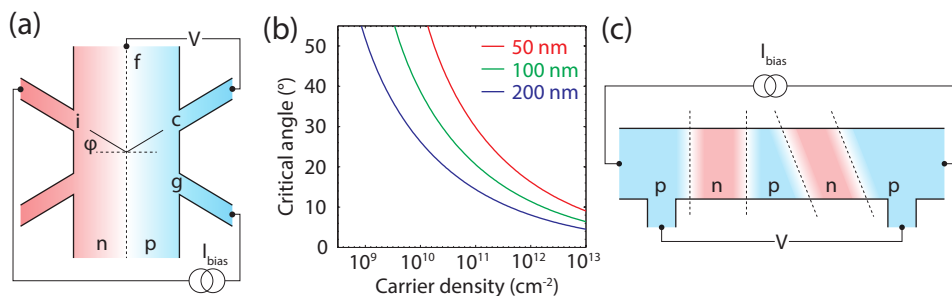


**Figure 10.1:** Electron focussing experiments. (a) A schematic of a device for the Veselago lens experiment. The device is shaped in a Hall bar geometry with tilted contacts with an angle of  $\varphi$ . Underneath are split gates that can change the carrier density independently in the left and the right side. A current is injected from contact  $i$  to contact  $g$ . A voltage drop is measured from the collector contact  $c$  to a contact far away  $f$ . When focussing occurs a fraction of the current will be refracted towards contact  $c$  and a  $V/I_{bias}$  increase is then measured. (b) The critical angle as function of carrier density for different junction widths. This is the typical angle up to which the collimation will take place. The smoother the junction the less collimation and the more reflection off the barrier. (c) A proposed device geometry to measure Klein tunneling on the micron scale, as originally proposed in Ref. [77].

To realise this, one needs ballistic transport across the entire width of the device. This has recently been realised in suspended graphene devices [248, 249]. In that case the gates are below and far away, which makes the  $p - n$  junction smooth, which is useful for achieving highly reflecting barriers but not for achieving refraction at large angles. A sharp junction ( $k_F d \sim 1$ ) allows transmission at higher incident angles, in contrast to a smoother junction ( $k_F d \gg 1$ ) that only transmits at normal incidence (due to the chiral nature). For a Veselago lens device a sharp  $p - n$  junction is required. For that reason nearby gates must be as close as possible to the graphene

sheet, which is difficult in suspended devices. Here we propose to use a thin  $\sim 30 - 50$  nm hBN flake as a gate dielectric. A relatively sharp junction can be made by reactive ion etching a e-beam defined thin line through a metal strip separating the two. Gate separations of  $\sim 40$  nm have already been realised by us in tungsten (W). Next the hBN flake is transferred onto split gates. This yields a junction width of twice the split gate separation which is  $d \sim 100$  nm. This junction width allows transmission up to relatively large incident angles within an accessible range of charge densities [87]. In Fig. 10.1b the critical angle is plotted as function of the carrier density for three different junction widths. The critical angle is taken from full width at half maximum of the transmission probability for smooth junctions from eq. 2.10 in Chapter 2. We expect that graphene on hBN has a charge carrier density fluctuation of  $\sim 10^9$  cm<sup>2</sup> [250], setting a lower limit to the working range of carrier densities. For  $d \sim 100$  nm, this will give a critical angle of  $\sim 40^\circ$  that sets the geometry of the device to an accessible dimension for conventional e-beam lithography, assuming a mean free path of  $1 - 2$   $\mu$ m. Another way of probing transmission angle is using scanning probe microscopy, which can in principle be done without modifying the device design.

Once this has been realised, it paves the road to more complex devices. One is to realise Klein tunneling on micron length scales. Despite the effort so far only indirect observations at sub-micron length scale of Klein tunneling have been reported [251–253]. Following the original proposal [77], we can use our fabrication techniques developed in this thesis to make a series of bottom gates where some are tilted, Fig. 10.1c. A current bias  $I_{bias}$  is applied from the left to the right and a voltage drop  $V$  is measured. Klein tunneling occurs through potential barriers where the transmission equals 1 at normal incidence. The transmission can be blocked at specific angles of incidence depending on the barrier height. This can be tested by a set of two gates in parallel with one tilted. It is required here that the device is ballistic over the entire range.

## 10.2.2 Double-gated twisted CVD bilayer

Bilayer graphene is AB' (or Bernal) stacked, this means that the A atom of the bottom layer aligns with the B' atom of the top layer. An energy gap will open when the layers are at different energies, due to the lifting of the sublattice degeneracy [63, 254].

When the two layers are twisted the electronic structure is strongly affected [255]. A periodic Moiré superlattice will form. This is shown in Fig. 10.2c. Here two lattices are on top of each other with a small twist angle of  $\theta = 2^\circ$  with respect to AA'. The white areas are AA' stacked and the blue and the red are AB' and BA' stacked, Fig. 10.2b. An electric field opens a gap only in the AB' and BA' regions, shown in black in Fig. 10.2d. Here black is gapped and white is metallic. Topological protected modes appear in between the AB' and BA' gapped regions, connecting the metallic AA' regions indicated by the white arrows [256]. The result is a new periodic network consisting of valley current vortices [257]. This is predicted for large Moiré periods and thus small twist angles  $\theta < 1^\circ$ . Coexisting AA' and AB' electronic configurations have recently been observed in angle resolved photoemission spectroscopy (ARPES) in twisted bilayers with a small twist angle of  $0.1^\circ$  [258].

At somewhat larger twist angles  $1^\circ < \theta < 3^\circ$  a Hofstadter butterfly spectrum is

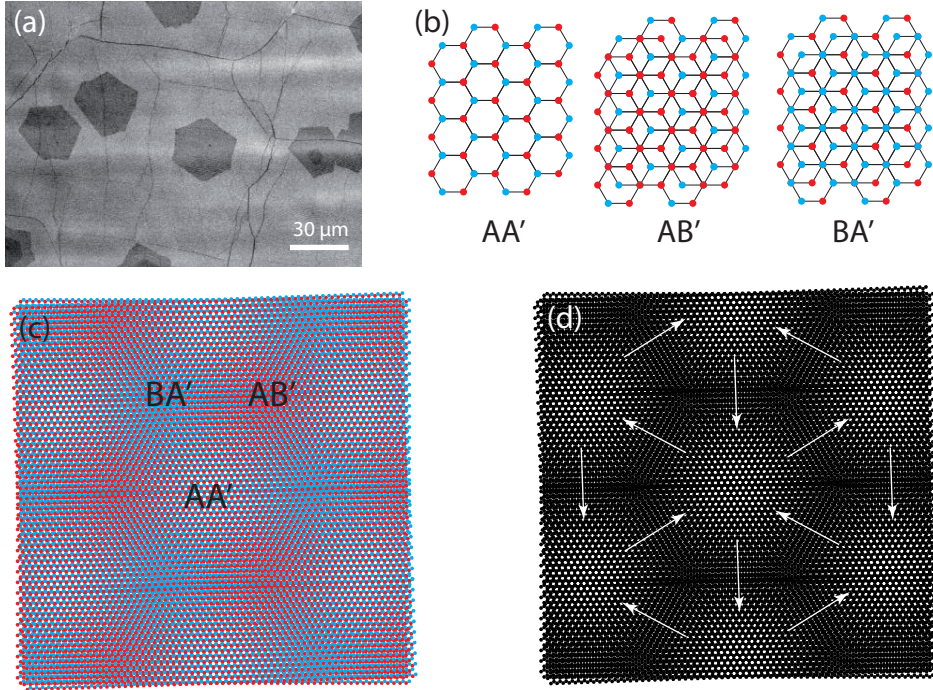


**Figure 10.2:** (a) An SEM image of CVD graphene on Cu foil. The dark hexagons are a second layer grown on top (or below) of the first layer. From the orientation of the edges we see that the two layers are most certainly twisted. (b) Three different lattice configurations for twisted bilayer, for AA' the lattices are precisely on top of each other. For AB' and BA' the lattices are exactly one carbon-carbon bond length shifted. (c) A periodic Moiré pattern, with a twist angle of  $\theta^{\circ}$ . The colors correspond to the lattice orientations. (c) For small twist angles a gap can be opened in the AB' and BA' sites where in between topological protected chiral states connect the metallic AA' sites.

predicted [259]. In addition in this regime a Van Hove singularity (VHS) in the density of states at the M point has been observed in scanning tunneling measurements (STM) at accessible energies [260]. At a VHS in the density of states new phases of matter are predicted, such as chiral superconductivity [261].

At large twist angles,  $3^{\circ} < \theta < 30^{\circ}$ , the layers are decoupled and behave as two separated monolayers. This has been realised with two transferred exfoliated graphene flakes [262]. With that approach there is very little control of the twist angle.

Recently our collaborators<sup>1</sup> have grown bilayer graphene with the same CVD method as described in Chapter 9. An SEM image is shown in Fig. 10.2a. Here the dark contrasted hexagons are randomly distributed bilayers. In the background, a continuous film of monolayer is present. The hexagon shaped bilayers are all rotated with respect to each other, implying that there must be a twist with the bottom layer<sup>2</sup>. This is also seen in recent transport measurements done in CVD graphene

<sup>1</sup>Shou-En Zhu and Guido Janssen.

<sup>2</sup>We assume here that the second layer is grown on top of the first, we have no evidence for that.



bilayers [263]. What remains to be seen is what the twist angles are and which bilayer flakes are below  $\theta < 3^\circ$ . The most direct measurement would be to measure the Moiré period in STM. Recently it has been shown that Raman spectroscopy can be used as well to measure the twist angles to a few degree accuracy [264, 265]. Once the twist angle is known, we transfer the twisted CVD graphene onto a hBN flake. We contact the flake with metal contacts and cap it off with a second hBN flake, onto which we deposit a top gate. We have a twisted bilayer devices sandwiched between two hBN flakes with bottom and top gates.

We can look for Hofstadter’s butterfly spectrum when applying a magnetic field. Furthermore, we can start to explore the electronic properties near VHS at accessible energies and explore new phases of matter. For very small twist angles chiral networks should exist, which strength is controlled by the external gates. We speculate that it should somehow respond to a in plane magnetic field. Twisted bilayer graphene devices can be a very interesting and yet largely unexplored direction.

### 10.2.3 Superconductivity

Clean graphene-superconductor interfaces are desirable for many interesting experiments such as specular Andreev reflection and the coexistence of quantum Hall edge state with Andreev reflection. In the experiments described in this thesis and in earlier work [216], progress has been made to realise these devices. Despite the effort either the graphene was of low quality or the junction transparency was too poor. In these experiments a titanium sticking layer was e-beam evaporated in a different system than where the NbTiN superconducting film is sputtered. Prior to the sputtering the titanium oxide had to be removed by an energetic plasma, which damaged the graphene despite efforts to protect it with an etch mask.

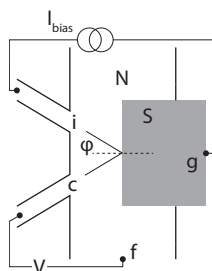


**Figure 10.3:** Proposed device design for observing specular Andreev reflection (SAR). When the carrier density is low enough SAR takes it over from retro-reflection and a charges are Andreev reflected towards contact c.

An improvement would be to use CVD graphene<sup>3</sup> on hBN of high-quality something we recently achieved. Next a titanium protection layer is e-beam evaporated on the graphene onto which subsequently the NbTiN superconducting film is sputtered,

<sup>3</sup>It may be that the second layer grows in between the first layer and the Cu.

<sup>3</sup>Exfoliated graphene is suitable as well, however CVD graphene showing similar quality has an advantage of higher throughput than exfoliated.

this can now be done in one system. In this way the vacuum does not have to be broken and no damage from an energetic plasma has to take place.

In Fig. 10.3 we propose a device design for observing specular Andreev reflection (SAR) in a similar way as the Veselago lens device. See more about the analogies between  $p-n$  junction and Andreev reflection in Ref. [100]. Current is applied from  $i$  to the superconductor contact  $g$ . A voltage is measured at the collector contact  $c$  relative to a contact far away. When SAR takes place charges are Andreev reflected towards contact  $c$  and increase or decrease of  $V$  should be measured, depending on the polarity of the carriers. When the gate voltage is swept above the superconducting gap solely retro reflection takes place and no carriers arrive at contact  $c$ . For this device it is required that the potential fluctuations, typically on  $h\nu \sim 5$  meV [250], are either slowly varying across the superconductor or small compared to the superconducting gap and the mean free path must be larger than the device width.

### 10.2.4 Technology

Here we propose a few technological improvements.

- **Vacuum transfer**

Up to now transfers of hBN and graphene have been done in atmospheric conditions outside a cleanroom. Wrinkles and bubbles always appear after the transfer. Any contamination in air or on a surface may be trapped once transferred. This could be the cause of wrinkles. A transfer in vacuum is therefore appealing. We have developed a small holder in which we can mount the target substrate (i.e. substrate with hBN flake) and clamp the frame with the polymer scaffold (i.e. the graphene). The layers are aligned with respect to each other in a microscope with a micromanipulator. Next, the frame is clamped and the holder is taken away from the microscope. With a screw on the bottom we can then move the target substrate onto the polymer scaffold. The holder can be placed in a vacuum oven. Once in vacuum the polymer film touches the substrate but is not yet sticking. To make them stick the temperature is increased to 80 °C. At that temperature the polymer melts onto the substrate. Then the holder can be taken out and two polymer is stuck onto the substrate and a transfer in vacuum is done.

- **Eliminating bubbles**

Recently we have seen in some cases that the wrinkles disappear when we do an annealing treatment with slow ramp up times and slow ramp down times. Up to now it is poorly understood why this happened. This needs to be further investigated in order to precisely understand the mechanism or at least the correct parameters. It may be the solution to the wrinkle problem.

- **hBN capping**

We have noticed in AFM measurements that after etching graphene in a desired shape polymer residues are present that are impossible to remove, apart from mechanical cleaning. We propose to cap off the clean graphene with a thin layer of hBN and then etch the desired shape through both layers. In that case residues are touching the hBN and not the graphene.

- **Synthetic large area hBN**

As we now use CVD graphene, we are no longer limited by the size of the graphene flakes but by the exfoliated hBN flakes. A way to produce large scale hBN is by a CVD method [266]. This would be a very attractive alternative to the current exfoliated hBN.

---

# Bibliography

- [1] K. S. Novoselov, A. K. Geim, S. V. Morozov, D. Jiang, Y. Zhang, S. V. Dubonos, I. V. Grigorieva, and A. A. Firsov, Electric field effect in atomically thin carbon films, *Science* **306**, 666–669 (2004).
- [2] K. S. Novoselov, A. K. Geim, S. V. Morozov, D. Jiang, M. I. Katsnelson, I. V. Grigorieva, S. V. Dubonos, and A. A. Firsov, Two-dimensional gas of massless Dirac fermions in graphene., *Nature (London)* **438**, 197–200 (2005).
- [3] Y. Zhang, Y.-W. Tan, H. L. Stormer, and P. Kim, Experimental observation of the quantum Hall effect and Berry’s phase in graphene, *Nature (London)* **438**, 201–204 (2005).
- [4] K. S. Novoselov, Nobel lecture: graphene: materials in the flatland, *Rev. Mod. Phys.* **83**, 837–849 (2011).
- [5] A. K. Geim, Random walk to graphene (Nobel lecture), *Angew. Chem. Int. Ed.* **50**, 6966–6985 (2011).
- [6] R. R. Nair, P. Blake, A. N. Grigorenko, K. S. Novoselov, T. J. Booth, T. Stauber, N. M. R. Peres, and A. K. Geim, Fine structure constant defines visual transparency of graphene, *Science* **320**, 1308–1308 (2008).
- [7] S. Bae, H. Kim, Y. Lee, X. Xu, J.-S. Park, Y. Zheng, J. Balakrishnan, T. Lei, H. Ri Kim, Y. I. Song, Y.-J. Kim, K. S. Kim, B. Ozyilmaz, J.-H. Ahn, B. H. Hong, and S. Iijima, Roll-to-roll production of 30-inch graphene films for transparent electrodes, *Nat. Nanotechnol.* **5**, 574–578 (2010).
- [8] C. Lee, X. Wei, J. W. Kysar, and J. Hone, Measurement of the elastic properties and intrinsic strength of monolayer graphene, *Science* **321**, 385–388 (2008).
- [9] P. Neugebauer, M. Orlita, C. Faugeras, A.-L. Barra, and M. Potemski, How perfect can graphene be?, *Phys. Rev. Lett.* **103**, 136403 (2009).
- [10] J. Moser, A. Barreiro, and A. Bachtold, Current-induced cleaning of graphene, *Appl. Phys. Lett.* **91**, 163513 (2007).
- [11] A. A. Balandin, S. Ghosh, W. Bao, I. Calizo, D. Teweldebrhan, F. Miao, and C. N. Lau, Superior thermal conductivity of single-layer graphene, *Nano Lett.* **8**, 902–907 (2008).
- [12] A. A. Balandin, Thermal properties of graphene and nanostructured carbon materials, *Nat. Mater.* **10**, 569–581 (2011).
- [13] S. Chen, Q. Wu, C. Mishra, J. Kang, H. Zhang, K. Cho, W. Cai, A. A. Balandin, and R. S. Ruoff, Thermal conductivity of isotopically modified graphene, *Nat. Mater.* **11**, 203–207 (2012).
- [14] W. Bao, F. Miao, Z. Chen, H. Zhang, W. Jang, C. Dames, and C. N. Lau, Controlled ripple texturing of suspended graphene and ultrathin graphite membranes, *Nat. Nanotechnol.* **4**, 562–566 (2009).

- [15] K. S. Kim, Y. Zhao, H. Jang, S. Y. Lee, J. M. Kim, K. S. Kim, J.-H. Ahn, P. Kim, J.-Y. Choi, and B. H. Hong, Large-scale pattern growth of graphene films for stretchable transparent electrodes, *Nature (London)* **457**, 706–710 (2009).
- [16] J. S. Bunch, S. S. Verbridge, J. S. Alden, A. M. van der Zande, J. M. Parpia, H. G. Craighead, and P. L. McEuen, Impermeable atomic membranes from graphene sheets, *Nano Lett.* **8**, 2458–2462 (2008).
- [17] H. W. Kroto, J. R. Heath, S. C. O’Brien, R. F. Curl, and R. E. Smalley, C<sub>60</sub>: Buckminsterfullerene, *Nature (London)* **318**, 162–163 (1985).
- [18] S. Iijima, Helical microtubules of graphitic carbon, *Nature (London)* **354**, 56–58 (1991).
- [19] A. K. Geim and K. S. Novoselov, The rise of graphene, *Nat. Mater.* **6**, 183–191 (2007).
- [20] N. D. Mermin, Crystalline order in two dimensions, *Phys. Rev.* **176**, 250–254 (1968).
- [21] J. A. Venables, G. D. T. Spiller, and M. Hanbucken, Nucleation and growth of thin films, *Rep. Prog. Phys.* **47**, 399 (1984).
- [22] J. W. Weber, V. E. Calado, and M. C. M. van de Sanden, Optical constants of graphene measured by spectroscopic ellipsometry, *Appl. Phys. Lett.* **97**, 091904 (2010).
- [23] S. P. Koenig, N. G. Boddeti, M. L. Dunn, and J. S. Bunch, Ultrastrong adhesion of graphene membranes, *Nat. Nanotechnol.* **6**, 543–546 (2011).
- [24] P. Blake, E. W. Hill, A. H. C. Neto, K. S. Novoselov, D. Jiang, R. Yang, T. J. Booth, and A. K. Geim, Making graphene visible, *Appl. Phys. Lett.* **91**, 063124 (2007).
- [25] V. Geringer, M. Liebmann, T. Echtermeyer, S. Runte, M. Schmidt, R. Rckamp, M. C. Lemme, and M. Morgenstern, Intrinsic and extrinsic corrugation of monolayer graphene deposited on SiO<sub>2</sub>, *Phys. Rev. Lett.* **102**, 076102 (2009).
- [26] C. H. Lui, L. Liu, K. F. Mak, G. W. Flynn, and T. F. Heinz, Ultraflat graphene, *Nature (London)* **462**, 339–341 (2009).
- [27] P. M. Ostrovsky, I. V. Gornyi, and A. D. Mirlin, Electron transport in disordered graphene, *Phys. Rev. B* **74**, 235443 (2006).
- [28] Z. H. Ni, L. A. Ponomarenko, R. R. Nair, R. Yang, S. Anissimova, I. V. Grigorieva, F. Schedin, P. Blake, Z. X. Shen, E. H. Hill, K. S. Novoselov, and A. K. Geim, On resonant scatterers as a factor limiting carrier mobility in graphene, *Nano Lett.* **10**, 3868–3872 (2010).
- [29] M. Monteverde, C. Ojeda-Aristizabal, R. Weil, K. Bennaceur, M. Ferrier, S. Guéron, C. Glattli, H. Bouchiat, J. N. Fuchs, and D. L. Maslov, Transport and elastic scattering times as probes of the nature of impurity scattering in single-layer and bilayer graphene, *Phys. Rev. Lett.* **104**, 126801 (2010).
- [30] K. Bolotin, K. Sikes, Z. Jiang, M. Klima, G. Fudenberg, J. Hone, P. Kim, and H. Stormer, Ultrahigh electron mobility in suspended graphene, *Solid State Commun.* **146**, 351–355 (2008).
- [31] X. Du, I. Skachko, A. Barker, and E. Y. Andrei, Approaching ballistic transport in suspended graphene, *Nat. Nanotechnol.* **3**, 491–495 (2008).
- [32] C. Dean, A. Young, I. Meric, C. Lee, L. Wang, S. Sorgenfrei, K. Watanabe, T. Taniguchi, P. Kim, K. Shepard, and J. Hone, Boron nitride substrates for high-quality graphene electronics, *Nat. Nanotechnol.* **5**, 722–726 (2010).
- [33] P. J. Zomer, S. P. Dash, N. Tombros, and B. J. van Wees, A transfer technique for high mobility graphene devices on commercially available hexagonal boron nitride, *Appl. Phys. Lett.* **99**, 232104 (2011).

- [34] A. S. Mayorov, R. V. Gorbachev, S. V. Morozov, L. Britnell, R. Jalil, L. A. Ponomarenko, P. Blake, K. S. Novoselov, K. Watanabe, T. Taniguchi, and A. K. Geim, Micrometer-scale ballistic transport in encapsulated graphene at room temperature, *Nano Lett.* **11**, 2396–2399 (2011).
- [35] T. Taychatanapat, K. Watanabe, T. Taniguchi, and P. Jarillo-Herrero, Electrically tunable transverse magnetic focusing in graphene, *Nat. Phys.* **9**, 225–229 (2013).
- [36] F. Amet, J. R. Williams, K. Watanabe, T. Taniguchi, and D. Goldhaber-Gordon, Insulating behavior at the neutrality point in single-layer graphene, *Phys. Rev. Lett.* **110**, 216601– (2013).
- [37] A. M. Goossens, S. C. M. Driessen, T. A. Baart, K. Watanabe, T. Taniguchi, and L. M. K. Vandersypen, Gate-defined confinement in bilayer graphene-hexagonal boron nitride hybrid devices, *Nano Lett.* **12**, 4656–4660 (2012).
- [38] R. V. Gorbachev, A. K. Geim, M. I. Katsnelson, K. S. Novoselov, T. Tudorovskiy, I. V. Grigorieva, A. H. MacDonald, S. V. Morozov, K. Watanabe, T. Taniguchi, and L. A. Ponomarenko, Strong Coulomb drag and broken symmetry in double-layer graphene, *Nat. Phys.* **8**, 896–901 (2012).
- [39] L. A. Ponomarenko, R. V. Gorbachev, G. L. Yu, D. C. Elias, R. Jalil, A. A. Patel, A. Mishchenko, A. S. Mayorov, C. R. Woods, J. R. Wallbank, M. Mucha-Kruczynski, B. A. Piot, M. Potemski, I. V. Grigorieva, K. S. Novoselov, F. Guinea, V. I. Fal’ko, and A. K. Geim, Cloning of Dirac fermions in graphene superlattices, *Nature (London)* **497**, 594–597 (2013).
- [40] B. Hunt, J. D. Sanchez-Yamagishi, A. F. Young, M. Yankowitz, B. J. LeRoy, K. Watanabe, T. Taniguchi, P. Moon, M. Koshino, P. Jarillo-Herrero, and R. C. Ashoori, Massive Dirac fermions and Hofstadter butterfly in a van der Waals heterostructure, *Science* **340**, 1427–1430 (2013).
- [41] C. R. Dean, L. Wang, P. Maher, C. Forsythe, F. Ghahari, Y. Gao, J. Katoch, M. Ishigami, P. Moon, M. Koshino, T. Taniguchi, K. Watanabe, K. L. Shepard, J. Hone, and P. Kim, Hofstadter’s butterfly and the fractal quantum Hall effect in Moiré superlattices, *Nature* **497**(7451), 598–602 (2013).
- [42] B. Radisavljevic, A. Radenovic, J. Brivio, V. Giacometti, and A. Kis, Single-layer MoS<sub>2</sub> transistors, *Nat. Nanotechnol.* **6**, 147–150 (2011).
- [43] A. Castellanos-Gomez, M. Barkelid, A. M. Goossens, V. E. Calado, H. S. J. van der Zant, and G. A. Steele, Laser-thinning of MoS<sub>2</sub>: On demand generation of a single-layer semiconductor, *Nano Lett.* **12**, 3187–3192 (2012).
- [44] O. Lopez-Sanchez, D. Lembke, M. Kayci, A. Radenovic, and A. Kis, Ultrasensitive photodetectors based on monolayer MoS<sub>2</sub>, *Nat. Nanotechnol.* **8**, 497–501 (2013).
- [45] H. Fang, S. Chuang, T. C. Chang, K. Takei, T. Takahashi, and A. Javey, High-performance single layered WSe<sub>2</sub> p-FETs with chemically doped contacts, *Nano Lett.* **12**, 3788–3792 (2012).
- [46] K. S. Novoselov, D. Jiang, F. Schedin, T. J. Booth, V. V. Khotkevich, S. V. Morozov, and A. K. Geim, Two-dimensional atomic crystals, *P. Natl. A. Sci. USA* **102**, 10451–10453 (2005).
- [47] S. Z. Butler, S. M. Hollen, L. Cao, Y. Cui, J. A. Gupta, H. R. Gutierrez, T. F. Heinz, S. S. Hong, J. Huang, A. F. Ismach, E. Johnston-Halperin, M. Kuno, V. V. Plashnitsa, R. D. Robinson, R. S. Ruoff, S. Salahuddin, J. Shan, L. Shi, M. G. Spencer, M. Terrones, W. Windl, and J. E. Goldberger, Progress, challenges, and opportunities in two-dimensional materials beyond graphene, *ACS Nano* **7**, 2898–2926 (2013).
- [48] L. Britnell, R. V. Gorbachev, R. Jalil, B. D. Belle, F. Schedin, A. Mishchenko, T. Georgiou, M. I. Katsnelson, L. Eaves, S. V. Morozov, N. M. R. Peres, J. Leist, A. K. Geim, K. S. Novoselov, and L. A. Ponomarenko, Field-effect tunneling transistor based on vertical graphene heterostructures, *Science* **335**, 947–950 (2012).

- [49] T. Georgiou, R. Jalil, B. D. Belle, L. Britnell, R. V. Gorbachev, S. V. Morozov, Y.-J. Kim, A. Gholinia, S. J. Haigh, O. Makarovskiy, L. Eaves, L. A. Ponomarenko, A. K. Geim, K. S. Novoselov, and A. Mishchenko, Vertical field-effect transistor based on graphene-WS<sub>2</sub> heterostructures for flexible and transparent electronics, *Nat. Nanotechnol.* **8**, 100–103 (2013).
- [50] K. S. Novoselov, V. I. Falko, L. Colombo, P. R. Gellert, M. G. Schwab, and K. Kim, A roadmap for graphene, *Nature (London)* **490**, 192–200 (2012).
- [51] F. Bonaccorso, Z. Sun, T. Hasan, and A. C. Ferrari, Graphene photonics and optoelectronics, *Nat. Photonics* **4**, 611–622 (2010).
- [52] J. Wu, M. Agrawal, H. A. Becerril, Z. Bao, Z. Liu, Y. Chen, and P. Peumans, Organic light-emitting diodes on solution-processed graphene transparent electrodes, *ACS Nano* **4**, 43–48 (2009).
- [53] X. Wang, L. Zhi, and K. Mullen, Transparent, conductive graphene electrodes for dye-sensitized solar cells, *Nano Lett.* **8**, 323–327 (2007).
- [54] L. Gomez De Arco, Y. Zhang, C. W. Schlenker, K. Ryu, M. E. Thompson, and C. Zhou, Continuous, highly flexible, and transparent graphene films by chemical vapor deposition for organic photovoltaics, *ACS Nano* **4**, 2865–2873 (2010).
- [55] K. J. Tielrooij, J. C. W. Song, S. A. Jensen, A. Centeno, A. Pesquera, A. Zurutuza Elorza, M. Bonn, L. S. Levitov, and F. H. L. Koppens, Photoexcitation cascade and multiple hot-carrier generation in graphene, *Nat. Phys.* **9**, 248–252 (2013).
- [56] L. Britnell, R. M. Ribeiro, A. Eckmann, R. Jalil, B. D. Belle, A. Mishchenko, Y.-J. Kim, R. V. Gorbachev, T. Georgiou, S. V. Morozov, A. N. Grigorenko, A. K. Geim, C. Casiraghi, A. H. C. Neto, and K. S. Novoselov, Strong light-matter interactions in heterostructures of atomically thin films, *Science* **340**, 1311–1314 (2013).
- [57] J. M. Dawlaty, S. Shivaraman, J. Strait, P. George, M. Chandrashekar, F. Rana, M. G. Spencer, D. Veksler, and Y. Chen, Measurement of the optical absorption spectra of epitaxial graphene from terahertz to visible, *Appl. Phys. Lett.* **93**, 131905 (2008).
- [58] G. Konstantatos, M. Badioli, L. Gaudreau, J. Osmond, M. Bernechea, F. P. G. de Arquer, F. Gatti, and F. H. L. Koppens, Hybrid graphene-quantum dot phototransistors with ultrahigh gain, *Nat. Nanotechnol.* **7**, 363–368 (2012).
- [59] Y.-M. Lin, C. Dimitrakopoulos, K. A. Jenkins, D. B. Farmer, H.-Y. Chiu, A. Grill, and P. Avouris, 100-GHz transistors from wafer-scale epitaxial graphene, *Science* **327**, 662–662 (2010).
- [60] Y. Wu, Y.-m. Lin, A. A. Bol, K. A. Jenkins, F. Xia, D. B. Farmer, Y. Zhu, and P. Avouris, High-frequency, scaled graphene transistors on diamond-like carbon, *Nature (London)* **472**, 74–78 (2011).
- [61] M. Y. Han, B. Özyilmaz, Y. Zhang, and P. Kim, Energy band-gap engineering of graphene nanoribbons, *Phys. Rev. Lett.* **98**, 206805 (2007).
- [62] X. Liu, J. B. Oostinga, A. F. Morpurgo, and L. M. K. Vandersypen, Electrostatic confinement of electrons in graphene nanoribbons, *Phys. Rev. B* **80**, 121407 (2009).
- [63] J. B. Oostinga, H. B. Heersche, X. Liu, A. F. Morpurgo, and L. M. K. Vandersypen, Gate-induced insulating state in bilayer graphene devices, *Nat. Mater.* **7**, 151–157 (2008).
- [64] D. C. Elias, R. R. Nair, T. M. G. Mohiuddin, S. V. Morozov, P. Blake, M. P. Halsall, A. C. Ferrari, D. W. Boukhvalov, M. I. Katsnelson, A. K. Geim, and K. S. Novoselov, Control of graphene’s properties by reversible hydrogenation: Evidence for graphane, *Science* **323**, 610–613 (2009).

- [65] D. Prasai, J. C. Tuberquia, R. R. Harl, G. K. Jennings, and K. I. Bolotin, Graphene: corrosion-inhibiting coating, *ACS Nano* **6**, 1102–1108 (2012).
- [66] R. J. Young, I. A. Kinloch, L. Gong, and K. S. Novoselov, The mechanics of graphene nanocomposites: A review, *Compos. Sci. Technol.* **72**, 1459–1476 (2012).
- [67] S. Garaj, W. Hubbard, A. Reina, J. Kong, D. Branton, and J. A. Golovchenko, Graphene as a subnanometre trans-electrode membrane, *Nature (London)* **467**, 190–193 (2010).
- [68] C. A. Merchant, K. Healy, M. Wanunu, V. Ray, N. Peterman, J. Bartel, M. D. Fischbein, K. Venta, Z. Luo, A. T. C. Johnson, and M. Drndić, DNA translocation through graphene nanopores, *Nano Lett.* **10**, 2915–2921 (2010).
- [69] F. Schedin, A. K. Geim, S. V. Morozov, E. W. Hill, P. Blake, M. I. Katsnelson, and K. S. Novoselov, Detection of individual gas molecules adsorbed on graphene, *Nat. Mater.* **6**, 652–655 (2007).
- [70] C. Liu, Z. Yu, D. Neff, A. Zhamu, and B. Z. Jang, Graphene-based supercapacitor with an ultrahigh energy density, *Nano Lett.* **10**, 4863–4868 (2010).
- [71] M. F. El-Kady and R. B. Kaner, Scalable fabrication of high-power graphene micro-supercapacitors for flexible and on-chip energy storage, *Nat. Commun.* **4**, 1475 (2013).
- [72] B. Kang and G. Ceder, Battery materials for ultrafast charging and discharging, *Nature (London)* **458**, 190–193 (2009).
- [73] X. Li, W. Cai, J. An, S. Kim, J. Nah, D. Yang, R. Piner, A. Velamakanni, I. Jung, E. Tutuc, S. K. Banerjee, L. Colombo, and R. S. Ruoff, Large-area synthesis of high-quality and uniform graphene films on copper foils, *Science* **324**, 1312–1314 (2009).
- [74] C. Berger, Z. Song, T. Li, X. Li, A. Y. Ogbazghi, R. Feng, Z. Dai, A. N. Marchenkov, E. H. Conrad, P. N. First, and W. A. de Heer, Ultrathin epitaxial graphite: 2d electron gas properties and a route toward graphene-based nanoelectronics, *J. Phys. Chem. B* **108**, 19912–19916 (2004).
- [75] Y. Hernandez, V. Nicolosi, M. Lotya, F. M. Blighe, Z. Sun, S. De, M. T., B. Holland, M. Byrne, Y. K. Gun'Ko, J. J. Boland, P. Niraj, G. Duesberg, S. Krishnamurthy, R. Goodhue, J. Hutchison, V. Scardaci, A. C. Ferrari, and J. N. Coleman, High-yield production of graphene by liquid-phase exfoliation of graphite, *Nat. Nanotechnol.* **3**, 563–568 (2008).
- [76] V. V. Cheianov, V. Fal'ko, and B. L. Altshuler, The focusing of electron flow and a Veselago lens in graphene  $p - n$  junctions, *Science* **315**, 1252–1255 (2007).
- [77] M. I. Katsnelson, K. S. Novoselov, and A. K. Geim, Chiral tunnelling and the Klein paradox in graphene, *Nat. Phys.* **2**, 620–625 (2006).
- [78] C. Kittel, *Introduction to solid state physics*, John Wiley & Sons, Inc., 7th edition, 1996.
- [79] P. R. Wallace, The band theory of graphite, *Phys. Rev.* **71**, 622–634 (1947).
- [80] C. Bena and G. Montambaux, Remarks on the tight-binding model of graphene, *New J. Phys.* **11**, 095003 (2009).
- [81] M. V. Berry, Quantal phase factors accompanying adiabatic changes, *P. Roy. Soc. Lond. A. Mat.* **392**, 45–57 (1984).
- [82] X. Wu, X. Li, Z. Song, C. Berger, and W. A. de Heer, Weak antilocalization in epitaxial graphene: evidence for chiral electrons, *Phys. Rev. Lett.* **98**, 136801 (2007).
- [83] F. V. Tikhonenko, D. W. Horsell, R. V. Gorbachev, and A. K. Savchenko, Weak localization in graphene flakes, *Phys. Rev. Lett.* **100**, 056802 (2008).



- [84] P. Allain and J. Fuchs, Klein tunneling in graphene: optics with massless electrons, *Eur. Phys. J. B* **83**, 301–317 (2011).
- [85] V. G. Veselago, The electrodynamics of substances with simultaneously negative values of  $\epsilon$  and  $\mu$ , *Sov. Phys. Usp.* **10**, 509 (1968).
- [86] J. B. Pendry and D. R. Smith, Reversing light with negative refraction, *Phys. Today* **57**, 37–43 (2004).
- [87] V. V. Cheianov and V. I. Fal'ko, Selective transmission of Dirac electrons and ballistic magnetoresistance of n-p junctions in graphene, *Phys. Rev. B* **74**, 041403 (2006).
- [88] S. Datta, *Electronic transport in mesoscopic systems*, Cambridge University Press, 1997.
- [89] J. N. Fuchs, F. Piéchon, M. O. Goerbig, and G. Montambaux, Topological Berry phase and semiclassical quantization of cyclotron orbits for two dimensional electrons in coupled band models, *Eur. Phys. J. B* **77**, 351–362 (2010).
- [90] V. P. Gusynin and S. G. Sharapov, Unconventional integer quantum Hall effect in graphene, *Phys. Rev. Lett.* **95**, 146801 (2005).
- [91] J. Bardeen, L. N. Cooper, and J. R. Schrieffer, Theory of superconductivity, *Phys. Rev.* **108**, 1175–1204 (1957).
- [92] M. Tinkham, *Introduction to superconductivity*, Dover, New York, 2nd edition, 2004.
- [93] B. Josephson, Possible new effects in superconductive tunnelling, *Phys. Lett.* **1**, 251–253 (1962).
- [94] Y.-J. Doh, J. A. van Dam, A. L. Roest, E. P. A. M. Bakkers, L. P. Kouwenhoven, and S. De Franceschi, Tunable supercurrent through semiconductor nanowires, *Science* **309**, 272–275 (2005).
- [95] P. Jarillo-Herrero, J. A. van Dam, and L. P. Kouwenhoven, Quantum supercurrent transistors in carbon nanotubes, *Nature (London)* **439**, 953–956 (2006).
- [96] H. B. Heersche, P. Jarillo-Herrero, J. B. Oostinga, L. M. K. Vandersypen, and A. F. Morpurgo, Bipolar supercurrent in graphene, *Nature (London)* **446**, 56–59 (2007).
- [97] J. P. Heida, *Josephson currents in two dimensional mesoscopic ballistic conductors*, PhD thesis, University of Groningen, 1998.
- [98] A. F. Andreev, Thermal conductivity of the intermediate state of superconductors, *Sov. Phys.-JETP* **19**, 1228–1231 (1964).
- [99] C. W. J. Beenakker, Specular Andreev reflection in graphene, *Phys. Rev. Lett.* **97**, 067007 (2006).
- [100] C. W. J. Beenakker, Colloquium: Andreev reflection and Klein tunneling in graphene, *Rev. Mod. Phys.* **80**, 1337–1354 (2008).
- [101] G. Wald, Human vision and the spectrum, *Science* **101**, 653–658 (1945).
- [102] F. J. Giessibl, Advances in atomic force microscopy, *Rev. Mod. Phys.* **75**, 949–983 (2003).
- [103] A. C. Ferrari, J. C. Meyer, V. Scardaci, C. Casiraghi, M. Lazzeri, F. Mauri, S. Piscanec, D. Jiang, K. S. Novoselov, S. Roth, and A. K. Geim, Raman spectrum of graphene and graphene layers, *Phys. Rev. Lett.* **97**, 187401 (2006).
- [104] L. Malard, M. Pimenta, G. Dresselhaus, and M. Dresselhaus, Raman spectroscopy in graphene, *Phys. Rep.* **473**, 51–87 (2009).
- [105] A. C. Ferrari and D. M. Basko, Raman spectroscopy as a versatile tool for studying the properties of graphene, *Nat. Nanotechnol.* **8**, 235–246 (2013).

- 
- [106] L. A. Ponomarenko, R. Yang, T. M. Mohiuddin, M. I. Katsnelson, K. S. Novoselov, S. V. Morozov, A. A. Zhukov, F. Schedin, E. W. Hill, and A. K. Geim, Effect of a high- $\kappa$  environment on charge carrier mobility in graphene, *Phys. Rev. Lett.* **102**, 206603 (2009).
- [107] T. O. Wehling, S. Yuan, A. I. Lichtenstein, A. K. Geim, and M. I. Katsnelson, Resonant scattering by realistic impurities in graphene, *Phys. Rev. Lett.* **105**, 056802 (2010).
- [108] Z. Cheng, Q. Zhou, C. Wang, Q. Li, C. Wang, and Y. Fang, Toward intrinsic graphene surfaces: A systematic study on thermal annealing and wet-chemical treatment of SiO<sub>2</sub>-supported graphene devices, *Nano Lett.* **11**, 767–771 (2011).
- [109] W. M. Haynes, editor, *CRC handbook of chemistry and physics, 93rd ed.*, CRC Press, 2012.
- [110] D. Yoon, Y.-W. Son, and H. Cheong, Negative thermal expansion coefficient of graphene measured by raman spectroscopy, *Nano Lett.* **11**, 3227–3231 (2011).
- [111] A. M. Goossens, *Confinement of charge carriers in bilayer graphene*, PhD thesis, Technische Universiteit Delft, 2013.
- [112] S. J. Haigh, A. Gholinia, R. Jalil, S. Romani, L. Britnell, D. C. Elias, K. S. Novoselov, L. A. Ponomarenko, A. K. Geim, and R. Gorbachev, Cross-sectional imaging of individual layers and buried interfaces of graphene-based heterostructures and superlattices, *Nat. Mater.* **11**, 764–767 (2012).
- [113] R. S. Paese, An x-ray study of boron nitride, *Acta Cryst.* **5**, 356 (1952).
- [114] W. Pan, J. Xiao, J. Zhu, C. Yu, G. Zhang, Z. Ni, K. Watanabe, T. Taniguchi, Y. Shi, and X. Wang, Biaxial compressive strain engineering in graphene/boron nitride heterostructures, *Sci. Rep.* **2**, 893 (2012).
- [115] C. W. J. Beenakker, Theory of Coulomb-blockade oscillations in the conductance of a quantum dot, *Phys. Rev. B* **44**, 1646–1656 (1991).
- [116] R. J. Jackman, J. L. Wilbur, and G. M. Whitesides, Fabrication of submicrometer features on curved substrates by microcontact printing, *Science* **269**, 664–666 (1995).
- [117] J.-H. Ahn, H.-S. Kim, K. J. Lee, S. Jeon, S. J. Kang, Y. Sun, R. G. Nuzzo, and J. A. Rogers, Heterogeneous three-dimensional electronics by use of printed semiconductor nanomaterials, *Science* **314**, 1754–1757 (2006).
- [118] E. J. Smythe, M. D. Dickey, G. M. Whitesides, and F. Capasso, A technique to transfer metallic nanoscale patterns to small and non-planar surfaces, *ACS Nano* **3**, 59–65 (2009).
- [119] B. D. Gates, Q. Xu, M. Stewart, D. Ryan, C. G. Willson, and G. M. Whitesides, New approaches to nanofabrication: molding, printing, and other techniques, *Chem. Rev.* **105**, 1171–1196 (2005).
- [120] M. J. Allen, V. C. Tung, L. Gomez, Z. Xu, L.-M. Chen, K. S. Nelson, C. Zhou, R. B. Kaner, and Y. Yang, Soft transfer printing of chemically converted graphene, *Adv. Mater.* **21**, 2098–2102 (2009).
- [121] D. Li, W. Windl, and N. P. Padture, Toward site-specific stamping of graphene, *Adv. Mater.* **21**, 1243–1246 (2009).
- [122] X. Liang, Z. Fu, and S. Y. Chou, Graphene transistors fabricated via transfer-printing in device active-areas on large wafer, *Nano Lett.* **7**, 3840–3844 (2007).
- [123] M. Meitl, Z. Zhu, V. Kumar, K. Lee, X. Feng, Y. Huang, I. Adesida, R. Nuzzo, and J. Rogers, Transfer printing by kinetic control of adhesion to an elastomeric stamp, *Nat. Mater.* **5**, 33–38 (2006).

- [124] A. Reina, H. Son, L. Jiao, B. Fan, M. S. Dresselhaus, Z. Liu, and J. Kong, Transferring and identification of single- and few-layer graphene on arbitrary substrates, *J. Phys. Chem. C* **112**, 17741–17744 (2008).
- [125] Y. Lee, S. Bae, H. Jang, S. Jang, S.-E. Zhu, S. H. Sim, Y. I. Song, B. H. Hong, and J.-H. Ahn, Wafer-scale synthesis and transfer of graphene films, *Nano Lett.* **10**, 490–493 (2010).
- [126] L. De Arco, Y. Zhang, A. Kumar, and C. Zhou, Synthesis, transfer, and devices of single- and few-layer graphene by chemical vapor deposition, *IEEE T. Nanotechnol.* **8**, 135–138 (2009).
- [127] A. Reina, X. Jia, J. Ho, D. Nezich, H. Son, V. Bulovic, M. S. Dresselhaus, and J. Kong, Large area, few-layer graphene films on arbitrary substrates by chemical vapor deposition, *Nano Lett.* **9**, 30–35 (2009).
- [128] L. Jiao, B. Fan, X. Xian, Z. Wu, J. Zhang, and Z. Liu, Creation of nanostructures with poly(methyl methacrylate)-mediated nanotransfer printing, *J. Am. Chem. Soc.* **130**, 12612–12613 (2008).
- [129] E. A. Weiss, G. K. Kaufman, J. K. Kriebel, Z. Li, R. Schalek, and G. M. Whitesides, Si/SiO<sub>2</sub>-templated formation of ultraflat metal surfaces on glass, polymer, and solder supports: their use as substrates for self-assembled monolayers, *Langmuir* **23**, 9686–9694 (2007).
- [130] L. Song, L. Ci, W. Gao, and P. M. Ajayan, Transfer printing of graphene using gold film, *ACS Nano* **3**, 1353–1356 (2009).
- [131] H. Tabata, M. Shimizu, and K. Ishibashi, Fabrication of single electron transistors using transfer-printed aligned single walled carbon nanotubes arrays, *Appl. Phys. Lett.* **95**, 113107 (2009).
- [132] K. A. Dill, T. M. Truskett, V. Vlachy, and B. Hribar-Lee, Modeling water, the hydrophobic effect and ion solvation, *Annu. Rev. Bioph. Biom.* **34**, 173–199 (2005).
- [133] N. T. Southall, K. A. Dill, and A. D. J. Haymet, A view of the hydrophobic effect, *J. Phys. Chem. B* **106**, 521–533 (2002).
- [134] M. O. Jensen, O. G. Mouritsen, and G. H. Peters, The hydrophobic effect: Molecular dynamics simulations of water confined between extended hydrophobic and hydrophilic surfaces, *J. Chem. Phys.* **120**, 9729–9744 (2004).
- [135] J. Janeček and R. R. Netz, Interfacial water at hydrophobic and hydrophilic surfaces: Depletion versus adsorption, *Langmuir* **23**, 8417–8429 (2007).
- [136] H. Zandbergen, A. Pruyboom, and G. V. Tendeloo, Highly temperature-stable Si<sub>3</sub>N<sub>4</sub> perforated grids, *Ultramicroscopy* **24**, 45–48 (1988).
- [137] J. C. Meyer, A. K. Geim, M. I. Katsnelson, K. S. Novoselov, T. J. Booth, and S. Roth, The structure of suspended graphene sheets, *Nature (London)* **446**, 60–63 (2007).
- [138] M. J. Allen, V. C. Tung, and R. B. Kaner, Honeycomb carbon: a review of graphene, *Chem. Rev.* **110**, 132–145 (2009).
- [139] C. Rao, A. Sood, K. Subrahmanyam, and A. Govindaraj, Graphene: the new two-dimensional nanomaterial, *Angew. Chem. Int. Ed.* **48**, 7752–7777 (2009).
- [140] c. O. Girit, J. C. Meyer, R. Erni, M. D. Rossell, C. Kisielowski, L. Yang, C.-H. Park, M. F. Crommie, M. L. Cohen, S. G. Louie, and A. Zettl, Graphene at the edge: Stability and dynamics, *Science* **323**, 1705–1708 (2009).
- [141] J. C. Love, L. A. Estroff, J. K. Kriebel, R. G. Nuzzo, and G. M. Whitesides, Self-assembled monolayers of thiolates on metals as a form of nanotechnology, *Chem. Rev.* **105**, 1103–1170 (2005).

- 
- [142] W. A. de Heer, C. Berger, X. Wu, P. N. First, E. H. Conrad, X. Li, T. Li, M. Sprinkle, J. Hass, M. L. Sadowski, M. Potemski, and G. Martinez, Epitaxial graphene, *Solid State Commun.* **143**, 92 – 100 (2007).
- [143] A. Fasolino, J. H. Los, and M. I. Katsnelson, Intrinsic ripples in graphene, *Nat. Mater.* **6**, 858–861 (2007).
- [144] F. Guinea, B. Horowitz, and P. Le Doussal, Gauge field induced by ripples in graphene, *Phys. Rev. B* **77**, 205421 (2008).
- [145] V. M. Pereira, A. H. Castro Neto, H. Y. Liang, and L. Mahadevan, Geometry, mechanics, and electronics of singular structures and wrinkles in graphene, *Phys. Rev. Lett.* **105**, 156603 (2010).
- [146] N. Levy, S. A. Burke, K. L. Meaker, M. Panlasigui, A. Zettl, F. Guinea, A. H. C. Neto, and M. F. Crommie, Strain-induced pseudomagnetic fields greater than 300 tesla in graphene nanobubbles, *Science* **329**, 544–547 (2010).
- [147] R. Balog, B. Jorgensen, L. Nilsson, M. Andersen, E. Rienks, M. Bianchi, M. Fanetti, E. Laegsgaard, A. Baraldi, S. Lizzit, Z. Sljivancanin, F. Besenbacher, B. Hammer, T. G. Pedersen, P. Hofmann, and L. Hornekaer, Bandgap opening in graphene induced by patterned hydrogen adsorption, *Nat. Mater.* **9**, 315–319 (2010).
- [148] T. Georgiou, L. Britnell, P. Blake, R. V. Gorbachev, A. Gholinia, A. K. Geim, C. Casiraghi, and K. S. Novoselov, Graphene bubbles with controllable curvature, *Appl. Phys. Lett.* **99**, 093103 (2011).
- [149] C. Y. Wang, K. Mylvaganam, and L. C. Zhang, Wrinkling of monolayer graphene: A study by molecular dynamics and continuum plate theory, *Phys. Rev. B* **80**, 155445 (2009).
- [150] A. J. Gil, S. Adhikari, F. Scarpa, and J. Bonet, The formation of wrinkles in single-layer graphene sheets under nanoindentation, *J. Phys.: Condens. Matter* **22**, 145302 (2010).
- [151] W. H. Duan, K. Gong, and Q. Wang, Controlling the formation of wrinkles in a single layer graphene sheet subjected to in-plane shear, *Carbon* **49**, 3107–3112 (2011).
- [152] K. Min and N. R. Aluru, Mechanical properties of graphene under shear deformation, *Appl. Phys. Lett.* **98**, 013113 (2011).
- [153] N. Liu, Z. Pan, L. Fu, C. Zhang, B. Dai, and Z. Liu, The origin of wrinkles on transferred graphene, *Nano Res.* **4**, 996–1004 (2011).
- [154] G.-X. Ni, Y. Zheng, S. Bae, H. R. Kim, A. Pachoud, Y. S. Kim, C.-L. Tan, D. Im, J.-H. Ahn, B. H. Hong, and B. zylmaz, Quasi-periodic nanoripples in graphene grown by chemical vapor deposition and its impact on charge transport, *ACS Nano* **6**, 1158–1164 (2012).
- [155] L. Gao, W. Ren, H. Xu, L. Jin, Z. Wang, T. Ma, L.-P. Ma, Z. Zhang, Q. Fu, L.-M. Peng, X. Bao, and H.-M. Cheng, Repeated growth and bubbling transfer of graphene with millimetre-size single-crystal grains using platinum, *Nat. Commun.* **3**, 699 (2012).
- [156] W. Zhu, T. Low, V. Perebeinos, A. A. Bol, Y. Zhu, H. Yan, J. Tersoff, and P. Avouris, Structure and electronic transport in graphene wrinkles, *Nano Lett.* **12**, 3431–3436 (2012).
- [157] M. Ishigami, J. H. Chen, W. G. Cullen, M. S. Fuhrer, and E. D. Williams, Atomic structure of graphene on SiO<sub>2</sub>, *Nano Lett.* **7**, 1643–1648 (2007).
- [158] K. Xu, P. Cao, and J. R. Heath, Scanning tunneling microscopy characterization of the electrical properties of wrinkles in exfoliated graphene monolayers, *Nano Lett.* **9**, 4446–4451 (2009).
- [159] G. F. Schneider, V. E. Calado, H. Zandbergen, L. M. K. Vandersypen, and C. Dekker, Wedging transfer of nanostructures, *Nano Lett.* **10**, 1912–1916 (2010).

- [160] F. Guinea, M. I. Katsnelson, and M. A. H. Vozmediano, Midgap states and charge inhomogeneities in corrugated graphene, *Phys. Rev. B* **77**, 075422 (2008).
- [161] R. R. Nair, W. Ren, R. Jalil, I. Riaz, V. G. Kravets, L. Britnell, P. Blake, F. Schedin, A. S. Mayorov, S. Yuan, M. I. Katsnelson, H.-M. Cheng, W. Strupinski, L. G. Bulusheva, A. V. Okotrub, I. V. Grigorieva, A. N. Grigorenko, K. S. Novoselov, and A. K. Geim, Fluorinated graphene: fluorographene: a two-dimensional counterpart of teflon, *Small* **6**, 2773–2773 (2010).
- [162] D. Branton, D. W. Deamer, A. Marziali, H. Bayley, S. A. Benner, T. Butler, M. Di Ventra, S. Garaj, A. Hibbs, X. Huang, S. B. Jovanovich, P. S. Krstic, S. Lindsay, X. S. Ling, C. H. Mastrangelo, A. Meller, J. S. Oliver, Y. V. Pershin, J. M. Ramsey, R. Riehn, G. V. Soni, V. Tabard-Cossa, M. Wanunu, M. Wiggin, and J. A. Schloss, The potential and challenges of nanopore sequencing, *Nat. Biotechnol.* **26**, 1146–1153 (2008).
- [163] C. Dekker, Solid-state nanopores, *Nat. Nanotechnol.* **2**, 209–215 (2007).
- [164] L. Ma and S. L. Cockroft, Biological nanopores for single-molecule biophysics, *ChemBioChem* **11**, 25–34 (2010).
- [165] J. Li, M. Gershow, D. Stein, E. Brandin, and J. A. Golovchenko, DNA molecules and configurations in a solid-state nanopore microscope, *Nat. Mater.* **2**, 611–615 (2003).
- [166] A. J. Storm, C. Storm, J. Chen, H. Zandbergen, J.-F. Joanny, and C. Dekker, Fast DNA translocation through a solid-state nanopore, *Nano Lett.* **5**, 1193–1197 (2005).
- [167] G. M. Skinner, M. van den Hout, O. Broekmans, C. Dekker, and N. H. Dekker, Distinguishing single- and double-stranded nucleic acid molecules using solid-state nanopores, *Nano Lett.* **9**, 2953–2960 (2009).
- [168] M. Wanunu, J. Sutin, and A. Meller, DNA profiling using solid-state nanopores: detection of DNA-binding molecules, *Nano Lett.* **9**, 3498–3502 (2009).
- [169] S. W. Kowalczyk, A. R. Hall, and C. Dekker, Detection of local protein structures along DNA using solid-state nanopores, *Nano Lett.* **10**, 324–328 (2009).
- [170] M. D. Fischbein and M. Drndic, Electron beam nanosculpting of suspended graphene sheets, *Appl. Phys. Lett.* **93**, 113107 (2008).
- [171] G. Tsoukleri, J. Parthenios, K. Papagelis, R. Jalil, A. C. Ferrari, A. K. Geim, K. S. Novoselov, and C. Galotis, Subjecting a graphene monolayer to tension and compression, *Small* **5**, 2397–2402 (2009).
- [172] A. H. Castro Neto, F. Guinea, N. M. R. Peres, K. S. Novoselov, and A. K. Geim, The electronic properties of graphene, *Rev. Mod. Phys.* **81**, 109–162 (2009).
- [173] H. W. C. Postma, Rapid sequencing of individual DNA molecules in graphene nanogaps, *Nano Lett.* **10**, 420–425 (2010).
- [174] A. Hashimoto, K. Suenaga, A. Gloter, K. Urita, and S. Iijima, Direct evidence for atomic defects in graphene layers, *Nature (London)* **430**, 870–873 (2004).
- [175] I. Heller, S. Chatoor, J. Mannik, M. A. G. Zevenbergen, J. B. Oostinga, A. F. Morpurgo, C. Dekker, and S. G. Lemay, Charge noise in graphene transistors, *Nano Lett.* **10**, 1563–1567 (2010).
- [176] S. W. Kowalczyk, A. Y. Grosberg, Y. Rabin, and C. Dekker, Modeling the conductance and DNA blockade of solid-state nanopores, *Nanotechnology* **22**, 315101 (2011).
- [177] G. F. Schneider, S. W. Kowalczyk, V. E. Calado, G. Pandraud, H. W. Zandbergen, L. M. K. Vandersypen, and C. Dekker, DNA translocation through graphene nanopores, *Nano Lett.* **10**, 3163–3167 (2010).

- 
- [178] G. F. Schneider, Xu, S. Hage, S. Luik, J. Spoor, S. Malladi, H. Zandbergen, and C. Dekker, Tailoring the hydrophobicity of graphene nanopores, Accepted in *Nat. Comm.* (2013).
- [179] M.-Y. Wu, R. M. M. Smeets, M. Zandbergen, U. Ziese, D. Krapf, P. E. Batson, N. H. Dekker, C. Dekker, and H. W. Zandbergen, Control of shape and material composition of solid-state nanopores, *Nano Lett.* **9**, 479–484 (2008).
- [180] U. F. Keyser, B. N. Koeleman, S. van Dorp, D. Krapf, R. M. M. Smeets, S. G. Lemay, N. H. Dekker, and C. Dekker, Direct force measurements on DNA in a solid-state nanopore, *Nat. Phys.* **2**, 473–477 (2006).
- [181] D. Krapf, M.-Y. Wu, R. M. M. Smeets, H. W. Zandbergen, C. Dekker, and S. G. Lemay, Fabrication and characterization of nanopore-based electrodes with radii down to 2 nm, *Nano Lett.* **6**, 105–109 (2005).
- [182] S.-L. Xu, S.-X. Yin, H.-P. Liang, C. Wang, L.-J. Wan, and C.-L. Bai, Identification of the preferential-bonding effect of disubstituted alkane derivatives using scanning tunneling microscopy, *J. Phys. Chem. B* **108**, 620–624 (2003).
- [183] F. Miao, S. Wijeratne, Y. Zhang, U. C. Coskun, W. Bao, and C. N. Lau, Phase-coherent transport in graphene quantum billiards., *Science* **317**, 1530–1533 (2007).
- [184] A. Shailos, W. Nativel, A. Kasumov, C. Collet, M. Ferrier, S. Guron, R. Deblock, and H. Bouchiat, Proximity effect and multiple Andreev reflections in few-layer graphene, *Europhys. Lett.* **79**, 57008 (2007).
- [185] X. Du, I. Skachko, and E. Y. Andrei, Josephson current and multiple Andreev reflections in graphene SNS junctions, *Phys. Rev. B* **77**, 184507 (2008).
- [186] T. Dirks, T. L. Hughes, S. Lal, B. Uchoa, Y.-F. Chen, C. Chialvo, P. M. Goldbart, and N. Mason, Transport through Andreev bound states in a graphene quantum dot, *Nat. Phys.* **7**, 386–390 (2011).
- [187] I. V. Borzenets, U. C. Coskun, S. J. Jones, and G. Finkelstein, Phase diffusion in graphene-based Josephson junctions, *Phys. Rev. Lett.* **107**, 137005 (2011).
- [188] G.-H. Lee, D. Jeong, J.-H. Choi, Y.-J. Doh, and H.-J. Lee, Electrically tunable macroscopic quantum tunneling in a graphene-based Josephson junction, *Phys. Rev. Lett.* **107**, 146605 (2011).
- [189] B. M. Kessler, C. O. Girit, A. Zettl, and V. Bouchiat, Tunable superconducting phase transition in metal-decorated graphene sheets, *Phys. Rev. Lett.* **104**, 047001 (2010).
- [190] V. B. A. Allain, Z. Han, Gate-tunable superconducting-metal-insulating transition in tin-decorated graphene, [arXiv:1109.6910v2](https://arxiv.org/abs/1109.6910v2) [*cond-mat*] (2011).
- [191] F. Miao, W. Bao, H. Zhang, and C. N. Lau, Premature switching in graphene Josephson transistors, *Solid State Commun.* **149**, 1046 – 1049 (2009).
- [192] C. Girit, V. Bouchiat, O. Naaman, Y. Zhang, M. F. Crommie, A. Zettl, and I. Siddiqi, Tunable graphene dc superconducting quantum interference device, *Nano Lett.* **9**, 198–199 (2009).
- [193] C. Chialvo, I. C. Moraru, D. J. V. Harlingen, and N. Mason, Current-phase relation of graphene Josephson junctions, [arXiv:1005.2630](https://arxiv.org/abs/1005.2630) [*cond-mat*] (2010).
- [194] J. Trbovic, N. Minder, F. Freitag, and C. Schenberger, Superconductivity-enhanced conductance fluctuations in few-layer graphene, *Nanotechnology* **21**, 274005 (2010).
- [195] A. Kanda, T. Sato, H. Goto, H. Tomori, S. Takana, Y. Ootuka, and K. Tsukagoshi, Dependence of proximity-induced supercurrent on junction length in multilayer-graphene Josephson junctions, *Phys. C (Amsterdam, Neth.)* **470**, 1477 – 1480 (2010).

- [196] J.-H. Choi, H.-J. Lee, and Y.-J. Doh, Above-gap conductance anomaly studied in superconductor-graphene-superconductor Josephson junctions, *J. Korean Phys. Soc.* **57**, 149 (2010).
- [197] C. Ojeda-Aristizabal, M. Ferrier, S. Guéron, and H. Bouchiat, Tuning the proximity effect in a superconductor-graphene-superconductor junction, *Phys. Rev. B* **79**, 165436 (2009).
- [198] U. C. Coskun, M. Brenner, T. Hymel, V. Vakaryuk, A. Levchenko, and A. Bezryadin, Distribution of supercurrent switching in graphene under proximity effect, *Phys. Rev. Lett.* **108**, 097003 (2012).
- [199] M. Ma and A. Y. Zyuzin, Josephson effect in the quantum Hall regime, *Europhys. Lett.* **21**, 941 (1993).
- [200] N. M. Chtchelkatchev and I. S. Burmistrov, Conductance oscillations with magnetic field of a two-dimensional electron gas - superconductor junction, *Phys. Rev. B* **75**, 214510 (2007).
- [201] I. M. Khaymovich, N. M. Chtchelkatchev, I. A. Shereshevskii, and A. S. Mel'nikov, Andreev transport in two-dimensional normal-superconducting systems in strong magnetic fields, *Europhys. Lett.* **91**, 17005 (2010).
- [202] M. Stone and Y. Lin, Josephson currents in quantum Hall devices, *Phys. Rev. B* **83**, 224501 (2011).
- [203] J. A. M. van Ostaay, A. R. Akhmerov, and C. W. J. Beenakker, Spin-triplet supercurrent carried by quantum Hall edge states through a Josephson junction, *Phys. Rev. B* **83**, 195441 (2011).
- [204] K. Komatsu, C. Li, S. Autier-Laurent, H. Bouchiat, and S. Gueron, Superconducting proximity effect through graphene from zero field to the Quantum Hall regime, *Phys. Rev. B* **86**, 115412 (2012).
- [205] B. J. van Wees, P. de Vries, P. Magnée, and T. M. Klapwijk, Excess conductance of superconductor-semiconductor interfaces due to phase conjugation between electrons and holes, *Phys. Rev. Lett.* **69**, 510–513 (1992).
- [206] I. K. Marmoros, C. W. J. Beenakker, and R. A. Jalabert, Three signatures of phase-coherent Andreev reflection, *Phys. Rev. B* **48**, 2811–2814 (1993).
- [207] F. Giazotto, P. Pingue, F. Beltram, M. Lazzarino, D. Orani, S. Rubini, and A. Franciosi, Resonant transport in Nb/GaAs/AlGaAs heterostructures: realization of the de Gennes-Saint-James model, *Phys. Rev. Lett.* **87**, 216808 (2001).
- [208] N. N. Iosad, B. D. Jackson, F. Ferro, J. R. Gao, S. N. Polyakov, P. N. Dmitriev, and T. M. Klapwijk, Source optimization for magnetron sputter-deposition of NbTiN tuning elements for SIS THz detectors, *Supercond. Sci. Technol.* **12**, 736 (1999).
- [209] N. N. Iosad, A. V. Mijiritskii, V. V. Roddatis, N. M. van der Pers, B. D. Jackson, J. R. Gao, S. N. Polyakov, P. N. Dmitriev, and T. M. Klapwijk, Properties of  $(\text{Nb}_{0.35}, \text{Ti}_{0.15})_x\text{N}_{1-x}$  thin films deposited on silicon wafers at ambient substrate temperature, *J. Appl. Phys.* **88**, 5756–5759 (2000).
- [210] N. Iosad, *Metal nitrides for superconducting tunnel detectors*, PhD thesis, Technische Universiteit Delft, 2002.
- [211] A. Barreiro, M. Lazzeri, J. Moser, F. Mauri, and A. Bachtold, Transport properties of graphene in the high-current limit, *Phys. Rev. Lett.* **103**, 076601 (2009).
- [212] N. Vandecasteele, A. Barreiro, M. Lazzeri, A. Bachtold, and F. Mauri, Current-voltage characteristics of graphene devices: Interplay between Zener-Klein tunneling and defects, *Phys. Rev. B* **82**, 045416 (2010).

- [213] V. Perebeinos and P. Avouris, Inelastic scattering and current saturation in graphene, *Phys. Rev. B* **81**, 195442 (2010).
- [214] R. R. Nair, M. Sepioni, I.-L. Tsai, O. Lehtinen, J. Keinonen, A. V. Krasheninnikov, T. Thomson, A. K. Geim, and I. V. Grigorieva, Spin-half paramagnetism in graphene induced by point defects, *Nat. Phys.* **8**, 199–202 (2012).
- [215] A. V. Balatsky, I. Vekhter, and J.-X. Zhu, Impurity-induced states in conventional and unconventional superconductors, *Rev. Mod. Phys.* **78**, 373–433 (2006).
- [216] X. L. Liu, *Quantum dots and Andreev reflections in graphene*, PhD thesis, Technische Universiteit Delft, 2010.
- [217] M. T. Levinsen, Cavity self-induced step for a Dayem bridge, *Appl. Phys. Lett.* **24**, 247–249 (1974).
- [218] T. M. Klapwijk, M. Sepers, and J. E. Mooij, Regimes in the behavior of superconducting microbridges, *J. Low Temp. Phys.* **27**, 801–835 (1977).
- [219] S. Sasaki, M. Kriener, K. Segawa, K. Yada, Y. Tanaka, M. Sato, and Y. Ando, Topological superconductivity in  $\text{Cu}_x\text{Bi}_2\text{Se}_3$ , *Phys. Rev. Lett.* **107**, 217001 (2011).
- [220] M. S. Fuhrer, C. N. Lau, and A. H. MacDonald, Graphene: Materially better carbon, *MRS Bull.* **35**, 289–295 (2010).
- [221] Y. Dan, Y. Lu, N. J. Kybert, Z. Luo, and A. T. C. Johnson, Intrinsic response of graphene vapor sensors, *Nano Lett.* **9**, 1472–1475 (2009).
- [222] J. Chen, C. Jang, S. Adam, M. S. Fuhrer, E. D. Williams, and M. Ishigami, Charged-impurity scattering in graphene, *Nat. Phys.* **4**, 377–381 (2008).
- [223] Y. Zhang, T. Tang, C. Girit, Z. Hao, M. C. Martin, A. Zettl, M. F. Crommie, Y. R. Shen, and F. Wang, Direct observation of a widely tunable bandgap in bilayer graphene, *Nature (London)* **459**, 820–823 (2009).
- [224] B. E. Feldman, J. Martin, and A. Yacoby, Broken-symmetry states and divergent resistance in suspended bilayer graphene, *Nat. Phys.* **5**, 889–893 (2009).
- [225] A. S. Mayorov, D. C. Elias, M. Mucha-Kruczynski, R. V. Gorbachev, T. Tudorovskiy, A. Zhukov, S. V. Morozov, M. I. Katsnelson, V. I. Falko, A. K. Geim, and K. S. Novoselov, Interaction-driven spectrum reconstruction in bilayer graphene, *Science* **333**, 860–863 (2011).
- [226] R. Jalilian, L. A. Jauregui, G. Lopez, J. Tian, C. Roecker, M. M. Yazdanpanah, R. W. Cohn, I. Jovanovic, and Y. P. Chen, Scanning gate microscopy on graphene: Charge inhomogeneity and extrinsic doping, *Nanotechnology* **22**, 295705 (2011).
- [227] A. Castellanos-Gomez, N. Agrat, and G. Rubio-Bollinger, Carbon fibre tips for scanning probe microscopy based on quartz tuning fork force sensors, *Nanotechnology* **21**, 145702 (2010).
- [228] Y. Hirayama, T. Saku, S. Tarucha, and Y. Horikoshi, Ballistic electron transport in macroscopic four-terminal square structures with high mobility, *Appl. Phys. Lett.* **58**, 2672–2674 (1991).
- [229] H. van Houten, C. W. J. Beenakker, J. G. Williamson, M. E. I. Broekaart, P. H. M. van Loosdrecht, B. J. van Wees, J. E. Mooij, C. T. Foxon, and J. J. Harris, Coherent electron focusing with quantum point contacts in a two-dimensional electron gas, *Phys. Rev. B* **39**, 8556–8575 (1989).
- [230] T. Kobayashi, M. Bando, N. Kimura, K. Shimizu, K. Kadono, N. Umezu, K. Miyahara, S. Hayazaki, S. Nagai, Y. Mizuguchi, Y. Murakami, and D. Hobarra, Production of a 100-m-long high-quality graphene transparent conductive film by roll-to-roll chemical vapor deposition and transfer process, *Appl. Phys. Lett.* **102**, 023112 (2013).



- [231] X. Li, C. W. Magnuson, A. Venugopal, R. M. Tromp, J. B. Hannon, E. M. Vogel, L. Colombo, and R. S. Ruoff, Large-area graphene single crystals grown by low-pressure chemical vapor deposition of methane on copper, *J. Am. Chem. Soc.* **133**, 2816–2819 (2011).
- [232] Z. Yan, J. Lin, Z. Peng, Z. Sun, Y. Zhu, L. Li, C. Xiang, E. L. Samuel, C. Kittrell, and J. M. Tour, Toward the synthesis of wafer-scale single-crystal graphene on copper foils, *ACS Nano* **6**, 9110–9117 (2012).
- [233] Y. A. Wu, Y. Fan, S. Speller, G. L. Creeth, J. T. Sadowski, K. He, A. W. Robertson, C. S. Allen, and J. H. Warner, Large single crystals of graphene on melted copper using chemical vapor deposition, *ACS Nano* **6**, 5010–5017 (2012).
- [234] N. Petrone, C. R. Dean, I. Meric, A. M. van der Zande, P. Y. Huang, L. Wang, D. Muller, K. L. Shepard, and J. Hone, Chemical vapor deposition-derived graphene with electrical performance of exfoliated graphene, *Nano Lett.* **12**, 2751–2756 (2012).
- [235] W. Gannett, W. Regan, K. Watanabe, T. Taniguchi, M. F. Crommie, and A. Zettl, Boron nitride substrates for high mobility chemical vapor deposited graphene, *Appl. Phys. Lett.* **98**, 242105 (2011).
- [236] Q. Yu, L. A. Jauregui, W. Wu, R. Colby, J. Tian, Z. Su, H. Cao, Z. Liu, D. Pandey, D. Wei, T. F. Chung, P. Peng, N. P. Guisinger, E. A. Stach, J. Bao, S.-S. Pei, and Y. P. Chen, Control and characterization of individual grains and grain boundaries in graphene grown by chemical vapour deposition, *Nat. Mater.* **10**, 443–449 (2011).
- [237] J. C. Koepke, J. D. Wood, D. Estrada, Z.-Y. Ong, K. T. He, E. Pop, and J. W. Lyding, Atomic-scale evidence for potential barriers and strong carrier scattering at graphene grain boundaries: a scanning tunneling microscopy study, *ACS Nano* **7**(1), 75–86 (2012).
- [238] X. Li, C. W. Magnuson, A. Venugopal, J. An, J. W. Suk, B. Han, M. Borysiak, W. Cai, A. Velamakanni, Y. Zhu, L. Fu, E. M. Vogel, E. Voelkl, L. Colombo, and R. S. Ruoff, Graphene films with large domain size by a two-step chemical vapor deposition process, *Nano Lett.* **10**, 4328–4334 (2010).
- [239] O. V. Yazyev and S. G. Louie, Electronic transport in polycrystalline graphene, *Nat. Mater.* **9**, 806–809 (2010).
- [240] S. Adam, E. H. Hwang, V. M. Galitski, and S. Das Sarma, A self-consistent theory for graphene transport, *P. Natl. A. Sci. USA* **104**, 18392–18397 (2007).
- [241] E. H. Hwang, S. Adam, and S. Das Sarma, Carrier transport in two-dimensional graphene layers, *Phys. Rev. Lett.* **98**, 186806 (2007).
- [242] B. Song, G. F. Schneider, Q. Xu, G. Pandraud, C. Dekker, and H. Zandbergen, Atomic-scale electron-beam sculpting of near-defect-free graphene nanostructures, *Nano Lett.* **11**, 2247–2250 (2011).
- [243] T. Taniguchi and K. Watanabe, Synthesis of high-purity boron nitride single crystals under high pressure by using Ba-BN solvent, *J. Cryst. Growth* **303**, 525–529 (2007).
- [244] D. C. Elias, R. V. Gorbachev, A. S. Mayorov, S. V. Morozov, A. A. Zhukov, P. Blake, L. A. Ponomarenko, I. V. Grigorieva, K. S. Novoselov, F. Guinea, and A. K. Geim, Dirac cones reshaped by interaction effects in suspended graphene, *Nat. Phys.* **7**, 701–704 (2011).
- [245] K. K. Saha, M. Drndić, and B. K. Nikolić, DNA base-specific modulation of microampere transverse edge currents through a metallic graphene nanoribbon with a nanopore, *Nano Lett.* **12**, 50–55 (2011).
- [246] P. Rickhaus, M. Weiss, L. Marot, and C. Schönenberger, Quantum Hall effect in graphene with superconducting electrodes, *Nano Lett.* **12**, 1942–1945 (2012).

- [247] S. Sutar, E. S. Comfort, J. Liu, T. Taniguchi, K. Watanabe, and J. U. Lee, Angle-dependent carrier transmission in graphene  $p-n$  junctions, *Nano Lett.* **12**, 4460–4464 (2012).
- [248] A. L. Grushina, D.-K. Ki, and A. F. Morpurgo, A ballistic  $p-n$  junction in suspended graphene with split bottom gates, *Appl. Phys. Lett.* **102**, 223102 (2013).
- [249] P. Rickhaus, R. Maurand, M.-H. Liu, M. Weiss, K. Richter, and C. Schönberger, Ballistic interferences in suspended graphene., [arXiv:1304.6590 \[cond-mat\]](https://arxiv.org/abs/1304.6590) (2013).
- [250] J. Xue, J. Sanchez-Yamagishi, D. Bulmash, P. Jacquod, A. Deshpande, K. Watanabe, T. Taniguchi, P. Jarillo-Herrero, and B. J. LeRoy, Scanning tunnelling microscopy and spectroscopy of ultra-flat graphene on hexagonal boron nitride, *Nat. Mater.* **10**, 282–285 (2011).
- [251] R. V. Gorbachev, A. S. Mayorov, A. K. Savchenko, D. W. Horsell, and F. Guinea, Conductance of  $p-n-p$  graphene structures with air-bridge top gates, *Nano Lett.* **8**, 1995–1999 (2008).
- [252] N. Stander, B. Huard, and D. Goldhaber-Gordon, Evidence for Klein tunneling in graphene  $p-n$  junctions, *Phys. Rev. Lett.* **102**, 026807 (2009).
- [253] A. F. Young and P. Kim, Quantum interference and Klein tunnelling in graphene heterojunctions, *Nat. Phys.* **5**, 222–226 (2009).
- [254] E. McCann, Asymmetry gap in the electronic band structure of bilayer graphene, *Phys. Rev. B* **74**, 161403 (2006).
- [255] J. M. B. LopesdosSantos, N. M. R. Peres, and A. H. CastroNeto, Graphene bilayer with a twist: electronic structure, *Phys. Rev. Lett.* **99**, 256802 (2007).
- [256] I. Martin, Y. M. Blanter, and A. F. Morpurgo, Topological confinement in bilayer graphene, *Phys. Rev. Lett.* **100**, 036804 (2008).
- [257] P. San-Jose and E. Prada, Helical networks in twisted graphene bilayers under interlayer bias, [arXiv:1304.5344 \[cond-mat\]](https://arxiv.org/abs/1304.5344) (2013).
- [258] K. S. Kim, A. L. Walter, L. Moreschini, T. Seyller, K. Horn, E. Rotenberg, and A. Bostwick, Coexisting massive and massless Dirac fermions in symmetry-broken bilayer graphene, *Nat. Mater.*, pre-print available at <http://dx.doi.org/10.1038/nmat3717> (2013).
- [259] Z. F. Wang, F. Liu, and M. Y. Chou, Fractal Landau-level spectra in twisted bilayer graphene, *Nano Lett.* **12**, 3833–3838 (2012).
- [260] G. Li, A. Luican, J. M. B. Lopes dos Santos, A. H. Castro Neto, A. Reina, J. Kong, and E. Y. Andrei, Observation of Van Hove singularities in twisted graphene layers, *Nat. Phys.* **6**, 109–113 (2010).
- [261] R. Nandkishore, L. S. Levitov, and A. V. Chubukov, Chiral superconductivity from repulsive interactions in doped graphene, *Nat. Phys.* **8**, 158–163 (2012).
- [262] J. D. Sanchez-Yamagishi, T. Taychatanapat, K. Watanabe, T. Taniguchi, A. Yacoby, and P. Jarillo-Herrero, Quantum Hall effect, screening, and layer-polarized insulating states in twisted bilayer graphene, *Phys. Rev. Lett.* **108**, 076601 (2012).
- [263] B. Fallahazad, Y. Hao, K. Lee, S. Kim, R. S. Ruoff, and E. Tutuc, Quantum Hall effect in Bernal stacked and twisted bilayer graphene grown on Cu by chemical vapor deposition, *Phys. Rev. B* **85**, 201408 (2012).
- [264] R. W. Havener, H. Zhuang, L. Brown, R. G. Hennig, and J. Park, Angle-resolved Raman imaging of interlayer rotations and interactions in twisted bilayer graphene, *Nano Lett.* **12**, 3162–3167 (2012).
- [265] R. He, T.-F. Chung, C. Delaney, C. Keiser, L. A. Jauregui, P. M. Shand, C. C. Chancey, Y. Wang, J. Bao, and Y. P. Chen, Observation of low energy raman modes in twisted bilayer graphene, *Nano Lett.* **13**, 35943601 (2013).

- [266] Z. Liu, L. Ma, G. Shi, W. Zhou, Y. Gong, S. Lei, X. Yang, J. Zhang, J. Yu, K. P. Hackenberg, A. Babakhani, J.-C. Idrobo, R. Vajtai, J. Lou, and P. M. Ajayan, In-plane heterostructures of graphene and hexagonal boron nitride with controlled domain sizes, *Nat. Nanotechnol.* **8**, 119–124 (2013).

---

# Summary

Graphene is a one-atomic thin sheet of carbon. It exists in nature, as a part of graphite. With sticky tape one can exfoliate a single graphene layer from a graphite chunk and transfer it onto a silicon substrate. Graphene's properties are remarkable and very diverse. To name a few: It is a semiconductor with a zero-band gap. Its energy dispersion is conical, which results in massless electrons described by the relativistic Dirac equation. The carbon atoms are arranged in a hexagonal lattice, which gives electrons an extra degree of freedom: the pseudo-spin. The pseudo-spin is connected to the momentum of the electrons, and therefore electrons are chiral in graphene. Furthermore graphene is transparent, very flexible and ten times stronger than steel. It can conduct heat better than diamond and is impermeable even to helium gas. All these properties together make graphene a very attractive platform for research in numerous directions.

We employ graphene's unique properties to explore fundamental physics or create novel applications. This is done by fabricating and measuring graphene nanodevices. The graphene for our devices has been produced with different methods. Next, nanostructures are made by e-beam lithography. Most measurements are done by DC electronic transport at room temperature or at low temperatures as low as 4 K or 50 mK. This thesis describes a diverse set of experiments.

**Transfer Method** We have developed a method to transfer nanostructures and in particular graphene from its substrate onto other substrates with micrometer alignment precision. The transfer occurs by immersing a polymer-coated substrate in water, that separates the polymer from the substrate. Since graphene sticks to the polymer, this method has allowed us to transfer graphene on other substrates than SiO<sub>2</sub>. We have shown that the electronic properties are not significantly affected by the transfer, despite the formation of wrinkles after transfer. We have some control over these wrinkles in size and orientation by engineering the substrate morphology and modifying the surface hydrophobicity.

**Graphene nanopores** We have realised a graphene nanopore, using the transfer method described above. Electronically detecting individual base pairs is a promising method for DNA sequencing. The distance between two DNA base pairs is about  $\sim 0.3$  nm. This distance is about the same as the thickness of graphene. Graphene is at the same time the thinnest material that exists in nature. Thus to achieve single base pair resolution graphene appears to be a logical choice. Single DNA molecules

---

are dragged through a nanopore in graphene by applying an ionic current in a salt solution. During these events the ionic current decreases and hence single molecule translocation events can be detected and further analysed. With this device we have set the first step in the direction of a proto-type DNA sequencing device based on graphene.

**Graphene superconductor interfaces** The interplay between graphene and superconductors at high magnetic fields is not well understood. In that context we have fabricated graphene/NbTiN junctions. NbTiN is a type II superconductor, with a typical critical field of above  $> 11$  T. Transport through a graphene superconductor junction is carried by Andreev reflection, notable by the doubling of the differential conductance. We have observed more than a doubling of the differential conductance in strongly disordered graphene/NbTiN junctions, that may be explained by an enhancement of Andreev reflection caused by disorder near the junction.

**Surface cleaning of graphene** Using the tip of an atomic force microscope, we have mechanically cleaned graphene flakes. This can literally be seen as cleaning graphene with a nanometer sized broom. We have shown an improvement of the electronic mobility and a decrease of external doping. In dual gated bilayer graphene on hexagonal boron nitride (hBN) we have found mobilities up to  $\sim 36,000 \text{ cm}^2 \text{ V}^{-1} \text{ s}^{-1}$ . This new method is particularly relevant when other cleaning methods are not effective or desirable.

**Ballistic transport in CVD graphene** For the first time we have observed ballistic transport in chemical vapour deposited (CVD) graphene on micron length scales. This has so far only been seen in exfoliated graphene. To realise this we have adapted a dry and clean transfer method to transfer CVD graphene onto hBN flakes. CVD graphene has the advantage over exfoliated graphene that it can be produced on a large scale and is thus suitable for industrial purposes. Another attractive aspect is that CVD graphene can become an interesting alternative to exfoliated graphene as a platform for fundamental research.

---

# Samenvatting

Grafeen is een enkel-atoom laag van koolstof. Het komt in de natuur voor als onderdeel van grafiet. Met plakband kan men een enkele laag grafeen los trekken van een brokje grafiet en overdragen op een silicium chip. De eigenschappen van grafeen zijn buitengewoon bijzonder en zeer divers. Hier noemen we enkele: Het is een halfgeleider zonder een energiekloof. De energiespreiding verloopt linear, waardoor elektronen massalooos worden en hun gedrag beschreven wordt met de relativistische Dirac vergelijking. De koolstofatomen zijn gerangschikt in een hexagonaal rooster. Deze ordening biedt elektronen een extra vrijheidsgraad: de pseudo-spin. De pseudo-spin blijkt verbonden met de bewegingsrichting van de elektronen, waardoor elektronen chiraal zijn in grafeen. Verder is grafeen transparant, zeer flexibel en tien keer zo sterk als staal. Het kan warmte beter geleiden dan diamant en is ondoordringbaar zelfs voor helium gas. Al deze eigenschappen samen maken grafeen een zeer aantrekkelijk platform voor onderzoek in tal van richtingen.

We maken gebruik van unieke eigenschappen van grafeen om de fundamentele natuurkunde verkennen of om nieuwe toepassingen maken. Dit wordt gedaan door het vervaardigen en het meten van grafeen nanodevices. Het grafeen voor onze nanodevices is geproduceerd met verschillende methoden. Vervolgens worden nanostructuren geschreven met electronstraallithografie. De meeste metingen zijn uitgevoerd door DC elektronentransport te meten bij kamertemperatuur of bij lage temperaturen tot 4 K of 50 mK. Dit proefschrift beschrijft een gevarieerde set van experimenten.

**Grafeen overdrachtmethode** We hebben een methode om nanostructuren en in het bijzonder grafeen over te brengen van zijn oorspronkelijk substraat op andere substraten ontwikkeld. De overdracht vindt plaats door het onderdompelen van een polymeer gecoat substraat in water. Het water scheidt het polymeer van het substraat. Omdat grafeen aan het polymeer plakt, staat deze methode ons toe om grafeen over te dragen op andere substraten dan  $\text{SiO}_2$ . We hebben aangetoond dat de elektronische eigenschappen niet significant beïnvloed worden door deze overdracht, ondanks de vorming van rimpels in grafeen na overdracht. We hebben enige controle over deze rimpels in grootte en oriëntatie door de morfologie van substraat en het beïnvloeden van de oppervlaktehydrofobiciteit.

**Grafeen nanogaatjes** We hebben een grafeen nanogaatje gerealiseerd, met behulp van de overdracht methode zoals hierboven beschreven. Elektronisch detecteren van afzonderlijke basenparen is een veelbelovende methode voor DNA sequentiebepa-

---

ling. De afstand tussen twee DNA-basenparen is ongeveer  $\sim 0.3$  nm. Deze afstand is ongeveer gelijk aan de dikte van grafeen. Grafeen is tevens het dunste materiaal dat in de natuur bestaat. Dus om een resolutie te halen van een enkel basenpaar lijkt grafeen een logische keuze. Afzonderlijke DNA moleculen worden door het nanogaatje getrokken als gevolg van ionische stroom in een zoutoplossing. Wanneer het DNA molecuul zich in het gaatje bevindt neemt de ionische stroom af. Dit kunnen we zodoende detecteren en verder analyseren. Met dit apparaat hebben we de eerste stap in de richting van een prototype grafeen DNA sequentie apparaat gezet.

**Graphene superconductor interfaces** Van de wisselwerking tussen grafeen en supergeleiders bij hoge magnetische velden is weinig bekend. In dat kader hebben we grafeen met NbTiN verbonden. NbTiN is een type II supergeleider met een typisch kritische veld van meer dan  $> 11$  T. Transport van grafeen naar een supergeleider gaat gepaard met Andreev reflectie, wat waargenomen door een verdubbeling van de differentiele geleiding. In sterk wanordelijk grafeen/NbTiN raakvlakken hebben we meer dan een verdubbeling van de differentiele geleiding waargenomen, die verklaard kan worden door een versterking van Andreev reflectie als gevolg van de wanorde in grafeen.

**Oppervlakte reiniging van grafeen** Gebruikmakend van de punt van een atomaire kracht microscoop, hebben we mechanisch grafeen schoongemaakt. Dit kan letterlijk worden gezien als het schoonvegen van grafeen met een nano-bezempje. Met deze methode hebben wij een verbetering van de elektronische beweeglijkheid en een afname van de externe dotering gerealiseerd. In een bilaag grafeen transistor op hexagonaal boornitride (hBN) hebben we beweeglijkheden tot  $\sim 36,000 \text{ cm}^2 \text{ V}^{-1} \text{ s}^{-1}$  waargenomen. Deze nieuwe methode is met name relevant wanneer andere reinigingsmethoden niet effectief of wenselijk worden geacht.

**Ballistisch transport in CVD grafeen** Voor het eerst hebben we ballistisch transport waargenomen in chemische opgedampt (CVD) grafeen op micron lengteschalen. Dit is tot nu toe alleen waargenomen in geëxfolieerd grafeen (vervaardigd uit de plakband methode). Om dit te realiseren hebben we een droge en schone overdrachtsmethode gebruikt om CVD grafeen overbrengen naar hBN vlokken aangepast. CVD grafeen heeft het voordeel ten opzichte van geëxfolieerd grafeen dat het op grote schaal geproduceerd kan worden en dus geschikt is voor industriële doeleinden. Een ander aantrekkelijk aspect is dat CVD grafeen een interessant alternatief kan worden voor geëxfolieerd grafeen als een platform voor fundamenteel onderzoek.

---

# Curriculum Vitae

Victor Emanuel Calado

- Feb. 10, 1981 Born in Rotterdam, The Netherlands.
- 1994 - 2001 Erasmiaans Gymnasium, Rotterdam
- 2001 - 2009 B.Sc. & M.Sc. Applied Physics, Delft University of Technology
- 2009 - 2013 Ph.D. research at Delft University of Technology, in the Quantum Transport group under supervision of prof. dr. ir. L.M.K. Vandersypen





---

## List of publications

- 10 *Ballistic Transport in CVD graphene*  
V. E. Calado, S. E. Zhu, S. Goswami, Q. Xu, K. Watanabe, T. Taniguchi, G. C. A. M. Janssen and L. M. K. Vandersypen  
Submitted.
- 9 *Formation and control of wrinkles in graphene by the wedging transfer method*  
V. E. Calado, G. F. Schneider, A. M. M. G. Teulings, C. Dekker and L. M. K. Vandersypen  
Applied Physics Letters **101**, 103116 (2012).
- 8 *Laser-thinning of MoS(2): On demand generation of a single-layer semiconductor*  
A. Castellanos-Gomez, M. Barkelid, A. M. Goossens, V. E. Calado, H. S. J. van der Zant and G. A. Steele  
Nano Letters **12**, 3187-3192 (2012).
- 7 *Mechanical cleaning of graphene*  
A. M. Goossens, V. E. Calado, A. Barreiro, K. Watanabe, T. Taniguchi and L. M. K. Vandersypen  
Applied Physics Letters **100**, 073110 (2012).
- 6 *Zero-bias conductance peak and Josephson effect in graphene-NbTiN junctions*  
M. Popinciuc, V. E. Calado, X. L. Liu, A. R. Akhmerov, T. M. Klapwijk and L. M. K. Vandersypen  
Physical Review B **85**, 205404 (2012).
- 5 *Coupling artificial molecular spin states by photon-assisted tunnelling*  
L. R. Schreiber, F. R. Braakman, T. Meunier, V. E. Calado, J. Danon, J. M. Taylor, W. Wegscheider and L. M. K. Vandersypen  
Nature Communications **2**, 556 (2011).
- 4 *Efficient controlled-phase gate for single-spin qubits in quantum dots*  
T. Meunier, V. E. Calado and L. M. K. Vandersypen  
Physical Review B **83**, 121403 (2011).
- 3 *DNA translocation through graphene nanopores*  
G. F. Schneider, S. W. Kowalczyk, V. E. Calado, G. Pandraud, H. Zandbergen, L. M. K. Vandersypen and C. Dekker  
Nano Letters **10**, 3163-3167 (2010).
- 2 *Wedging transfer of nanostructures*  
G. F. Schneider, V. E. Calado, H. Zandbergen, L. M. K. Vandersypen and C. Dekker  
Nano Letters **10**, 1912-1916 (2010).
- 1 *Optical constants of graphene measured by spectroscopic ellipsometry*  
J. W. Weber, V. E. Calado and M. C. M. van de Sanden  
Applied Physics Letters **97**, 091904 (2010).



---

# Acknowledgements

I am indebted to acknowledge anyone who helped me with all the work described in this thesis. First, I want to thank my advisor Lieven Vandersypen for giving me the great opportunity to do my PhD with him. Lieven, your guidance and support have been immensely important to me. You have given me the room for doing exploratory research, precisely as I wished, while being there at the right moments. I have learned really a lot from you.

The work in this thesis could not be done without useful discussions with others in particular the graphene team members: Stijn Goossens, Amelia Barreiro-Megino, Xin Lan Liu and Srijit Goswami. Sharing new ideas (and critically asses) among each other is in my opinion essential for excellent and joyful research. Stijn, apart from being a college we have become friends and have had a lot of fun at conferences and at work!

I like to thank my students, Annemarie Teulings and Thijs Cui, for their valuable efforts they put in the projects. After all, I can conclude that working with students is very stimulating.

There is no science without collaboration. I like to thank all the collaborators that essentially contributed at least half the work of this thesis. Grégory Schneider, your enthusiasm and motivation gave me a boost in the very early stage of my PhD, in retrospect this was invaluable. Mihai Popincuic, it was very enjoyable to work with you and keeping it going with a good mood, despite the quality of the data and samples. Shou-En Zhu, I admire your commitment to science, it was and still is a pleasure to work with you. I am happy to continue this way, I am sure we are going to make new breakthroughs. I like to thank Anton Akhmerov, Cees Dekker, Guido Janssen and Teun Klapwijk for all the useful discussions we have had.


Experimental research cannot be without technical support. I thank Raymond Schouten, for all the help with electronics. Bram van der Enden, Remco Roeleveld, Jelle Haanstra and Aad Poot for the help on cryogenics and lab equipment. I have spend significant time in the cleanroom during my PhD, where assistance from Marc Zuiddam, Marco van der Krogt, Rael Mattern, Charles de Boer, Ewan Hendriks, Anja van Langen-Suurling, Arnold van Run and Hozan Miro was valuable if not more than that.

I want to thank Yuki Nakagawa, Marja Plas, Dominique Meijer and Angèle Fontijn for the administrative support and paperwork.

And after all, since I joined QT in February 2007 I have met a way too many people to mention here. With those I had a great time doing research in combination with all the social aspects in- and outside office hours, on trips, conferences and QT-weekends. Thanks to everyone for this great time!

Victor Calado  
Rotterdam, August 15, 2013





This thesis describes a diverse set of experiments on graphene, a one-atom thin sheet of carbon. We employ graphene's unique properties to explore fundamental physics and novel applications. To do so, we use nano fabrication techniques to create graphene nanodevices.

Here we first developed a water-based transfer method. This transfer method allowed us to realise the first graphene nanopore device. With that device we were able to detect single DNA molecules passing the nanopore. This is the first step towards a prototype DNA sequencing device. Furthermore, we found that the electronic quality of graphene on SiO<sub>2</sub> does not significantly degrade due to the wet transfer, despite the formation of wrinkles in graphene.

Electronic transport from graphene into a superconductor is carried by Andreev reflection, notable by a doubling of the differential conductance. In disordered graphene/NbTiN junctions we have observed more than a doubling of the differential conductance, which can be understood by an enhancement of Andreev reflection mediated by disorder.

We have used the tip of an atomic force microscope to mechanically clean a graphene surface. The electronic quality improved after this cleaning treatment. This new method is particularly relevant when other methods are not effective or desirable.

For the first time we have observed ballistic transport in chemical vapour deposited (CVD) graphene on micron length scales. To realise this we have adapted a dry and clean transfer method to transfer CVD graphene onto hBN flakes. CVD graphene has the advantage that it is scalable and controllable, hence suitable for industrial purposes. While exfoliated graphene is widely used as a platform for fundamental research, CVD graphene may soon become an attractive alternative.